12-2017

From Pyrochlore to the Tripod Kagome Lattice: Magnetism of New Compound Family A2RE3Sb3O14 (A = Mg, Zn; RE = Pr, Nd, Gd, Tb, Dy, Ho, Er, Yb)

Zhiling Dun
University of Tennessee, Knoxville, zdun1@vols.utk.edu

To the Graduate Council:

I am submitting herewith a dissertation written by Zhiling Dun entitled "From Pyrochlore to the Tripod Kagome Lattice: Magnetism of New Compound Family A2RE3Sb3O14 (A = Mg, Zn; RE = Pr, Nd, Gd, Tb, Dy, Ho, Er, Yb)." I have examined the final electronic copy of this dissertation for form and content and recommend that it be accepted in partial fulfillment of the requirements for the degree of Doctor of Philosophy, with a major in Physics.

Haidong Zhou, Major Professor

We have read this dissertation and recommend its acceptance:

Hanno Weitering, David Mandrus, Takeshi Egami

Accepted for the Council:

Dixie L. Thompson

Vice Provost and Dean of the Graduate School

(Original signatures are on file with official student records.)

From Pyrochlore to the Tripod Kagome Lattice: Magnetism of New Compound Family A2RE3Sb3O14 (A = Mg, Zn; RE = Pr, Nd, Gd, Tb, Dy, Ho, Er, Yb)

A Dissertation Presented for the

Doctor of Philosophy

Degree

The University of Tennessee, Knoxville

Zhiling Dun

December 2017

This dissertation is dedicated to my wife, Chunli.

Acknowledgments

Firstly, I would like to thank my advisor, Prof. Haidong Zhou, for being an excellent advisor. His outstanding guidance and insightful advice have made me from a layman who knows little about research to a junior physicist who has published a number of papers and is able to undertake a scientific task alone.

The work described in this dissertation involves lots of collaborations. I would like to express my hearted gratitude to Xiaojian Bai, Dr. Joseph Paddinson, Prof. Martin Mourigal, Prof. Sriram Shastry and all the other collaborators for their contributions to the project. I would especially thank Prof. Arthur Ramirez from University of California, Santa Cruz, who performed all the specific heat measurements and brought a lot of insights into the system.

During these years, I have been traveling around to National Laboratories to learn and perform different experiments. I would like to thank the help from local staff/scientists. They are Minseong Lee and Eun San Choi from National High Magnetic Field Laboratory; Huibo Cao, Clarina dela Cruz, Tao Hong, Masaaki Matsuda, Georg Ehlers, Matthew Stone and Feng Ye from Oak Ridge National Laboratory; Yiming Qiu and Nicolas Butch from National Instituste of Standards and Technology; Yang Ren from Argonne National Laboratory. Without their help, these experiments would never be successful.

I would like to thank Prof. Cristian Batista, Prof. Steve Johnston, Prof. Stephen Nagler and Prof. Takeshi Egami from the University of Tennessee. Even though I am not their student, they offered me a lot of instructions and useful discussions.

I would like to thank Ryan Sinclair for careful reading of my dissertation and correcting grammars. I would also thank my other colleagues, Jie Ma, Ryan Rawl, Qiang Chen and Qing Huang for being helpful in the lab during these years.

I would like to thank the National Science Foundation for funding support of my research.

I would like to thank Prof. Hanno Weitering, Prof. David Mandrus, and Prof. Takeshi Egami for serving on my doctoral committee.

Finally, I would like to thank my families. I want to thank my parents for their unconditional love and support since I was born. I am also very grateful to my wife, Chunli Zhang. Thank you for the company and encouragement during these years even though we are hundreds of miles apart. Thank you for sacrificing your own scientific career to support mine.

Abstract

Geometrical frustration refers to the inability of a complex system to satisfy all its competing interactions within an underlying topological constrained lattice. The two-dimensional kagome lattice is one of the most frustrated lattices and has been a favorite in the theoretical condensed matter community. However, the large variety of exotic states predicted in kagome lattices lies in contrast to a paucity of experimental systems, making new kagome lattice compounds highly desired.

In this dissertation, I shall provide a systematic study of the structural and magnetic properties of a new compounds family, $A_2RE_3Sb_3O_{14}$ (A = Mg, Zn; RE = Pr, Nd, Gd, Tb, Dy, Ho, Er, Yb). These compounds feature a hitherto unstudied "tripod kagome lattice (TKL)" that was realized by partial ion substitution in the pyrochlore structure. In this dissertation, I shall first briefly introduce the frustrated magnetism and experimental methods in the first two chapters. The third part will cover some general aspects of the TKL, including its structural relation to the pyrochlore lattice, the unique tripod-like spin anisotropies, and spin Hamiltonian. In the fourth chapter, I shall present susceptibility (dc, ac) and specific heat measurements and do a case by case investigation of their magnetic ground states. These include non-collinear spin orders, dipolar spin orders, spin glasses, magnetic charge orders, and several quantum spin liquids. These ground states are compared with the parent pyrochlore lattice and are understood from the standpoint of a balance among spin-spin interactions, anisotropies and Kramers/non-Kramers nature of single ion state. In the fifth chapter, an in-depth neutron scattering study of $Mg_2Ho_3Sb_3O_{14}$ is provided, demonstrating the system to be a kagome spin ice from a transverse Ising model. The last section contains the conclusions of this dissertation and offers perspectives for future work.

Table of Contents

List of Tables

List of Figures

List of Abbreviations

2D ..... Two-Dimensional

A-RE ..... $A_2RE_3Sb_3O_{14}$ (e.g. MgHo for $Mg_2Ho_3Sb_3O_{14}$)

CEF ..... Crystal Electric Field

CW ..... Curie-Weiss

DCS ..... Disk Chopper Spectrometer

ECO ..... Emergent Charge Order

gMFT ..... Gauge Mean-Field Theory

HTSE ..... High Temperature Series Expansion

KSI ..... Kagome Spin Ice

LRO ..... Long-Range Order

mmECO ..... moment-modulated Emergent Charge Order

NHMFL ..... National High Magnetic Field Laboratory

NMR ..... Nuclear Magnetic Resonance

NIST ..... National Institute of Standards and Technology

PPMS ..... Magnetic Properties Measurement System

QSL ..... Quantum Spin Liquid

QSI ..... Quantum Spin Ice

RCO ..... Relaxation-Coupled Oscillator

RPA ..... Random Phase Approximation

RVB ..... Resonating Valence Bond

SEQUOIA ... Fine-Resolution Fermi Chopper Spectrometer

SG ..... Spin Glass

SRO ..... Short-Ranged Order

SNS ..... Spallation Neutron Source

TIM ..... Transverse Ising Model

TKL ..... Tripod Kagome Lattice

VSM ..... Vibrating Sample Magnetometer

μ**SR** ..... Muon Spin Resonance

Chapter 1

Introduction

This chapter is intended to give a brief introduction to geometrical frustration as well as some frustrated systems. I shall begin with some basic concepts in frustrated magnetism. After that, a brief review of pyrochlore oxides will be provided as the system that we studied is a kagome variant from the pyrochlore lattice. The third section contains important information related to the kagome antiferromagnet which is highly related to the physics discussed in the following chapters. Lastly, I will show how the TKL is realized from a pyrochlore lattice and why this will be a considerable improvement for experimental studies on kagome physics.

1.1 Basic Concepts of Frustrated Magnetism

In physics, frustration refers to the presence of competing forces that cannot be simultaneously satisfied. Frustrated magnetism arises from the systems in which localized magnetic moments, or spins, interact through competing exchange interactions that cannot be simultaneously satisfied, giving rise to a large degeneracy of the system's ground state [13]. Usually, antiferromagnetic interactions on lattices that involve triangular motifs are responsible for this behavior. It is clear from from Fig. 1.1(a) that a triangle of antiferromagnetically interacting Ising spins, which must point upward or downward, is the simplest example of frustration. When a pair of spins are aligned with anti-parallel moments, the third spin is frustrated, resulting in the same total energy with either the up or down spin configuration. On the other hand, the same model on a square lattice (1.1(c)) or Ising

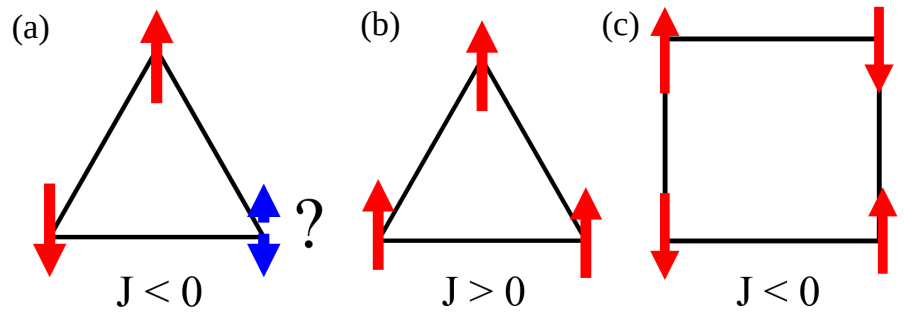

Figure 1.1: Ising models for (a) a triangle with antiferromagnetic spins, (b) a triangle with ferromagnetic spins, and (c) a square with nearest-neighbor antiferromagnetic spins.

spins with ferromagnetic interactions (1.1(b)) are not frustrated because there is a unique state which has the lowest energy for these systems. This example already demonstrates two important aspects of frustrated magnetism which are equally important: many-body interactions and the geometry of the underlying lattice.

The study of geometrical frustration begins with the idea of classical ground state degeneracy which is now considered to be a key, or even a defining, characteristic of frustration. Wannier showed in 1950 that an antiferromagnet consisting of a two-dimensional (2D) triangular lattice has a very large number of degenerate ground states [14]. The ground-state entropy is extensive and is equal to 0.323 k_BN, where k_B is the Boltzmann constant and N is the number of spins. When the temperature is lowered, the spins fluctuate thermally in a correlated manner. The same idea could also be applied to a pyrochlore lattice or a kagome lattice antiferromagnet where the degenerated ground states are known to be a spin ice [15] and a kagome spin ice (KSI) [16], respectively. In these states, classical fluctuations (thermal activation) dominate. Given the Ising nature, excitations of any form will require a minimum energy to flip one spin. The system will eventually fall out of equilibrium and freeze into one of the microstates when the temperature is sufficiently low. Therefore, these systems can be viewed as classical spin liquids, or cooperative paramagnets, which are analogous to an ordinary liquid composed of molecules that form a dense, highly correlated state that has no static order [13].

When quantum spin fluctuations are introduced into a frustrated magnet with small spin numbers, the quantum mechanical uncertainty principle produces zero-point motions comparable to the size of the spin itself which persists down to $T = 0$ K. Although they are

similar to thermal fluctuations in some ways, quantum fluctuations can be phase coherent. If they are strong enough, the result is a quantum spin liquid (QSL), a superposition state in which the spins simultaneously point in many different directions [13]. The study of QSLs begins with P. W. Andersen's proposal of the resonating valence bond (RVB) in 1987 [17]. In his original proposal, nearby spins form pairs of rotationally invariant singlets, or valence bonds, which do not develop long-range order (LRO) in any local order parameter at any temperature. For the ground state to be a RVB, it is necessary that large-scale resonances between different singlet configurations lead through interference effects to a noticeable energy gain. In other words, the ground state is a superposition of different partitionings of spins into valence bonds. Later, it was realized that valence bonds need not be formed only from nearby spins [18]. If a valence bond is formed from spins that are far apart, the spins are less tightly bound, consequently more easily excited into a state with non-zero spin, giving rise to a possibility of large numbers of different QSL states. In an attempt to classify these states, X. G. Wen has used the concept of the projective symmetry group and has classified hundreds of QSLs on $S = 1/2$ antiferromagnets on the square lattice [19]. It is noteworthy that QSLs are not "disordered systems", and most of them are expected to possess a definite topological order for both their ground states and their collective excitations. In this sense, they are much more akin to superconductors or quantum spin Hall liquids than to spin glasses (SG) [20]. In terms of excitations, a QSL is a state with fractional quasi-particle excitations. In ordinary phases of matter, all of the excitations are constructed from elementary excitations that are either electron-like (spin $S = 1/2$ and charge $\pm e$) or magnon-like (spin $S = 1$ and charge-neutral). In QSLs, the excitations are usually "spinons", an exotic quasi-particle carrying a half-integer spin (normally 1/2) and are charge-neutral. The property that the excitation is fractional means that spinons can be placed far away from each other with a finite energy cost; in other words, they can be deconfined [21]. In this sense, a spinon is a "fraction" of an electron. Spinons are well established in one-dimensional (1D) systems in which they occur as domain walls [22]. In 2D and 3D systems, a spinon is created simply as an unpaired spin which can then move by locally adjusting the nearby valence bond configurations.

On the experimental side, the frustration index, $f \equiv \theta_W/T_c$, provides a quantitative measure of the level of frustration [23]. Here, θ_W is the Weiss temperature that characterizes the sign and strength of interaction, and T_c is the ordering or spin freezing temperature. In frustrated magnets, the paramagnetic region usually extends to temperatures well below θ_W, giving rise to a large value of f. The T_c or the absence of static moments can be probed by susceptibility and specific heat measurements or by nuclear magnetic resonance (NMR) and muon spin resonance (μSR) experiments. More detailed information on the correlation and excitations is provided by magnetic neutron scattering, which probes the dynamical structure factor $S(\mathbf{Q}, \omega)$ of the system. A more detailed introduction of this experimental technique can be found in Chapter 2.

1.2 Pyrochlore Oxides

The 3D pyrochlore lattice is one of the most important frustrated systems. Over the past several decades, interest in the magnetic behavior of pyrochlore oxides of type $RE_2^{3+}X_2^{4+}O_7$, where RE is a rare earth ion and X is usually a transition metal, has exploded. Both the RE and X sites form a network of corner-sharing tetrahedron (Fig. 1.2 (a)). Due to various RE elements in the periodic table and a large number of transition metals, the pyrochlore oxides form a large family of compounds that could stabilize as a cubic structure at room temperature (Fig. 1.2 (b)). Moreover, because of the various spin numbers and spin anisotropies of different RE^{3+} ions, the complex interplay among the spin-orbital coupling, dipolar, and exchange interactions leads to many novel ordered/disordered states. For example, this interplay leads to multi-k ordering [24] with multiple field induced transitions [25] for Heisenberg spins in $Gd_2Ti_2O_7$, the spin ice state in $Ho_2Ti_2O_7$ [26] and $Dy_2Ti_2O_7$ [27] for classical Ising spins, possible quantum spin ice (QSI) phases in $Pr_2X_2O_7$ (X = Sn, Zr) [28, 29], $Tb_2Ti_2O_7$ [30] and $Yb_2Ti_2O_7$ [31] for quantum Ising models, as well as the order by disorder physics in the XY spin system $Er_2Ti_2O_7$ [32]. This section will mainly focus on the physics of spin ice and QSI since they are strongly related to the observations in the TKLs discussed in the following chapters.

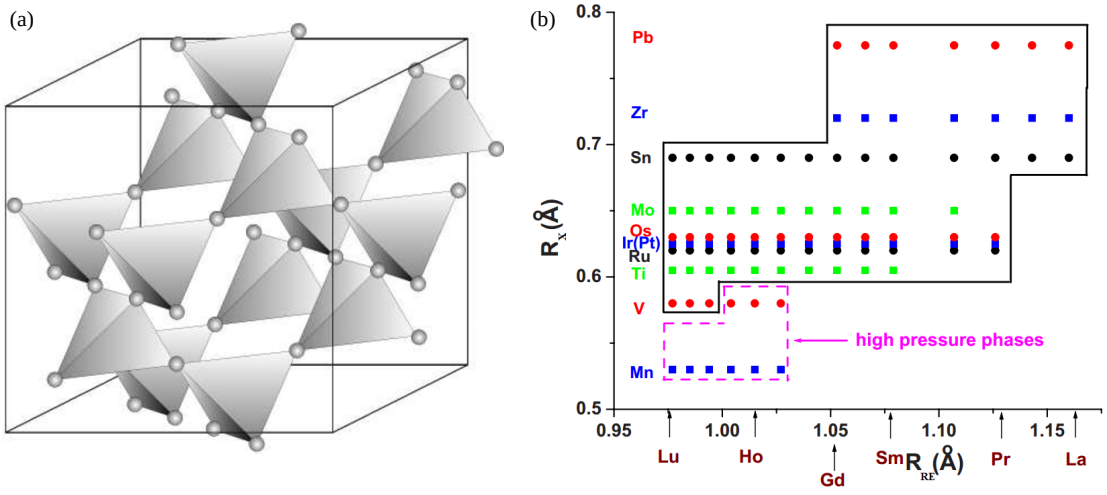

Figure 1.2: (a) A pyrochlore lattice composed of corner-shared tetrahedrons. (b) A structure-field or stability-field map for $RE_2X_2O_7$ materials. Adapted from Ref. [1].

1.2.1 Spin Ice

The spin-ice phenomenology in the pyrochlore oxides was discovered in 1997 in $Ho_2Ti_2O_7$ [26]. In $Ho_2Ti_2O_7$, the strong axial crystal electric field (CEF) acting on the Ho^{3+} ion gives rise to an almost ideal classical Ising spin. The local Ising axis is along the four local cubic [111] directions such that a spin can only point either "in" or "out" of a tetrahedron. Within a tetrahedron, there are six degenerate two-in-two-out spin configurations that minimize the effective ferromagnetic exchange energy. Given a large number of spins, there is a large number of ground state degeneracies and a zero point entropy, similar to the statistic problem of triangular Ising antiferromagnets mentioned above. This degeneracy can be described by borrowing Pauling's argument of the residual proton configuration disorder in hexagonal water ice [33]. Because of this analogy, these systems have been given the name spin ice. Soon after the proposal of spin ice in $Ho_2Ti_2O_7$, Ramirez et al. [27] measured precisely the zero-point entropy in $Dy_2Ti_2O_7$, establishing $Dy_2Ti_2O_7$ as another spin ice material. For both Dy and Ho pyrochlores, the large 10 μ_B moments lead to a critical role for magnetic dipole-dipole interactions. It is the large dipolar interaction ($\sim$ 2.35 K) that overcomes the antiferromagnetic exchange interaction ($\sim$ 1.2 K) and results in a spin ice state. The dipole-dipole correlation is faithfully reflected by an elastic neutron scattering experiment.

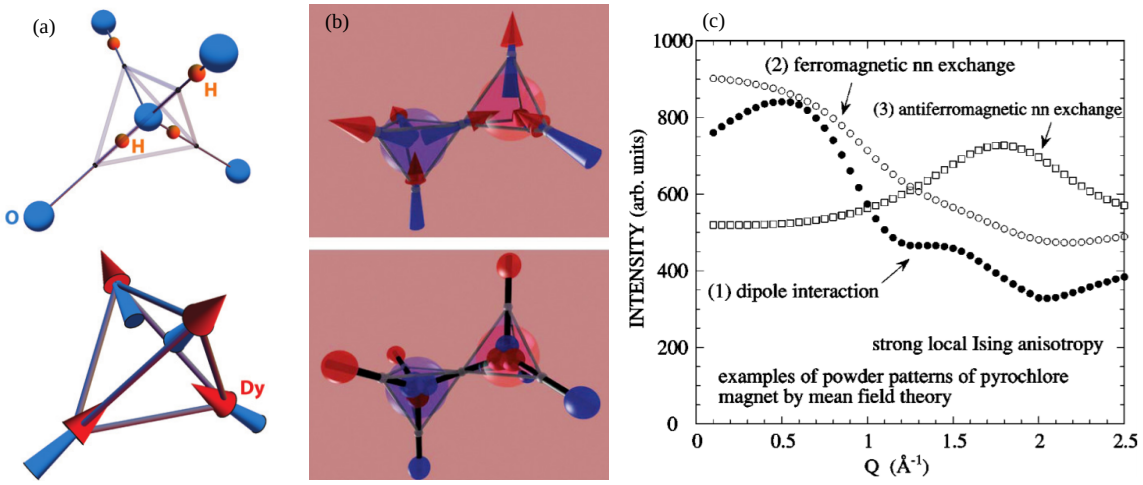

Figure 1.3: (a) Illustration of the mapping between spin ice and water ice. (b) Illustration of the spin to dumbbell mapping for tetrahedron hosting positive and negative monopoles. This figure is taken from Ref. [2]. (c) Examples of magnetic diffuse scattering of different models on a pyrochlore lattice calculated by the mean-field theory. This figure is adapted from Ref. [3].

As shown in Fig. 1.3, the observed diffuse scattering pattern can only be obtained using the dipolar model.

Another important consequence of long-range dipolar interaction relies on the excitations. When going beyond the equilibrium condition, a single spin flip process in the spin ice manifold will break the ice rule for two neighboring tetrahedra. From a magnetic viewpoint, the center of this tetrahedron becomes a source or sink for flux, that is, a magnetic monopole. Therefore, a single spin flipping corresponds to creating two equal and opposite magnetic monopoles on nearest-neighbor diamond sites (Fig. 1.3 (b)). In the dumbbell model description, the energy of two defects located at a distance apart is simply the sum of two defect creation energies and a magnetic Coulombic interaction between the defects [2]. Many experiments in which the monopoles in spin ice are studied and manipulated have already been performed. For example, Jaubert and Holdsworth showed that the energy of a monopole can be extracted from the Arrhenius behavior of the magnetic relaxation rate [34]. Using neutron scattering measurements under magnetic fields, Morris, et al. provided evidence of Dirac strings in the $Dy_2Ti_2O_7$ [35]. By measuring the current using the electromotive force, a group in England is able to derive the microscopic parameters of monopole motion in spin ice states and to identify the distinct roles of free and bound magnetic charges [36]. Overall,

the discovery of monopoles in spin ices has connected this classical spin liquid system to fractionalization and topological order, and it appears not yet to be losing momentum [37]!

1.2.2 Quantum Spin Ice

A QSI is a type of U(1) QSL which might be observed in certain pyrochlore magnets. It is achieved by introducing quantum dynamics into the classical nearest-neighbor spin ice model. The dynamics term could be a perturbative "transverse" nearest-neighbor exchange couplings ($J_\perp$) in addition to the "longitudinal" Ising exchange term (J_{zz}). A minimal model is given by a local XXZ Hamiltonian:

$$H_{\text{QSI}} = J_{zz} \sum_{i,j} S_i^z S_j^z - J_\perp \sum_{i,j} (S_i^+ S_j^- + S_i^- S_j^+), \tag{1.1}$$

where S^+ and S^- are spin ladder operators. Here, the transverse couplings are required to have a characteristic energy scale $J_\perp < J_{zz}$ such that the manifold of a classical spin ice state forms a reference classical spin liquid, the background on which quantum fluctuations can act perturbatively [4, 13]. The lowest order terms derived from a canonical perturbation theory that preserves the ice rule constraint are ring exchange terms that live on the hexagonal loops on the pyrochlore lattice (Fig. 1.4 (a)). The ring exchange model then reduces to a quantum dimer model on a diamond lattice which can be analyzed using the properties of the soluble point [38]. In short, a QSL phase is found in this minimal model by both the U(1) Gauge theory [38] and quantum Monte Carlo simulations [39]. Besides $J_\perp$ and J_{zz}, there are two extra terms ($J_{\perp\perp}$, $J_{z\perp}$) allowed by symmetry on the pyrochlore lattice [40] that originate from linear transformations of a pseudo-dipolar interaction and a Dzyaloshinskii-Moriya interaction. Using gauge mean field theory (gMFT), the zero temperature phase diagram using the coupling parameters $J_{ex} = (J_{zz}, J_\perp, J_{\perp\perp}, J_{z\perp})$ has been studied for systems with Kramers ions [5]. An example phase diagram produced using this method is shown in Fig. 1.4 (b). Besides the conventional ferromagnetic and antiferromagnetic ordered states, a QSI phase appears as expected, in a region where the Ising coupling J_{zz} is sufficiently larger than the other terms.

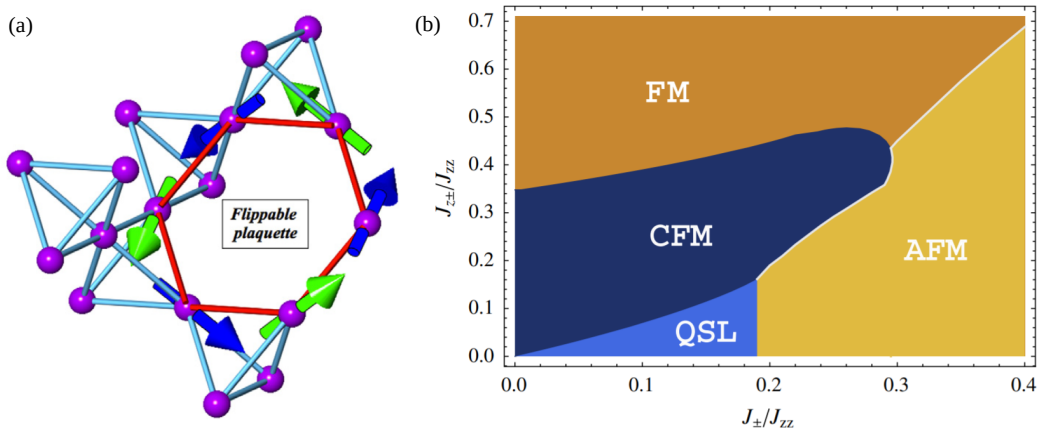

Figure 1.4: (a) A segment of a [111] kagome plane in the pyrochlore lattice showing one closed hexagonal loop (in red) and a flippable spin configuration around that loop. The figure is taken from Ref. [4]. (b) A zero temperature gMFT phase diagram taken through sections in the space of symmetry-allowed nearest-neighbor exchange couplings on the pyrochlore lattice. This figure is adapted from Ref. [5].

Among the pyrochlore family, $Tb_2Ti_2O_7$, $Pr_2X_2O_7$ (X = Sn, Zr) and $Yb_2Ti_2O_7$ are candidates for displaying some of the QSI phenomenologies.

$Tb_2Ti_2O_7$ was the first material which was named a QSI [41]. The Tb^{3+} moments have strong Ising characteristics, and they do not develop LRO down to the lowest measured temperatures. Early neutron studies found a broad region of diffuse scattering around **Q** = (002) [42], suggesting non-Ising fluctuations. It was then realized that the first excited CEF level in this system is only 18 K above the ground state doublet which allows for a significant admixing between the CEF states through exchange and long-range dipolar interaction [43]. Calculations show that $Tb_2Ti_2O_7$ might sit on the boundary between an all-in-all-out LRO phase and a two-in-two-out spin ice state. Recently, it has been argued that a sizable magneto-elastic response in this system will split the ground state doublet, leading to a singlet-singlet gap as large as 2 K and that this is the principal reason why this system does not order [44]. Overall, $Tb_2Ti_2O_7$ behaves like a QSL experimentally, and with spin ice like correlations and transverse fluctuations, a (partial) QSI picture is still possible at this moment [4].

The studies on $Pr_2X_2O_7$ (X = Sn, Zr) have just begun only recently. In these two materials, Pr^{3+} is a non-Kramers ion that possess a magnetic CEF Ising doublet ground state, similar to that in $Ho_2Ti_2O_7$ and $Tb_2Ti_2O_7$. Both compounds display some of the key

characteristics of spin ice states, such as the Pauling zero-point entropy and pinch points [28, 29]. However, inelastic neutron scattering suggests that the low-temperature state of this system remains dynamic down to at least 100 mK, in sharp contrast with classical spin ices where almost no inelastic response is observed [45]. A recent single crystal neutron scattering measurement on $Pr_2Zr_2O_7$ revealed a broad continuum of excitations, the temperature and magnetic field dependence of which indicates a continuous distribution of quenched transverse fields acting on the non-Kramers CEF ground state doublets [46]. It appears that the disorder in $Pr_2Zr_2O_7$, which might come from the high-temperature single crystal synthesis, induces a QSL state. A QSI model associated with this observation is proposed by L. Savary and L. Balents in 2017 that states in non-Kramers spin ices, disorder induces quantum entanglement and engenders an associated emergent gauge structure and set of fractional excitations [47].

The interest in $Yb_2Ti_2O_7$ has continued growing since early 2000. In this system, early specific heat and μSR measurements show a LRO transition at T_c 0.21 K, resulting in a splayed ferromagnetic state. The magnetic moments are found to be predominantly aligned along one of the six [100] cubic directions, but slightly splayed away from complete alignment. Below T_c, a temperature-independent relaxation rate is found by μSR [48] along with rods of diffuse scattering along the [111] directions in the elastic neutron spectrum [49]. In $Yb_2Ti_2O_7$, although the Yb^{3+} ions possess an XY-type anisotropy (meaning that the magnetic moments have their largest magnetic response perpendicular to the local [111] direction), the strongest interaction in the system is believed to be the Ising coupling (J_{zz}), validating a QSI model at the first stage. This was demonstrated by Ross et al. through spin wave measurements of the polarized state under an external magnetic field [31]. However, this picture is somehow challenged by a more recent neutron scattering experiment [50], which finds a much smaller J_{zz} compared to the previous report.

Overall, the three materials discussed above, are all described to some extent by the effective spin-1/2 QSI Hamiltonian Equ. 1.1 from which one can obtain an exotic gapless U(1) QSL state. However, none of them have yet been confirmed to be a clear realization of such a state. More theoretical and experimental work is expected to appear in the coming years.

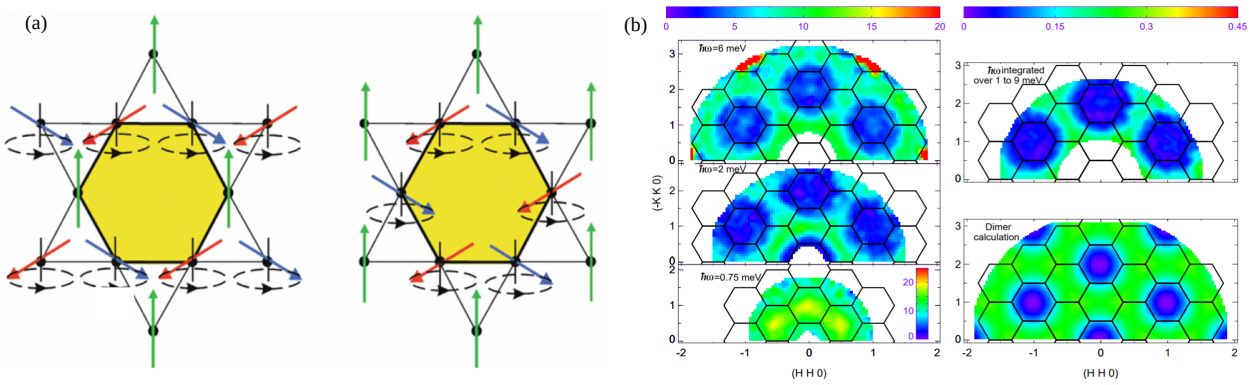

Figure 1.5: (a) A kagome lattice with $\mathbf{q} = 0$ and $\mathbf{q} = \sqrt{3} * \sqrt{3}$ local modes. (b) Momentum structure of the inelastic neutron scattering data for single crystal samples of $ZnCu_3(OH)_6Cl_2$ at 1.6 K for three different energies. Adapted from Ref. [6].

1.3 Kagome Antiferromagnet

The kagome lattice defines a certain type of 2D structure constructed by a network of corner-shared triangles (Fig. 1.5). It has been a favorite in the theoretical condensed matter community since the experimental work on $SrCr_8Ca_4O_{19}$ [51]. This section will begin with the most studied model on the kagome lattice, that is, an ideal Heisenberg antiferromagnet. Its experimental realization in herbertsmithite $ZnCu_3(OH)_6Cl_2$ will also be covered. After that, the physics of kagome spin ice (KSI) and emergent charge order (ECO) will be introduced. These exotic phenomena are theoretically predicted based on Ising spins, but have not been realized yet experimentally.

1.3.1 Nearest-Neighbor Heisenberg Model

Contrary with the initial proposal by Anderson on triangular and square lattices, corner sharing is a key ingredient for stabilizing fluctuating ground states, such as the RVB or QSL states [52]. The nearest-neighbor Heisenberg model on a kagome lattice is one of this kind. Even at a mean field level, the corner-sharing geometry generates a macroscopic ground state degeneracy and branches of zero energy excitations. As shown in Fig. 1.5 (a), given a LRO state in a kagome lattice, simultaneous local rotation of spins belonging to two sublattices has no energy cost. The cooperative motion results in a short correlation length which prevents LRO even at zero temperature. Over the years, there has been tremendous

interests investigating the ground state of this "simple" model. Using different theoretical approaches, various ground states have been found, including RVB, Z2-QSL, U(1)-QSL, chiral spin liquid, etc., with either gapped or gapless excitations. They are reviewed in a paper by M. R. Norman, where one could locate an introduction to the related theories [53].

From the experimental point of view, the ideal kagome antiferromagnet should follow three criteria: (i) decoupled kagome planes with negligible interlayer interactions, (ii) an absence of perturbations such as anisotropies, further neighbor interactions, and dipolar interactions, and (iii) a spin equals to 1/2 to increase quantum fluctuations. Among all of the explorations of the ideal kagome Heisenberg antiferromagnets, Herbertsmithite $ZnCu_3(OH)_6Cl_2$ stands out, fitting all of the criteria. This material features well defined Cu^{2+}-kagome layers that are well separated by diamagnetic Zn^{2+} layers. Furthermore, Cu^{2+} is a spin-1/2 ion with highly isotropic couplings. Various measurements, including specific heat, muon spin rotation (μSR), and neutron scattering fail to observe any sign of spin ordering or freezing down to mK regions [54, 55, 56]. Exploiting the advantages of single crystals for neutron scattering measurements, Han et al. found spectra with a modest dependence on both momentum and energy (Fig. 1.5 (b)), representing a spinon continuum [6]. Above 1 meV, the momentum pattern is what one would expect for near-neighbor antiferromagnetic correlations within the kagome plane. One problem with Herbertsmithite is the structural defeat, i.e. Zn-Cu anti-site disorder. Resonant X-ray measurements revealed that 15% excess copper sits on the zinc sites [57], resulting in strong correlations in the excitation spectrum below 1 meV [58]. Nevertheless, $ZnCu_3(OH)_6Cl_2$ still remains to date the most promising QSL candidate from a nearest-neighbor Heisenberg model.

1.3.2 Kagome Spin Ice and Emergent Charge Order

In terms of anisotropy, the pure Ising kagome case has been treated theoretically [59]. Again, the absence of order is predicted, leading to a classical spin liquid. A mathematically equivalent problem is enforcing in-plane Ising anisotropy (spin points either into or out of the center of each triangle) and ferromagnetic nearest neighbor interaction. This is a spin-ice-like system in a kagome layer – a kagome spin ice (KSI). A preventative spin configuration of the KSI state is shown in Fig. 1.6 (a). The local ice rule will be either one-in-two-out or

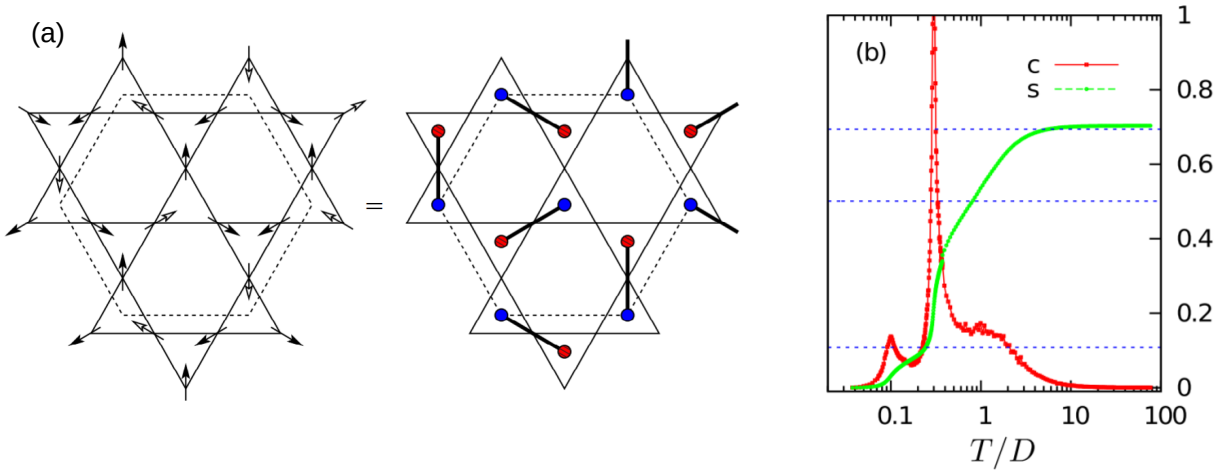

Figure 1.6: (a) Magnetic configurations of the dipolar KSI and their alternative representations, showing one of the ground states exhibiting the $\sqrt{3}*\sqrt{3}$ magnetic order, and its depiction in terms of dimers. Blue/red dots present negative/positive magnetic charges, respectively. (b) Temperature dependence of the specific heat and entropy per spin of the dipolar KSI. The sharp large peak corresponds to the ECO transition, and the small peak at $T \sim 0.1\ D$ corresponds to the LRO transition. Adopted from Ref. [7].

two-in-one-out for a single triangle and there are six degenerate states out of eight possible configurations. The degeneracy and the associated zero-point entropy have been determined by analytic and classical Monte Carlo calculations ($0.50R$ per mole spin here) [16] which greatly exceeds that of the pyrochlore spin ice.

The model discussed above has only considered the nearest neighbor exchange interaction. In the presence of the long dipolar interactions, the magnetic charge emergents. The emergent charge is defined as the algebraic sum over the three charges it contains (Fig. 1.6 (a)), similar to the magnetic monopole in spin ices. Therefore, when the ice rules are unanimously fulfilled at low temperatures, the total magnetic charge at each vertex of the triangle is ± 1. The interaction can be alternatively written as the sum of the nearest-neighbor short-ranged order (SRO) KSI ferromagnet and the magnetic Coulomb interaction between the charges [7]. As demonstrated by Monte Carlo simulations, the Coulomb interaction drives a sharp transition to an emergent charge ordered (ECO) state that is absent for nearest-neighbor interactions alone (Fig. 1.4 (b)). In this state, positive and negative charges alternate, but the remaining threefold degeneracy of the spin states for each charge means

that the spin order is only partial. Being a partially ordered state, the ECO state has non-zero entropy ($\sim 0.11R$ per mole spins). This part of the entropy can only be released given a loop dynamic of spin-flipping, which results in a $\sqrt{3}*\sqrt{3}$ LRO state at a temperature well below the ECO transition (Fig. 1.4 (c)).

Experimentally, there are at present no experimental realizations of kagome Ising magnets. The kagome ECO states have been observed in spin-ice materials under applied magnetic fields [60, 61] and nano-fabricated systems in the 2D limit [62]. However, a crucial experimental observation of KSI or ECO states has remained elusive in a bulk kagome compound.

1.4 Towards new Kagome Magnets

Besides the QSL, KSI and ECO states mentioned above, many other exotic states are predicted in a kagome lattice, such as the spin-orbital liquid state [63], dipolar spin order [8], the Kosterlitz-Thouless transition [64], Quantum Order by Disorder (QObD) [65], nematicity and supernematicity [66]. However, the large variety of exotic states predicted lies in contrast to a paucity of experimental systems. Besides herbertsmithite, recent attention has also been paid to vesignieite $BaCu_3V_2O_8(OH)_2$ [67] and the barlowite $Cu_4(OH)_6BrF$ [68]. From a materials standpoint, however, these systems are limited by (i) known defect-prone structures, and (ii) the inability to substitute facilely on the magnetic site (e.g with non-Heisenberg spins) to realize states other than the QSL. Clearly then, finding new KLM-containing compounds with spin-type variability is a challenge of the highest order.

Intriguingly, a 2D kagome lattice is naturally contained in the frustrated 3D pyrochlore structure. In pyrochlores $RE_2X_2O_7$, both the RE^{3+} and X^{4+} sublattices form alternating kagome and triangular layers along the [111] axis as a result of corner-shared tetrahedrons. However, the strong interlayer interactions enforce three-dimensionality. Obviously, if one can remove the magnetic moment of the triangular layers in the pyrochlore lattice, a RE-kagome-only lattice might be realized, enabling the study of intrinsic kagome physics. Because of various spin and spin anisotropies of different RE^{3+} ions, strong spin-orbital

coupling, and long-ranged dipolar interactions in addition to the exchange couplings, rich physics is immediately available which obviously goes beyond QSL physics.

In this dissertation, I shall introduce a new family of kagome lattice compounds - $A_2RE_3Sb_3O_{14}$ (A = Mg, Zn; RE = Pr, Nd, Gd, Tb, Dy, Ho, Er, Yb), which are realized by partial ion substitution in the pyrochlore lattice. Here, the triangular layers in the pyrochlore structure are occupied by non-magnetic A^{2+} ions, leaving the RE^{3+}-kagome layer well isolated from neighboring layers. We studied their structures as well as their magnetism by dc-, ac-susceptibility, specific heat, and neutron scattering measurements, which reveal various ground states. Some of them have been predicted but have not been realized before experimentally. Some of them even go beyond theoretical considerations. I hope the comprehensive study in this dissertation can provide a guidance for further studies and stimulate more works on these exciting compounds.

Chapter 2

Experimental Methods

This chapter provides details of experimental methods as well as a brief introduction of some of the relevant research techniques. I do not intend to go into the details for x-ray diffraction (XRD), specific heat, magnetic susceptibility, and magnetization measurements as they are basic concepts in the solid state physics. Magnetic ac susceptibility and neutron scattering are two important techniques used in the dissertation; therefore, they are briefly introduced

2.1 Sample Synthesis

All of the $A_2RE_3Sb_3O_{14}$ (A = Mg, Zn; RE = Pr, Nd, Gd, Tb, Dy, Ho, Er, Yb) samples studied in this dissertations are in the polycrystalline form and were synthesized by standard solid state reactions. Starting materials are fine powders ($\sim$ 300 mesh) of RE_2O_3 (RE = Nd, Gd, Dy, Ho, Er, Yb) / Pr_6O_{11} / Tb_4O_7, Sb_2O_3, and MgO/ZnO which were purchased through commercial vendors. For the $Zn_2R_3Sb_3O_{14}$ branch of the family, stoichiometric mixtures were carefully ground, pressed into pellets and reacted at a temperature of 1200 °C in air using a box furnace for three days with several intermediate grindings. For the $Mg_2R_3Sb_3O_{14}$ branch, a higher reaction temperature of 1300 - 1350 °C was required to obtain pure phases.

2.2 X-Ray Diffraction and Structural Refinements

Powder XRD were carried out using a HUBER X-ray powder diffractometer with Cu Kα radiation ($\lambda = 1.5418\mathring{A}$). Measurements were taken at room temperature between $4 \leq 2\theta \leq 100$ ° with $\Delta 2\theta = 0.05$ °.

Rietveld analysis of the XRD data was carried out using the programs of FULLPROF suite [69]. Peak shapes were modeled using a pseudo-Voigt function convoluted with an axial divergence asymmetry function. Backgrounds were obtained through linear interpolation between a set of manually chosen background points with refinable heights.

2.3 Specific Heat

The low temperature (0.076 K $\leq T \leq$ 7 K) specific heat ($C(T)$) measurements were performed in a He3-He4 dilution refrigerator using the semi-adiabatic heat pulse technique. The powder samples were cold-sintered with Ag powder, the contribution of which was measured separately and subtracted from the data. These measurements were performed by Jennifer Trinh and Arthur P. Ramirez in the University of California, Santa Cruz. The high-temperature specific heat ($2 \leq T \leq 300$, K) measurements were carried out on a Quantum Design Physical Properties Measurement System. The lattice contribution to the heat capacity is estimated from the results of a measurement of the non-magnetic isomorph $Zn_2La_3Sb_3O_{14}$.

It is common that the nuclear specific heat is likely to appear at ultra-low temperatures (≤ 0.5 K) in rare-earth compounds. The nuclear specific heat contains two parts, a contact hyperfine coupling that comes from the interaction between electronic spin and nuclear spin, and a quadrupolar contribution that describes the interaction between the nuclear electric quadrupole moment and the electric field gradient at the nucleus [70]. The expression of the nuclear specific heat Hamiltonian is:

$$C_N = \frac{R}{(k_B T)^2} \frac{\sum_{i=-I}^{I} (E_i^2 - E_i E_j) \exp\left(-\frac{E_i + E_j}{k_B T}\right)}{\sum_{i=-I}^{I} \exp\left(-\frac{E_i + E_j}{k_B T}\right)}, \tag{2.1}$$

where E_i (i = -I, ..., I)are the eigenvalues of the nuclear hyperfine coupling Hamiltonian:

$$H_N = Ai\langle J_z\rangle + P\left[i^2 - \frac{1}{3}I(I+1)\right]. \tag{2.2}$$

Here, I is the nuclear spin quantum number and J_z is the electronic spin angular momentum quantum number. A and P are the hyperfine coupling and the quadrupolar coupling constants, respectively.

In Chapter 5, we will focus on the nuclear specific heat analysis of $Mg_2Ho_3Sb_3O_{14}$. The Ho element has only one isotope with nuclear spin $I = 7/2$ and $J = 8$ following Hund's rules. The hyperfine coupling constants have been determined for Ho metals with $A = 0.0399$ K and $P = 0.002$ K [71]. Therefore, given a static moment size ($\mu_{static} = g_J\langle J_z\rangle$) of the Ho^{3+} ions, the nuclear specific heat can be calculated numerically following Equ. 2.1.

2.4 DC Susceptibility and Magnetization

Magnetic dc susceptibility (χ_{dc}) measurements were made using a Magnetic Properties Measurement System (MPMS) with a superconducting interference device (SQUID) magnetometer. Measurements were made after coolinsg in zero field and in a measuring field of μ_0H = 0.1T over the temperature range between 2 K and 300K. The Weiss temperature (θ_W) was obtained by Curie-Weiss (CW) fit of the inverse susceptibility. Isothermal magnetization $M(H)$ measurements were made using a Quantum Design Vibrating Sample Magnetometer (VSM) at 2 K with magnetic fields between -6.5 $\leq \mu_0 H \leq$ 6.5T.

2.5 AC Susceptibility

The ac susceptibility (χ_{ac}) measurement is an important tool for characterizing magnetic materials. In ac magnetic measurements, a small ac drive magnetic field is superimposed on the dc field, causing a time-dependent moment in the sample. There are two advantages of ac measurements. Firstly, the measurement is very sensitive to small changes in magnetization, as it measures the dM/dH of $M(H)$ curve. Secondly, ac measurements yield information

about magnetization dynamics which are not obtained in dc measurements because the sample moment is constant during the measurement time.

Our ac susceptibility measurements were performed at the National High Magnetic Field Laboratory (NHMFL) using the conventional mutual inductance technique, in collaboration with Minseong Lee and Eun San Choi. The magnetic fields were obtained using an ac-dc current calibrator (Valhalla Scientific, model 2700) and three lock-in amplifiers (Stanford Research, SR 830). The phases of the lock-in amplifiers are set to measure each of the harmonics signals which are shifted from the oscillating magnetic field according to Eq. 2.5. The lock-in amplifiers are also set to read the linear component (first harmonic response) and the nonlinear components (second and third harmonic responses) with respect to the oscillating ac field frequency. The amplitude of the ac excitation field (h_0) varies from 0.43 to 4.3 Oe with frequency (f) ranging from 40 to 1000 Hz. The applied external dc magnetic field (H_{ac}) varies from 0 to 1000 Oe. The data was taken while warming up the sample from the base temperature with a rate of 7.6 mK/min utilizing a zero field cooling process. The linear and nonlinear ac susceptibility values have been scaled by the ac field and ac frequency.

Principally, the magnetization m is expressed as :

$$m = m_0 + \chi_0 h + \chi_1 h^2 + \chi_2 h^3 + ... \tag{2.3}$$

Then, in the ac susceptibility measurements, when applying the magnetic field $h = h_0 \sin \omega t$, the induced voltage E of the pick up coil is given as [72]:

$$E = A\{\chi_0^t h_0 \cos \omega t + \chi_1^t h_0^2 \sin 2\omega t - 3/4\chi_2^t h_0^3 \cos 3\omega t - 1/2\chi_3^t h_0^4 \sin 4\omega t + ...\} \tag{2.4}$$

with

$$\begin{aligned} \chi_0^t &= \chi_0 + 3/4\chi_2 h_0^2 + 5/8\chi_4 h_0^4 + ... \\ \chi_1^t h_0 &= \chi_1 h_0 + \chi_3 h_0^3 + 15/16\chi_5 h_0^5 + ... \\ 3/4\chi_2^t h_0^2 &= 3/4\chi_2 h_0^2 + 15/16\chi_4 h_0^4 + 63/64\chi_6 h_0^6 + ... \end{aligned} \tag{2.5}$$

Here, χ_0^t, $\chi_1^t h_0$, and $3/4\chi_2^t h_0^2$ are the first harmonic, the second harmonic, and the third harmonic component, respectively, that we have measured during the experiments [73]. In this dissertation, we will mainly focus on the linear response (first harmonic). Since the applied ac field h_0 is small, the first harmonic component is similar to the linear ac susceptibility ($\chi_0^t \approx \chi_0$) which we labeled as χ_{ac} in the following.

In the higher frequency case, the magnetization of the sample may lag behind the drive field h. Thus, the ac susceptibility measurement yields two quantities: the magnitude and the phase shift (ϕ). We denote χ'_{ac} ($\equiv \chi_0 \cos\phi$) as the real part, which is the slope of the M(H) curve discussed above, and χ''_{ac} ($\equiv \chi_0 \sin\phi$) as the imaginary part, which indicates dissipative processes in the sample.

2.6 Neutron Scattering

2.6.1 Concepts and Equations

A neutron is charge neutral and carries a spin which allows it to interact with magnetic moments, including those arising from the electron cloud around an atom. This unique property makes it an excellent probe for the determination of the static and dynamic magnetic properties of matter. The principal aim of a neutron scattering experiment is the determination of the probability that a neutron which is incident on the sample with wave-vector $\mathbf{k}$ scatters with wave-vector $\mathbf{k'}$. During a scattering process, a neutron exchanges energy and momentum with the material. Due to energy and momentum conservation, the momentum and energy transfer to the sample is $\mathbf{Q} = \mathbf{k}$ - $\mathbf{k'}$ and $\hbar\omega = \frac{\hbar^2}{2m}(k^2 - k'^2)$, respectively. Depending on whether the energy transfer is zero or not, the neutron scattering experiments can be divided into two categories: elastic scattering and inelastic scattering. Both of these techniques have been used in Chapter five when studying the magnetism of $Mg_2Ho_3Sb_3O_{14}$. Here, I will focus on the magnetism and make a brief introduction of the magnetic scattering. In this section, all of the principle equations can be found in a stadard neutron scattering textbook [74].

For unpolarized neutrons, identical magnetic ions with localized electrons, the spin-only magnetic scattering cross section is:

$$\frac{d^2\sigma}{d\Omega d\omega} = (\gamma r_0)\,\frac{2k'}{k}F^2\left(\mathbf{Q}\right)e^{-2W(\mathbf{Q})}\sum_{\alpha\cdot\beta}\left(\delta_{\alpha\beta}-\frac{Q_\alpha Q_\beta}{Q^2}\right)S^{\alpha\beta}\left(\mathbf{Q},\omega\right), \tag{2.6}$$

where γ = -1.91 is the gyromagnetic ratio of the neutron moment, r_0^2 is the nuclear cross section, $F(\mathbf{Q})$ is the magnetic form factor that usually falls off with increasing $|\mathbf{Q}|$, $e^{-2W(\mathbf{Q})}$ is the Debye-Waller factor, and $S^{\alpha\beta}\left(\mathbf{Q},\omega\right)$ is the magnetic scattering function. It is noteworthy that the polarization factor $\left(\delta\alpha_{13}-\frac{Q_\alpha Q_B}{Q^2}\right)$ tells us that neutrons can only couple to the magnetic moments or spin fluctuations that are perpendicular to $\mathbf{Q}$ which allows unambiguous determination of the moment directions. The $S^{\alpha\beta}\left(\mathbf{Q},\omega\right)$ in the integral representation is given by:

$$S^{\alpha\beta}\left(\mathbf{Q},\omega\right)=\frac{1}{2\pi\hbar}\sum_{j,j'}\int_{-\infty}^{\infty}e^{i\mathbf{Q}\left(\mathbf{R}_i-\mathbf{R}'_j\right)}\left\langle\widehat{S}_j^{\alpha}\left(0\right)\widehat{S}_j^{\beta}\left(t\right)\right\rangle e^{-i\omega t}dt. \tag{2.7}$$

where $\left\langle\widehat{S}_j^{\alpha}\left(0\right)\widehat{S}_j^{\beta}\left(t\right)\right\rangle$ describes the thermal average of the time-dependent spin operators, and $\mathbf{R}_j$ is the coordination of the magnetic moment at site j. It is clear then that a neutron scattering experiment measures the Fourier transform of the pair correlation function in space and time. Physically speaking, the neutron may be considered as a magnetic probe which establishes the momentum- and energy-dependent magnetic field and detects the response in the scattering sample. We can thereby relate the magnetic scattering function to a generalized dynamic susceptibility ($\chi^{\alpha\beta}\left(\mathbf{Q},\omega\right)$) by the fluctuation-dissipation theorem:

$$S^{\alpha\beta}\left(\mathbf{Q},\omega\right)=\frac{N\hbar}{\pi}\left(1-\exp\left(-\frac{\hbar\omega}{k_BT}\right)\right)^{-1}\operatorname{Im}\chi^{\alpha\beta}\left(\mathbf{Q},\omega\right). \tag{2.8}$$

Lastly, in the inelastic neutron scattering experiments, the energy transfer $\hbar\omega$ can be either positive or negative. According to Boltzmann statistics, there is a scattering law of $S(\mathbf{Q},\omega)$ upon time reversal, known as principle of detailed balance, such that:

$$S\left(-\mathbf{Q},-\omega\right)=\exp\left(-\frac{\hbar\omega}{k_BT}\right)S\left(\mathbf{Q},\omega\right). \tag{2.9}$$

It unambiguously relates the neutron energy-gain and energy-loss processes to each other.

2.6.2 Powder Neutron Diffraction

Neutron diffraction or elastic neutron scattering is the application of neutron scattering to the determination of the atomic and/or magnetic structure of a material. The technique is similar to XRD, but with the additional ability to reveal the microscopic magnetic structure of a material. In order to probe the magnetic ground state, we carried out powder neutron diffraction measurements using the HB-2A high-resolution powder diffractometer [75] at the High Flux Isotope Reactor at Oak Ridge National Laboratory.

The HB-2A Neutron Powder Diffractometer is a workhorse instrument used to conduct crystal and magnetic structural studies of powdered and ceramic samples as a function of intensive conditions (such as temperature, pressure, and magnetic field). Powder diffraction data collected on this instrument are ideally suited for the Rietveld method. The diffractometer has a Debye-Scherrer geometry. The detector bank has 44 3He tubes with 12' Soller collimators. A germanium wafer-stack monochromator is vertically focusing and provides one of three principal wavelengths depending on which reflection is in the diffracting condition: (113) 2.41 Å, (115) 1.54 Å, or (117) 1.12 Å. The take-off angle from the monochromator is fixed at 90°, and the minimum peak full width at half maximum (FWHM) is 0.2°. There are two choices of premonochromator collimation ($\alpha 1$ = 12' or open) and three choices of pre-sample collimation ($\alpha 2$ = 16', 21', or 31') that allow the operation of the instrument in high-resolution or high-intensity modes.

Measurements on 5g $Mg_2Ho_3Sb_3O_{14}$ powder sample were performed in a cylindrical copper container. Neutron wavelengths of 1.546 Å and 2.410 Å were used, produced by the (115) and (113) reflections of a vertically focusing Ge monochromator, respectively. The shorter wavelength, with a higher intensity and Q-coverage, was used to determine the crystal structure, and the longer wavelength, with a better Q resolution, was used to measure the magnetic diffuse scattering between temperatures of 0.4 K and 40 K.

2.6.3 Inelastic Neutron Scattering

Inelastic neutron scattering experiments measure the magnetic scattering function S($\mathbf{Q}$, ω) (Eq. 2.7) of a target material with certain a momentum transfer ($\mathbf{Q}$) and energy transfer ($\hbar\omega$). Inelastic scattering experiments normally require a monochromatization of the incident or outgoing beam and an energy analysis of the scattered neutrons. This can be done either through time-of-flight techniques (neutron time-of-flight scattering) or through Bragg reflection from single crystals (neutron triple-axis spectroscopy and neutron backscattering) [74]. In this dissertation, inelastic neutron scattering measurements were performed to probe the high energy CEF transitions as well as the low energy collective spin excitations. They are measured with two time-of-flight instruments, the Fine-Resolution Fermi Chopper Spectrometer (SEQUOIA) [76] at the Spallation Neutron Source (SNS) of Oak Ridge National Laboratory and the Disk Chopper Spectrometer (DCS) [77] at the NIST Center for Neutron Research, respectively.

The SEQUOIA instrument is a direct geometry time-of-flight chopper spectrometer with fine energy transfer and wave-vector resolution capabilities used for forefront research on dynamical processes in materials. In particular, SEQUOIA allows for unprecedented high-resolution inelastic neutron scattering studies of magnetic excitations and lattice vibrations. SEQUOIA has a 5.5 m flight path from the sample to detector bank. This detector bank currently covers scattering angles from -30 to 60 in the horizontal and from -18 to 18 in the vertical in increments of $\sim$0.3°. Therefore the total solid angle coverage is .863 steradians. SEQUOIA uses the full source spectrum provided by the decoupled water moderator, and can be used to study excitations on energy scales ranging from a few millielectron volts up to several electron volts as a result. For our SEQUOIA measurements, a $\sim$ 5 g powder sample of $Mg_2Ho_3Sb_3O_{14}$ was loaded in an aluminum sample holder and cooled down to 4 K with a closed cycle refrigerator. In order to probe all possible CEF excitations, several incident neutron energies were used, with E_i = 240, 120, 60, and 8 meV in the high resolution mode. The same measurements were repeated for an empty aluminum sample holder that was used for background subtraction.

The DCS is a direct geometry time-of-flight spectrometer which is primarily used for studying of low energy excitations and quasielastic neutron scattering. Neutrons with a single well-defined energy arrive at the sample in pulses. The energies that the neutrons acquire, having been scattered by the sample, are determined from their times of flight to an array of detectors. A cleanpulsed monochromatic neutron beam is produced using seven disk choppers which produce neutron incident wavelengths ranging from 0.23 to 1.0 nm, i.e. ∼2.3 to ∼10 Å. Each of the pulsing and monochromating choppers has three slots of different widths. This permits three choices of resolution at a given wavelength and master chopper speed. The chopper phase stability, approximately 100-200 ns at 20000 rpm, is excellent. For our DCS measurements, a $\sim$ 5 g powder sample of $Mg_2Ho_3Sb_3O_{14}$ was loaded in a copper can and cooled down to the millikelvin regime using a dilution refrigerator. The measurements were carried out with an incident neutron wavelengths of 5 $\mathring{A}$ in the high flux mode at $T = 0.12$, 0.40, 1.6, 4.2, 10.0, and 40.0 K. Due to the large specific heat and related relaxation process below 1 K, a long period of thermal stabilization time was required. The equilibrium was reached $\sim$ 6 h after the temperature of the mixing chamber reaches base, as the intensities of the magnetic Bragg peaks saturate and do not change over time.

For both measurements, all data were corrected for detector efficiency using a vanadium standard, normalized to incident beam monitor (DCS) or beam current (SEQUOIA), and corrected for absorption by the sample. Data reduction was performed using the DAVE programs [78].

Chapter 3

General Considerations

Since we are studying a number of new compounds with a hitherto unstudied frustrating lattice, it is necessary to consider all of the compounds as a family group and then to discuss the family's basic properties. This chapter intends to provide some general considerations of the TKL family before going into the physics of any specific compound. This includes the structure, the unique "tripod" spin anisotropies, and the general spin Hamiltonian. Since the TKL is achieved through partial ion substitution in the pyrochlore structure, these aspects are compared to the parent pyrochlore structure. **For simplification, in the following dissertation, we use the abbreviated name A-RE for the TKLs such as MgPr for $\mathbf{Mg_2Pr_3Sb_3O_{14}}$.**

3.1 Structure

The $A_2RE_3Sb_3O_{14}$ (A = Mg, Zn; RE = Pr, Nd, Gd, Tb, Dy, Ho, Er, Yb) compounds crystallize in a rhombohedral structure with the R -3m space group in hexagonal expression. Compared with the pyrochlore lattice, the triangular layers of both the RE^{3+} and Sb^{5+} sublattices in the structure are replaced by Mg^{2+} or Zn^{2+} The replacement is also possible for other magnetic transition metal ions such as Co^{2+} and Mn^{2+} [79, 80, 81]. The chemical formula can also be written as $(A_{0.25}RE_{0.75})_2(A_{0.25}Sb_{0.75})_2O_7$, which is a pyrochlore ($RE_2X_2O_7$) with one-quarter of the RE^{3+} and X^{4+} ions substituted in an ordered manner (Fig. 3.1(b)). It is noteworthy that for the XRD pattern 3.2, the strongest peak for

pyrochlore at $2\theta \sim 30^\circ$ disappears completely and splits into two peaks, providing evidence for the absence RE-Sb site-disorder. As shown in the chapter four, the $C(T)$ peaks at their phase transitions are very sharp, further underscoring the high degree of site order in the kagome layers. This good kagome layer separation is likely due to the large ion size difference between Mg^{2+} (Zn^{2+}) and RE^{3+}. In this structure, the nearest neighbor distance between the RE^{3+} ions within a kagome layer remains similar to that of its pyrochlore cousin, and the RE^{3+}-kagome layers are well isolated from each other by the non-magnetic $Mg^{2+}Zn^{2+}$, Sb^{5+} layers. Take $Mg_2Gd_3Sb_3O_{14}$ for example, the nearest Gd-Gd distance within a kagome layer (3.678 Å) is similar to the distance in $Gd_2Ti_2O_7$ (3.600 Å), and much smaller than the distance between different planes (6.162 Å). Since the dipolar energy goes as $1/r^3$, this leads to inter-layer energies an order of magnitude smaller than the intra-layer energies.

For the A = Mg branch, XRD patterns of all eight compounds (RE = Pr, Nd, Gd, Tb, Dy, Ho, Er, Yb) can be precisely fitted using the TKL structure. The XRD patterns for two end members, MgPr and MgYb with the largest and smallest RE ionic radius among those we prepared, respectively, are shown in Fig. 3.2 (a) and (b). The associated crystallographic table with selected bond lengths is listed in Table. 3.1. As shown in Fig. 3.3, the lattice parameters decrease smoothly as the RE ionic radius decreases, which is in agreement with a previous report [82].

For the A = Zn branch, the XRD patterns for compounds with larger RE ionic radii (RE = Pr, Nd, Gd, Tb, Dy) closely correspond to the TKL structure; on the other hand, some discrepancies are observed for compounds with smaller ionic radii (RE = Ho, Er, Yb). This finding agrees with a previous report in which attempts to synthesize materials with the TKL structure based on smaller rare earth ions were unsuccessful [81]. For comparison, the XRD patterns for two compounds with nearby RE^{3+} ions on the periodic table, ZnDy and ZnHo, are plotted in Fig. 3.2 (c) and (d). In general, the XRD pattern of ZnHo is similar to that of ZnDy in terms of the positions and intensity ratios of the main reflections. However, some weak reflections observed in ZnDy, such as the (012), (110), and (104) Bragg peaks (marked by the arrows in Fig. 3.2(d)), are not present in the ZnHo data.

The difference between ZnDy and ZnHo can be explained by Zn/Ho site disorder. As both compounds have similar TKL structures, it is the site mixing of the Zn and Ho ions that

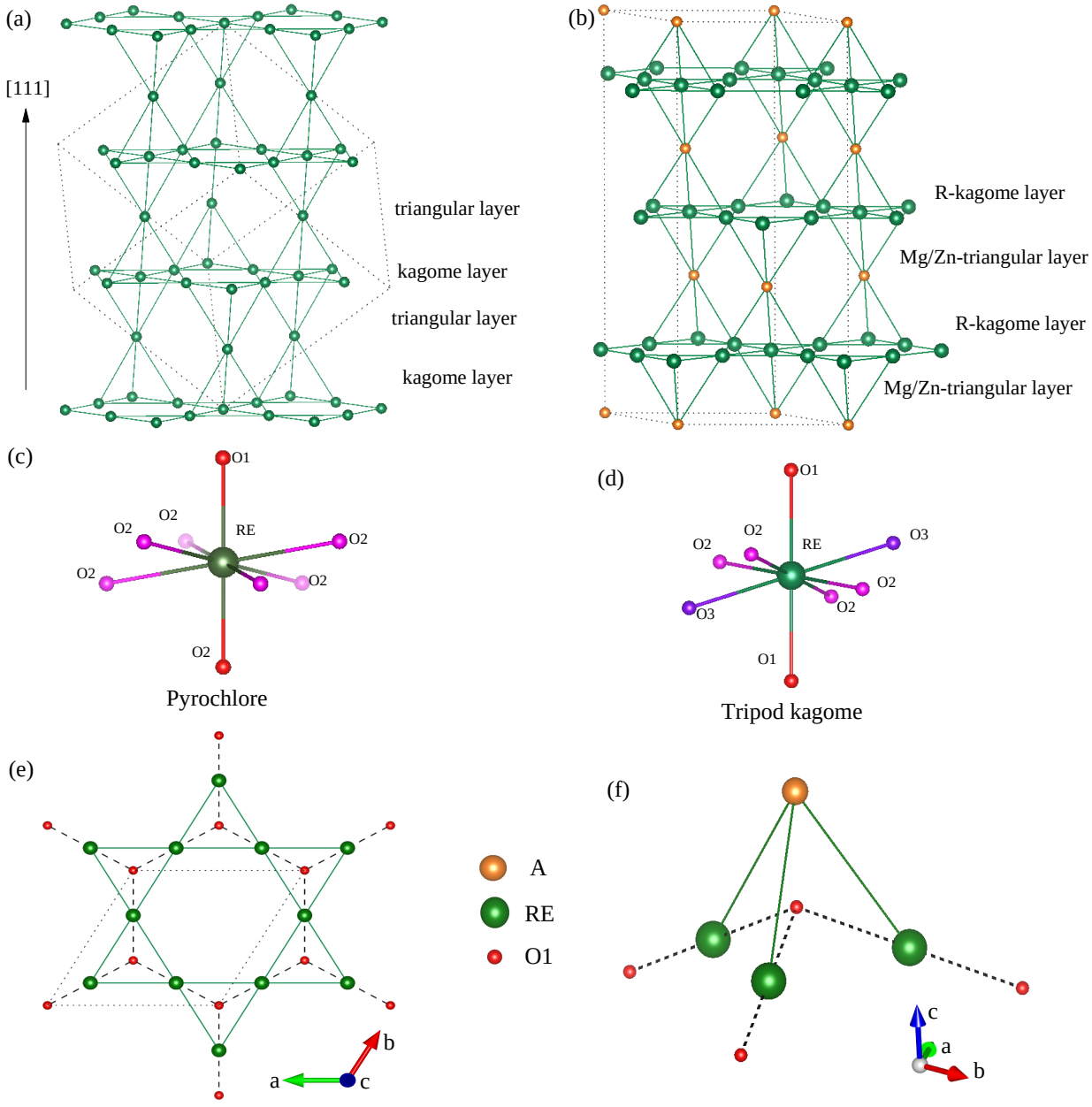

Figure 3.1: (a) Alternating kagome and triangular layers in a pyrochlore lattice. (b) Alternating RE-kagome and Mg-triangular layers in a TKL. Dashed lines indicate a single unit cell. Local oxygen environments around RE^{3+} for (c) pyrochlore and (d) TKL. (e) A single kagome layer with surrounding O1 in a TKL. (d) A single "tripod". Dashed lines represent Ising axes.

reduces the distinctness of their original positions, increases the crystallographic symmetries, and results in a reduction of the number of Bragg reflections. Assuming total site mixing of Zn/Ho with 40% Zn and 60% Ho occupancy at their original Wyckoff site in a TKL, an XRD simulation will give zero intensity for the (012), (110), (104) Bragg peaks if one ignores the weak scattering from oxygen. As shown in Fig. 3.2(d), a Rietveld refinement based on a total Zn/Ho site disorder model fits the XRD pattern reasonably well except for a few small discrepancies. It is noteworthy that the refinements do not give stable oxygen positions, and there are tiny peaks (less than 1% of the intensity of the strongest peak) that cannot be indexed by the TKL structure. This means that although the Zn/RE site order model catches the main feature of the XRD pattern, it is possible that there are hidden orders of the lattice which are beyond our model. For the lattice parameters (Fig. 3.3), a clear jump is observed between ZnDy and ZnHo for a, showing that site disorder expands the lattice within the ab plane. Such site disorder is not totally unexpected when we move from lower to higher Z in the $4f$ row. As we do so, the ionic radius of RE^{3+} decreases, and finally at Ho, it becomes insufficient to be distinguished from the Zn^{2+} ions during the sample synthesis at high temperature. Similar behavior has been reported for $Ca_2RE_3Sb_3O_{14}$ where the Ca/RE site disorder is present for all RE compounds of the Ca branch [83]. In order to distinguish these site-disordered lattices from other site-ordered ones, we will add a notation "$*$" before the chemical formula for disordered lattice (e.g. $*$ZnHo) in the following sections. It is also possible that some slight A/RE disorder exists in the other compounds. Within the experimental resolution, the refinements based on our XRD patterns generally give 0-5% A/RE site disorder for other TKL members of the Zn branch (RE = Pr, Nd, Gd, Tb, Dy) and all TKLs of the Mg branch.

Similar to the disorder effects found in other frustrated magnets, such A/RE site disorder in the TKL structure is likely to modify the spin-spin correlations and tune the fragile low-temperature ground state. As shown in the following chapter, the total Zn/Er disorder in $*$ZnEr results in a spin glass (SG) ground state. It is also noteworthy that a small level of site disorder is likely plays an important role. For example, by comparing two separate reports of MgDy, the difference of the ECO ordering temperatures ($\sim$ 0.3 K in Ref. [9], $\sim$ 0.37 K in our report) and the sharpness of the transition peaks in $C(T)$ can be attributed to

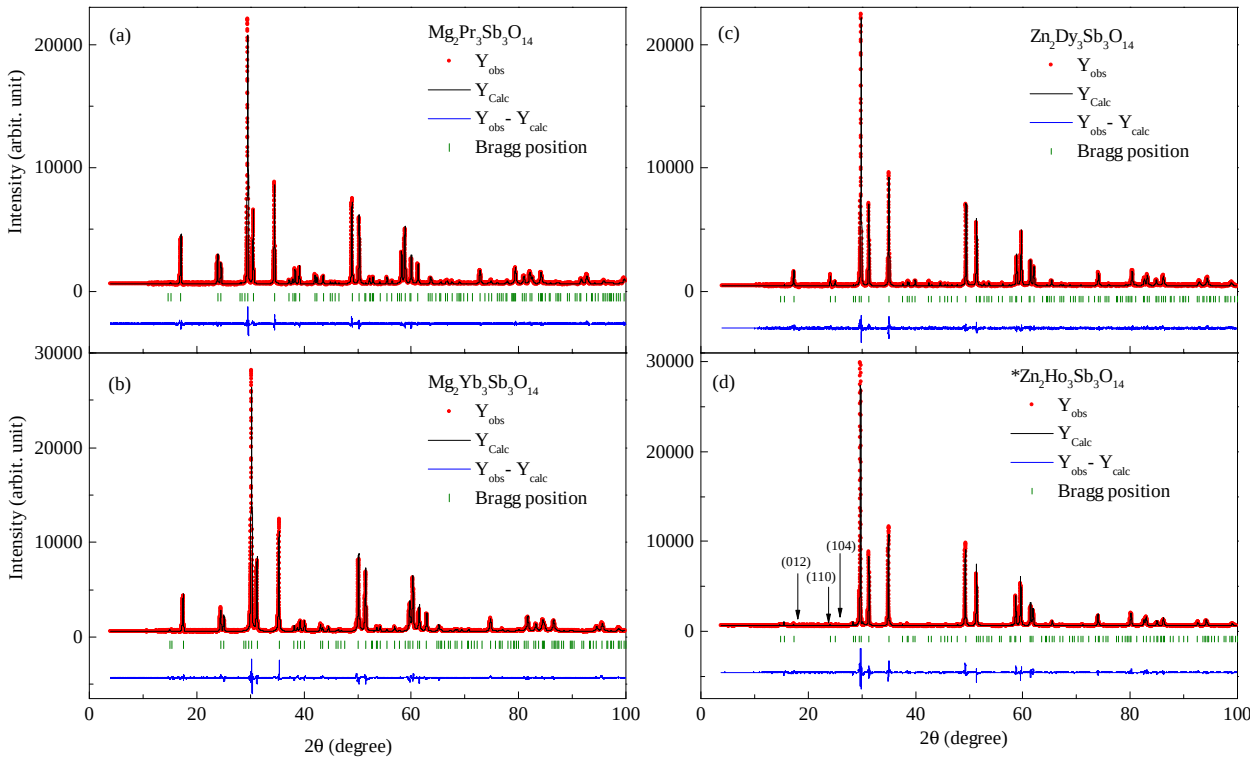

Figure 3.2: XRD patterns and best fits from Rietveld refinements of two end members in the Mg branch for (a) MgPr and (b) MgYb. XRD patterns and best fits from Rietveld refinements of two TKLs in the Zn branch with nearby RE ions in the periodic table, (c) ZnDy and (d)∗ZnHo. Arrows indicates where obvious discrepancies are observed.

the different percentages of Mg/Dy site disorder which might come from different reaction environments during sample synthesis.

3.2 "Tripod" Spin Anisotropies

In the pyrochlore $RE_2X_2O_7$, one important structural feature is that each RE^{3+} ion is surrounded by eight oxygen atoms (3.1(c)) with two shorter RE-O1 bonds lying along the local-[111] axis, and six longer RE-O2 bonds forming a puckered ring. This feature defines the CEF and the g-factor which determines the ionic anisotropy for the RE^{3+} spins. In the TKL, this local oxygen coordination is largely preserved. The RE ion is still surrounded by eight oxygens with the two shortest RE-O1 bonds lying along the local-[111] axis (3.1(d)). The difference is that the longer six RE-O bonds are divided into two sets: four longer RE-O2 bonds and two intermediate RE-O3 bonds (see Tab. 3.1 for detailed bond lengths). As shown

Table 3.1: Summary of room temperature XRD pattern refinements for $A_2R_3Sb_3O_{14}$ (A = Mg, Zn; RE = Pr, Nd, Gd, Tb, Dy, Ho, Er, Yb)

A = Mg	Pr	Nd	Gd	Tb	Dy	Ho	Er	Yb
IR (RE^{3+}) (Å)	1.266	1.249	1.193	1.180	1.167	1.155	1.144	1.125
a (Å)	7.44347(3)	7.43899(8)	7.35505(6)	7.33201(3)	7.31781(9)	7.30817(8)	7.29484(9)	7.26659(2)
c (Å)	17.55855(18)	17.54255(18)	17.35073(14)	17.31816(35)	17.29602(22)	17.26724(19)	17.23451(21)	17.17256(27)
Mg1(3a)	(0, 0, 0)	(0, 0, 0)	(0, 0, 0)	(0, 0, 0)	(0, 0, 0)	(0, 0, 0)	(0, 0, 0)	(0, 0, 0)
Mg2(3b)	(0, 0, $\frac{1}{2}$)	(0, 0,$\frac{1}{2}$)	(0, 0, $\frac{1}{2}$)	(0, 0, $\frac{1}{2}$)	(0, 0, $\frac{1}{2}$)	(0, 0, $\frac{1}{2}$)	(0, 0, $\frac{1}{2}$)	(0, 0, $\frac{1}{2}$)
RE (9d)	($\frac{1}{2}$, 0, $\frac{1}{2}$)	($\frac{1}{2}$, 0, $\frac{1}{2}$)	($\frac{1}{2}$, 0, $\frac{1}{2}$)	($\frac{1}{2}$, 0, $\frac{1}{2}$)	($\frac{1}{2}$, 0, $\frac{1}{2}$)	($\frac{1}{2}$, 0, $\frac{1}{2}$)	($\frac{1}{2}$, 0, $\frac{1}{2}$)	($\frac{1}{2}$, 0, $\frac{1}{2}$)
Sb (9e)	($\frac{1}{2}$, 0, 0)	($\frac{1}{2}$, 0, 0)	($\frac{1}{2}$, 0, 0)	($\frac{1}{2}$2, 0, 0)	($\frac{1}{2}$2, 0, 0)	($\frac{1}{2}$, 0, 0)	($\frac{1}{2}$, 0, 0)	($\frac{1}{2}$, 0, 0)
O1 (6c)	(0, 0, z)	(0, 0, z)	(0, 0, z)	(0, 0, z)	(0, 0, z)	(0, 0, z)	(0, 0, z)	(0, 0, z)
z	0.1043(5)	0.1078(4)	0.1031(5)	0.0986(6)	0.0940(5)	0.1085(5)	0.1152(5)	0.1175(5)
O2 (18h)	(x, $\bar{x}$, z)	(x, $\bar{x}$, z)	(x, $\bar{x}$, z)	(x, $\bar{x}$, z)	(x, $\bar{x}$, z)	(x, $\bar{x}$, z)	(x, $\bar{x}$, z)	(x, $\bar{x}$, z)
x	0.5293(4)	0.5275(3)	0.5320(3)	0.5344(4)	0.5372(3)	0.5323(4)	0.5357(3)	0.5249(4)
z	0.8907(3)	0.8914(2)	0.8951(3)	0.8964(3)	0.8980(3)	0.8968(3)	0.8983(3)	0.8959(3)
O3 (18h)	(x, $\bar{x}$, z)	(x, $\bar{x}$, z)	(x, $\bar{x}$, z)	(x, $\bar{x}$, z)	(x, $\bar{x}$, z)	(x, $\bar{x}$, z)	(x, $\bar{x}$, z)	(x, $\bar{x}$, z)
x	0.4703(4)	0.4708(3)	0.4754(4)	0.4753(5)	0.4765(4)	0.4769(4)	0.4751(3)	0.4719(4)
z	0.3566(3)	0.3558(2)	0.3578(2)	0.3591(3)	0.3586(2)	0.3596(2)	0.3580(2)	0.3523(2)
RE-O1 (Å)	2.412(4)	2.383(4)	2.393(4)	2.423(6)	2.458(5)	2.337(4)	2.285(4)	2.261(4)
RE-O2 (Å)	2.566(4)	2.556(2)	2.587(3)	2.606(4)	2.634(3)	2.586(4)	2.616(3)	2.513(3)
RE-O3 (Å)	2.547(6)	2.557(4)	2.487(4)	2.460(6)	2.462(4)	2.442(4)	2.467(4)	2.561(6)
Intralayer RE-RE	3.72174(4)	3.71950(5)	3.67753(4)	3.66601(8)	3.65891(5)	3.65409(5)	3.64742(5)	3.63330(6)
Interlayer RE-RE	6.23482(6)	6.22936(6)	6.16099(5)	6.14852(9)	6.14016(7)	6.13020(6)	6.11863(7)	6.09645(10)
Overall B ($Å^2$)	1.39(1)	1.55(1)	1.45(1)	1.51(2)	1.43(1)	1.58(1)	1.55(1)	1.48(2)
R_p	3.24	2.05	2.32	3.65	2.93	3.37	3.54	2.94
R_{wp}	3.55	2.05	3.42	4.56	3.43	3.72	3.31	3.16
χ^2	2.62	1.15	1.17	1.51	1.24	3.89	3.60	2.27

A = Zn	Pr	Nd	Gd	Tb	Dy	Ho	Er	Yb
IR (R^{3+}) (Å)	1.266	1.249	1.193	1.180	1.167	1.155	1.144	1.125
a (Å)	7.47622(9)	7.46151(10)	7.40270(11)	7.378569(11)	7.36714(12)	7.38639(3)	7.37040(3)	7.35212(2)
c (Å)	17.42042(21)	17.36332(22)	17.20519(26)	17.15565(26)	17.11680(29)	17.09436(7)	17.04657(7)	16.97254(6)
Zn1(3a)	(0, 0, 0)	(0, 0, 0)	(0, 0, 0)	(0, 0, 0)	(0, 0, 0)	disorder	disorder	disorder
Zn2(3b)	(0, 0, $\frac{1}{2}$)	(0, 0, $\frac{1}{2}$)	(0, 0, $\frac{1}{2}$)	(0, 0, $\frac{1}{2}$)	(0, 0, $\frac{1}{2}$)	disorder	disorder	disorder
RE (9d)	($\frac{1}{2}$, 0, $\frac{1}{2}$)	($\frac{1}{2}$, 0, $\frac{1}{2}$)	($\frac{1}{2}$, 0, $\frac{1}{2}$)	($\frac{1}{2}$, 0, $\frac{1}{2}$)	($\frac{1}{2}$, 0, $\frac{1}{2}$)	disorder	disorder	disorder
Sb (9e)	($\frac{1}{2}$, 0, 0)	($\frac{1}{2}$, 0, 0)	($\frac{1}{2}$, 0, 0)	($\frac{1}{2}$, 0, 0)	($\frac{1}{2}$, 0, 0)	($\frac{1}{2}$, 0, 0)	($\frac{1}{2}$, 0, 0)	($\frac{1}{2}$, 0, 0)
O1 (6c)	(0, 0, z)	(0, 0, z)	(0, 0, z)	(0, 0, z)	(0, 0, z)	(0, 0, z)	(0, 0, z)	(0, 0, z)
z	0.1105(7)	0.1063(8)	0.1084(8)	0.1061(8)	0.1057(9)	-	-	-
O2 (18h)	(x, $\bar{x}$, z)	(x, $\bar{x}$, z)	(x, $\bar{x}$, z)	(x, $\bar{x}$, z)	(x, $\bar{x}$, z)	(x, $\bar{x}$, z)	(x, $\bar{x}$, z)	(x, $\bar{x}$, z)
x	0.5183(5)	0.5206(5)	0.5180(5)	0.5212(5)	0.5178(6)	-	-	-
z	0.8890(3)	0.8902(4)	0.8888(3)	0.8876(4)	0.8857(4)	-	-	-
O3 (18h)	(x, $\bar{x}$, z)	(x, $\bar{x}$, z)	(x, $\bar{x}$, z)	(x, $\bar{x}$, z)	(x, $\bar{x}$, z)	(x, $\bar{x}$, z)	(x, $\bar{x}$, z)	(x, $\bar{x}$, z)
x	0.4654(4)	0.4644(4)	0.4676(4)	0.4662(4)	0.4668(5)	-	-	-
z	0.3510(3)	0.3554(3)	0.3546(3)	0.3566(3)	0.3544(3)	-	-	-
RE-O1 (Å)	2.370(6)	2.395(7)	2.360(6)	2.370(7)	2.369(7)	-	-	-
RE-O2 (Å)	2.483(4)	2.502(4)	2.454(4)	2.461(4)	2.420(4)	-	-	-
RE-O3 (Å)	2.634(6)	2.553(6)	2.536(6)	2.496(6)	2.528(6)	-	-	-
Intralayer RE-RE	3.73811(3)	3.73076(3)	3.70135(3)	3.68928(6)	3.68357(7)	-	-	-
Interlayer RE-RE	6.19490(7)	6.17561(7)	6.12026(10)	6.10237(10)	6.08907(10)	-	-	-
B ($Å^2$)	1.54(1)	1.52(1)	1.53(1)	1.64(1)	1.66(1)	2.42(2)	2.16(1)	2.17(1)
R_p	3.61	3.11	2.76	3.36	3.28	3.93	4.81	3.61
R_{wp}	5.76	4.92	5.78	5.48	5.32	8.68	9.79	9.73
χ^2	2.00	2.05	1.46	2.45	1.57	2.89	5.28	6.17

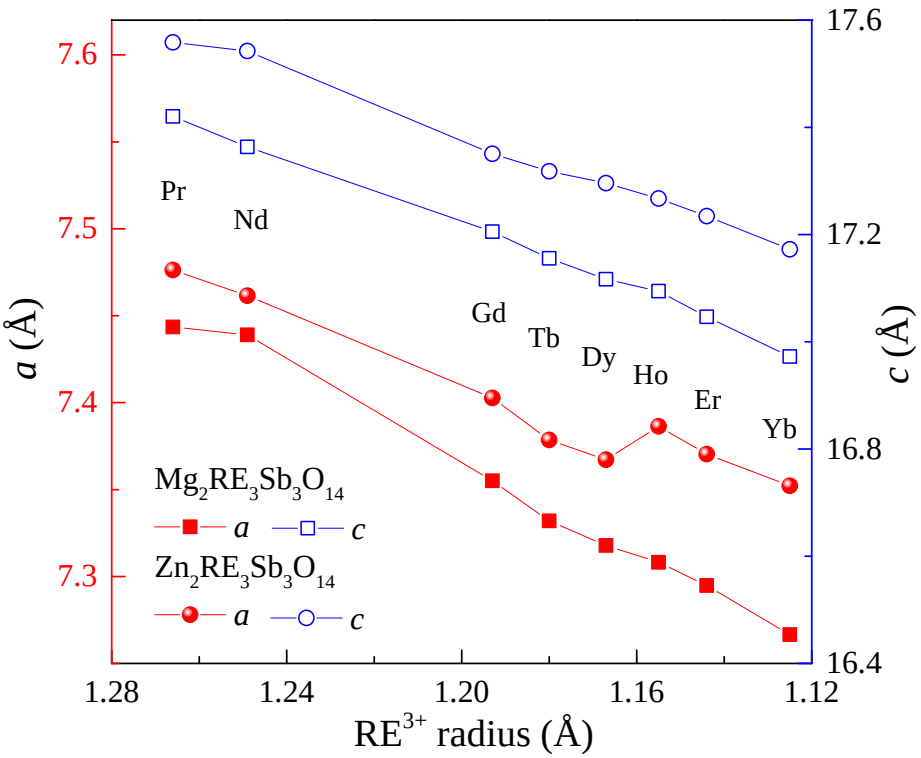

Figure 3.3: Lattice parameters obtained from Rietveld refinements as a function of RE^{3+} ionic radius for all RE members in the Mg and Zn branches of the TKL family.

in the following section, this change reduces the point group of symmetry at the RE site from D_{3d} to C_{2h}, which has an important consequence for the CEF of non-Kramers ions. Generally speaking, since the CEF degeneracy has already been lifted by the pyrochlore-like anisotropy for an effective spin-1/2 system, the dominant anisotropy remains the one distinguishing the puckered ring from the local-[111] oxygen ions, making this in-plane anisotropy most likely irrelevant to the ground state degeneracy. In other words, due to the similar local oxygen environment of the RE ion compared to that of the parent pyrochlore structure, we expect a similar CEF splitting of the $4f$ ground state, resulting in either Ising spins or XY-spin vectors that are neither uniaxial nor uniplanar. As shown in 3.1(f), there are three Ising axes for each kagome layer that are joining each RE ion to the O1 ion that are located at the center of the tetrahedron (thus the local XY plane is the one that is perpendicular to the local Ising axes). It is this lack of a unique crystal axis that is neither parallel nor perpendicular to the individual Ising axes of the distorted RE polyhedra that warrants use of the modifier "Tripod " to avoid confusion with uniaxial (coplanar) kagome lattices. Such

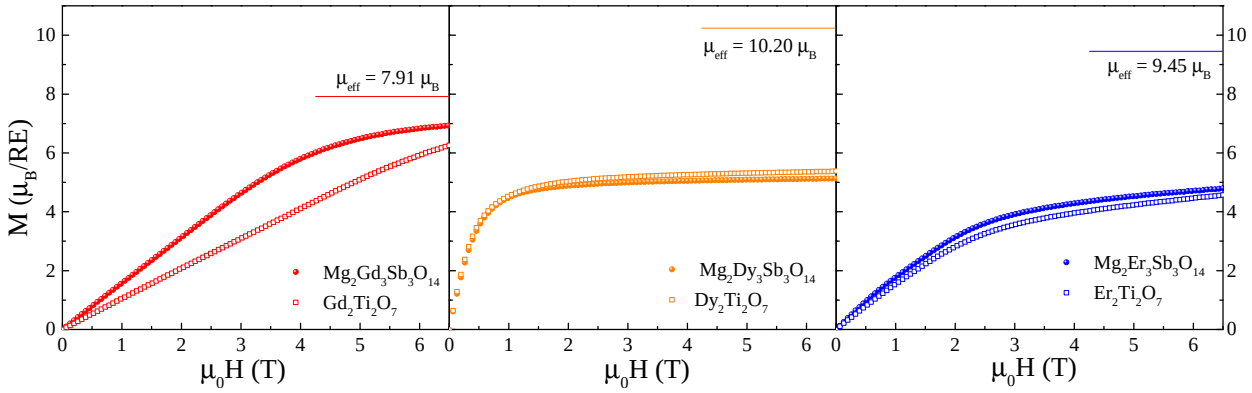

Figure 3.4: Magnetization curves up to 6.5 T measured at $T = 2$ K for $Mg_2RE_3Sb_3O_{14}$ and $RE_2Ti_2O_7$ (RE = Gd, Dy, Er). The μ_{eff} (solid color bar) represents the effective free-ion moment for each RE^{3+} ion.

tripod-like axes will also be crucial for the understanding of the low-temperature magnetism for each RE-TKL.

As discussed in the introduction, with a pyrochlore-like local environment, the eight RE elements studied in this dissertation likely possess three different spin anisotropies, depending on different elements. The Gd^{3+} is the only Heisenberg spin due to the half-filled $4f$ shell. For the Yb^{3+} and Er^{3+}, the CEF is likely giving rise to a local-XY model, where the spins are energetically favored to lie in the local XY-plane perpendicular to the tripod-Ising axes [84]. The remaining five ions (Pr^{3+}, Nd^{3+}, Dy^{3+}, Ho^{3+}, Tb^{3+}) all possess Ising anisotropies. The conjecture of spin anisotropies is confirmed by similar low-temperature magnetization curves between each RE-TKL and its pyrochlore parent. Here, we show the magnetization curves at 2 K for three TKL compounds and their pyrochlore cousins (all in polycrystalline forms) in Fig. 3.4, where apparent similarities are found for all three sample sets.

For Gd-TKL, the magnetization curve shows a straight line up to 3 T which signatures an isotropic g-factor as expected for an S-state of Gd^{3+} (J = 7/2, L = 0). The magnetization reaches 7.0 μ_B/Gd^{3+} (6.4 μ_B/Gd^{3+} for $Gd_2Ti_2O_7$) at 6.5 T, which is about 88.5% of its effective moment. Similar to $Dy_2Ti_2O_7$, strong anisotropic behaviors are observed in Dy-TKL. The magnetization quickly saturates at a plateau of 5.1 μ_B/ Dy^{3+}, about half of its effective moment. In the pyrochlore spin ice, such half magnetization plateau is the characteristic behavior of Dy^{3+} Ising moment [85]. A similar half magnetization plateau observed here provides strong evidence for the local Ising anisotropy for Dy ions in the TKL

system. For Er-TKL, the magnetization reaches 4.8 μ_B/Er^{3+} (4.6 μ_B/Er^{3+} for $Er_2Ti_2O_7$), which is about half of the effective moment per Er ion. Moreover, the magnetization curve of Er-TKL is also similar to that of its pyrochlore cousin $Er_2Ti_2O_7$ for the whole field region from 0 to 6.5 T. This similarity provides supporting evidence for the local XY anisotropy that has been confirmed in the Er pyrochlore.

Finally, it is worth mentioning that for MgHo (see Chapter 5), MgDy [9], and MgNd [86], the observed magnetic Bragg peaks from low-temperature neutron diffraction measurements also support the Ising spin scenario proposed above.

3.3 Hamiltonian

For a rare-earth oxide compound with localized electrons, there are three kinds of interactions that need to be taken into account. They are the CEF term, the dipolar interaction and the exchange interaction, which are written in a Hamiltonian as:

$$H = H_{\mathrm{CEF}} + H_{\mathrm{dip}} + H_{\mathrm{ex}}. \tag{3.1}$$

The H_{CEF} is the CEF term (or crystal potential) that describes the static electric field potential produced by a surrounding charge distribution (anion neighbors). It is also known as the single ion term because the ground state wave functions determine the anisotropic g-factor ($g_\perp$, $g_\parallel$). Since the electrostatic potential energy satisfies the Laplace equation and has the symmetry of the surroundings of the ion, the potential energy thereby can be expanded as a sum of spherical harmonics. In the case of rare earth ions, the perturbations due to the CEFs are usually small compared with the spin-orbit couplings. Therefore, it is appropriate to chose representations in which the states are eigenstates of the total orbital angular momentum (J). For a given J-multiplet, the Hamiltonian is expressed in terms of the Extended Stevens Operators [87] with a general form:

$$H_{\mathrm{CEF}} = \sum_{k=2,4,6} \sum_{q=-k}^{k} B_k^q O_k^q. \tag{3.2}$$

where B_k^q is the Stevens parameters with k being the order (also called rank or degree) for f-electrons and q being the operator range (that varies between -k and k). O_k^q are the Stevens operators which are polynomials of the components of the total angular momentum operator of a rare-earth ion: J_z, J_+ and J ($J_\pm = J_x \pm \mathrm{i}J_y$) [88]. The above Hamiltonian effectively splits each RE^{3+} ground atomic multiplet into $2J+1$ levels. Given a configuration of ligands, if the CEF ground state is a degenerate doublet that is well isolated from above levels, it ensures a pseudo-spin-1/2 description such that the system acts as a canonical two-level system at low temperature. Among the eight RE ions studied in this dissertation, except for Gd which has no CEF effect due to its zero angular momentum, four of them (RE = Nd, Dy, Er, Yb) have a half-integral J (known as Kramers ion), and their single ion ground states are doublets that are restrictedly protected by time-reversal symmetry. Therefore, the pseudo-spin-1/2 picture is automatically guaranteed, and the H_{CEF} term vanishes. On the other hand, the other three (RE = Pr, Tb, Ho) have non-Kramers ions, so the single ion ground states are not necessarily degenerate doublets. In the pyrochlore system, an "accidental" degeneracy of the non-Kramers doublets is usually found due to the protection of a high symmetry point group (D_{3d}) at the RE site. In the TKL compounds, due to the symmetry reduction of the RE site, the CEF levels for non-Kramers ions should split into $2J+1$ singlet levels according to the point group symmetry (C_{2h}) [89]. Since their local oxygen ligands remain closely similar to its pyrochlore parent, the ground state doublet should split into two singlets with a small and finite energy difference. As we will discuss in Chapter 5, as long as the energy splitting is comparable to the spin-spin interactions, the H_{CEF} in this case can be treated as a transverse field.

The second term H_{dip} is the magnetic dipole-dipole interaction. In a TKL, it is given by:

$$H_{\mathrm{dip}} = \frac{1}{2} D_{nn} R_{nn}^3 \sum_{i,j} \left(\frac{\mathbf{S}_i \cdot \mathbf{S}_j}{|\mathbf{R}_{ij}|^3} - \frac{3(\mathbf{S}_i \cdot \mathbf{R}_{ij})(\mathbf{S}_j \cdot \mathbf{R}_{ij})}{|\mathbf{R}_{ij}|^5} \right). \tag{3.3}$$

Here, $D_{nn} = \frac{\mu_0}{4\pi} \frac{\mu_{eff}^2}{R_{nn}^3}$ defines the dipolar energy scale which is proportional to the square of effective moment (μ_{eff}). $\mathbf{R}_{ij}$ is the vector between two spins $\mathbf{S}_i$, $\mathbf{S}_j$, and R_{nn} is the nearest distance between two spins that can be found in 3.1. For ions hosting a large moment, the energy scale of D_{nn} becomes comparable to the exchange interaction. For example,

in pyrochlore spin ices, the dipolar interaction overwhelms the antiferromagnetic exchange interaction, which results in a two-in-two-out ice rule state [15]. It is also noteworthy that the summation of the above Hamiltonian runs over all i, j, illustrating the long range nature of dipolar interactions. In spin ices, the important consequence is that the dipole moment of the underlying electronic degrees of freedom fractionalizes into magnetic monopoles when local defects are present [2]. Therefore, the interaction between the monopoles follows the magnetic Coulomb law, which is also long range in nature.

The third term H_{ex} represents the exchange interaction. It is usually appropriate to consider only the nearest neighbor interaction for rare earth oxides due to strong localization of the $4f$ electrons. Therefore, H_{ex} is given by:

$$H_{ex} = -\frac{1}{2}\sum_{i,j} J_{ij}^{uv} S_i^u S_j^v, \tag{3.4}$$

where $J_{ij}^{uv} = J_{ji}^{vu}$ is the matrix of exchange coupling between site i and j. The exchange matrix has four components which represent Heisenberg exchange, Kitaev exchange, Dzyaloshinskii-Moriya interaction and symmetric off-diagonal terms, respectively. For XY systems, it is almost certain that the anisotropic exchange parameters are playing an important role. However, for Heisenberg spins, we expect isotropic coupling. For Ising spins, there are only Ising exchanges that couple the S^z component of the nearest sites. For the latter two cases, we can reduce the matrix J_{ij}^{uv} into a single value J_{ex}. An estimation of the J_{ex} can be found from the Weiss temperature (θ_W) via a mean field theory [90]:

$$J_{ex} = -\frac{3\theta_W}{zS(S+1)} \tag{3.5}$$

where z is the number of nearest neighbors. In our TKL system, $z = 4$. Since J_{ex} is the effective exchange constant that couples two unit spins, $J_{ex} = JS(S+1)$. Because of the large spin moment in the RE-oxide systems, the measured θ_W has the contribution from both the exchange and the dipolar parts. As a simple approximation, one can estimate the

exchange contribution by subtracting θ_W by the dipolar contribution D_{nn} [91], with

$$J_{ex} = -\frac{3}{4}(\theta_W - D_{nn}). \tag{3.6}$$

Thus an estimation of the J_{ex} can be found by low temperature dc susceptibility measurement. For example, for MgDy, with θ_W = -0.12 K and μ_{eff} = 10.2 μ_B, we get D_{nn} = 1.31 K and J_{ex} = 1.12 K.

Chapter 4

Magnetic Ground States: A Susceptibility and Specific Heat Survey

The main results in this chapter, along with the results from the previous chapter, have produced two scientific publications: (i) Z. L. Dun, *et al.*, Phys. Rev. Lett. **116**, 157201 (2016) [**Editor's Suggestion**], and (ii) Z. L. Dun, *et al.*, Phys. Rev. B **95**, 104439 (2017).

In this Chapter, I shall provide a comprehensive study of the magnetic properties of two branches of the rare earth TKL family $A_2RE_3Sb_3O_{14}$ (A = Mg, Zn; RE = Pr, Nd, Gd, Tb, Dy, Ho, Er, Yb) with non-magnetic A sites. By combining the experimental probes of dc, ac susceptibility and specific heat, we show various magnetic ground states for TKLs with different RE ions. These include (i) the non-magnetic singlet state for MgPr and ZnPr, (ii) long range orderings (LROs) for MgGd, ZnGd, MgNd, ZnNd, and MgYb, (iii) a long range magnetic charge ordered state for MgDy, ZnDy, and potentially for MgHo, (iv) possible spin glass states for ZnEr, ZnHo, (v) the absence of spin ordering down to 80 mK for MgEr, MgTb, ZnTb, and ZnYb compounds. These ground states are compared to their pyrochlore parents and are discussed in terms of their spin anisotropies, CEF ground states, and chemical pressure effects. I will begin with a case-by-case study of the magnetic properties and end with discussions. The results for compounds with the same RE ion will be combined as sets.

4.1 Magnetic Properties

4.1.1 $Mg_2Pr_3Sb_3O_{14}$ and $Zn_2Pr_3Sb_3O_{14}$

For MgPr, a CW fit of $1/\chi_{dc}$ from 150 K to 300 K (Fig. 4.1 (a)) yields a Weiss temperature, θ_W = -46.18 K and an effective magnetic moment, μ_{eff} = 3.40 μ_B. For ZnPr, a similar fit yields θ_W = -68.43 K and μ_{eff} = 3.61 μ_B. These μ_{eff} values are consistent with the free ion moment of μ_{eff} = 3.58 μ_B expected for Pr^{3+} ions. Below 50 K, $1/\chi_{dc}$ becomes flat, followed by another slope change below 10 K (Fig. 4.1 (a) inset), suggesting changes of the magnetic moments and spin-spin interactions in this temperature region due to CEF effects.

For MgPr, a broad feature around 0.35 K is observed at zero field in χ'_{ac} (Fig. 4.2 (a)) while no obvious sign of LRO is observed from χ'_{ac} down to 50 mK. For ZnPr (Fig. 4.2 (b)), LRO is also not observed in χ'_{ac} where a Curie-Weiss type behavior is persistent down to the lowest measured temperature of 0.3 K. For both MgPr and ZnPr, the absolute values of the magnetic specific heat (C_{mag}) below 10 K are extremely small ($<$ 0.1 J/K^2 per mol-Pr), in sharp contrast to those observed in Pr-pyrochlores within the same temperature range ($\sim$ 2 J/K^2 per mol-Pr) [28, 29]. The integrated magnetic entropy (S_{mag}) from 0.35 K to 6 K recovers $\sim$ 0.2 J/K per mol-Pr, a value that is 3% of Rln2 that is expected for a effective spin-1/2 system.

In the Pr-pyrochlore compounds, the single-ion ground state is a non-Kramers doublet with a large Ising-like anisotropy whose first excited CEF level is a non-magnetic singlet that is well separated from the ground state doublet (18 meV in $Pr_2Sn_2O_7$ [28, 92] and 9.5 meV in $Pr_2Zr_2O_7$ [29]). Such effective spin-1/2 Ising systems with antiferromagnetic (antiferromagnetic) exchange interactions give rise to a QSI ground state at low temperature [28, 29] where spin fluctuations from a quantum superposition of the spin ice manifold suppresses LRO.

The small values of C_{mag} and S_{mag} observed in the Pr-TKLs suggest that the lower crystal field symmetry in the TKLs lifts the degeneracy of the low energy states probed in the pyrochlores. As discussed in the previous chapter, with non-Kramers Pr^{3+} ions, the local site symmetry alters the CEF spectrum to mix the doublets and results in a non-magnetic singlet ground state. Such a non-magnetic state is consistent with the small values of C_{mag}

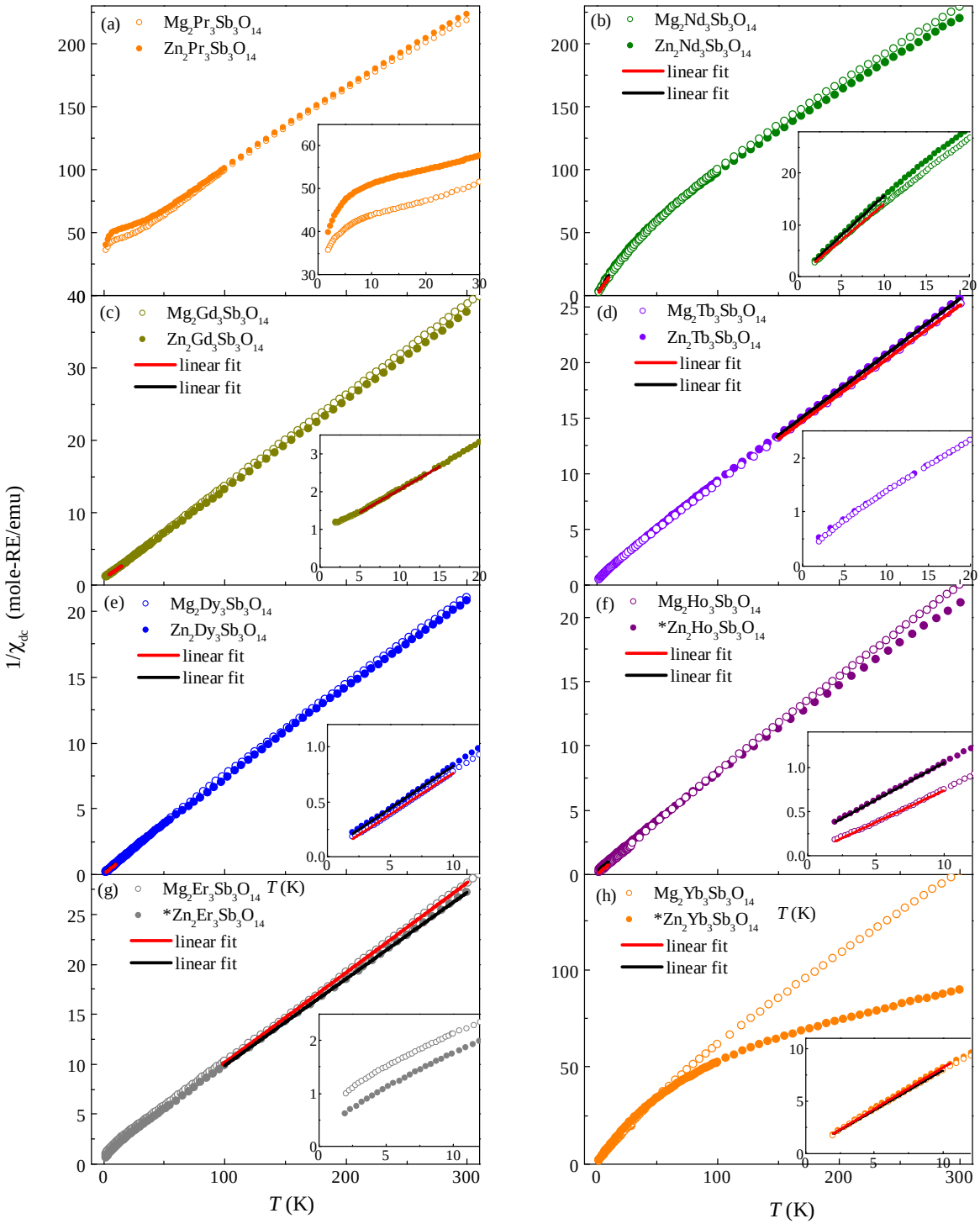

Figure 4.1: (a-h) Inverse χ_{dc} from 2 K to 300 K for all $A_2RE_3Sb_3O_{14}$ (A = Mg, Zn; RE = Pr, Nd, Gd, Tb, Dy, Ho, Er, Yb) compounds. Insets: zoomed in $1/\chi_{dc}$ at low temperature regions.

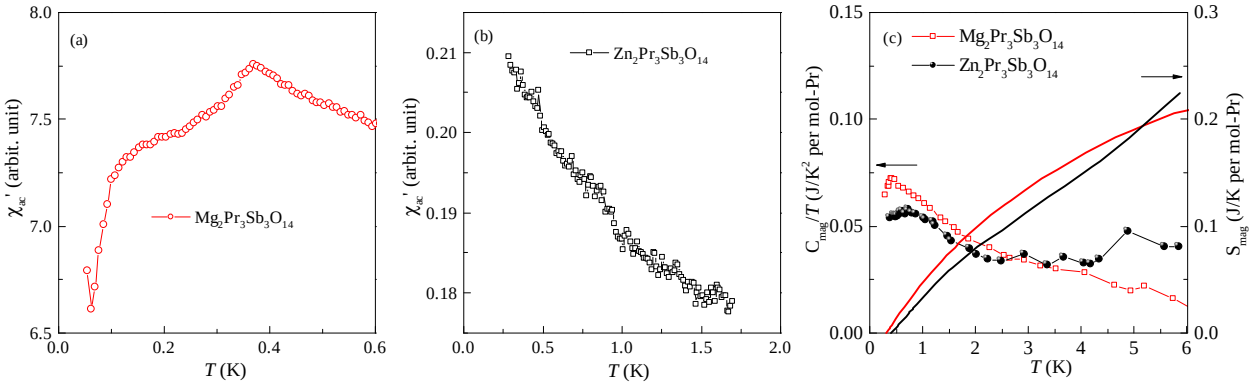

Figure 4.2: Temperature dependence of the real part of χ_{ac} for (a) MgPr, and (b) ZnPr. (c) C_{mag}/T and S_{mag} for both compounds.

and S_{mag}, as well as the flat χ_{dc} (steep $1/\chi_{dc}$) observed at low temperatures (Fig. 4.1 (a)). Therefore, the signals observed in χ'_{ac} of MgPr and ZnPr are likely due to a combination of Van Vleck susceptibility and a contribution from magnetic impurities that is not observed by the XRD.

4.1.2 $Mg_2Nd_3Sb_3O_{14}$ and $Zn_2Nd_3Sb_3O_{14}$

For MgNd, a CW fit from 150 K to 300 K of $1/\chi_{dc}$ yields θ_W = -66.36 K and μ_{eff} = 3.58 μ_B. For ZnNd, a similar fit yields θ_W = -60.47 K and μ_{eff} = 3.60 μ_B. The μ_{eff} values are consistent with the free ion moment of μ_{eff} = 3.62 μ_B expected for Nd^{3+}. A CW fit in the low temperature region (2 K-10 K, Fig. 4.1 (b)) yields θ_W = -0.01 K, μ_{eff} = 2.38 μ_B for MgNd and θ_W = -0.11 K, μ_{eff} = 2.28 μ_B for ZnNd. These numbers are similar to that of the Nd pyrochlores [93, 94] and consistent with a recent report of the MgNd [86].

For MgNd, a broad peak is observed in the zero field χ'_{ac} at 0.49 K, accompanied by a shoulder around 0.55 K (Fig. 4.3 (a)). A small dc-field of 0.03 T reduces its height and separates the positions of these features. With increasing fields, the position of the low temperature peak does not show any obvious field dependence while the shoulder-related peak moves to higher temperatures. In Fig. 4.3 (c), C_{mag}/T of MgNd shows a λ-like peak at 0.55 K, indicating a second order antiferromagnetic LRO transition. For ZnNd, a similar peak in C_{mag}/T is observed at a slightly lower temperature of 0.47 K. Accordingly, a sharp peak is observed at 0.47 K in χ'_{ac} (Fig. 4.3 (a)) at zero field. Similar to that of MgNd, this

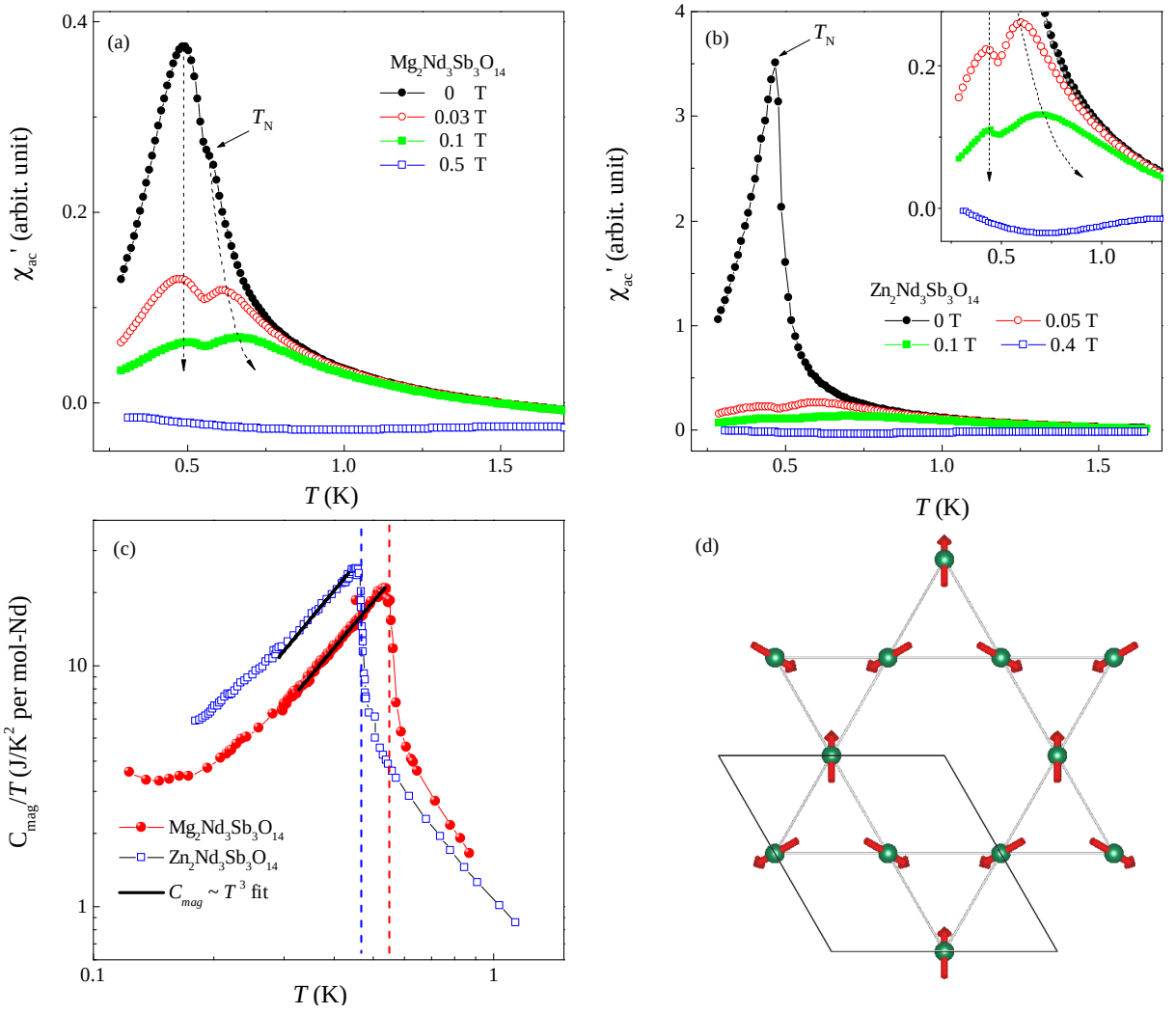

Figure 4.3: Temperature dependence of the real part of χ_{ac} under different dc fields for (a) MgNd and (b) ZnNd. (c) C_{mag}/T on a log-log scale for MgNd and ZnNd. Two $C_{mag} \sim T^3$ fits are shown as black solid lines. (d) The proposed all-in-all-out spin structure in a kagome layer. Black solid lines represent a single unit cell.

peak splits into two when a small dc field is applied (shown in Fig. 4.3 (b) inset). For both compounds, C_{mag} show a T^3 behavior below T_N, consistent with linear dispersive spin wave excitations in three dimensions.

The magnetic ground state for MgNd has been recently studied by Scheie et. al [86], where a second order phase transition with a non-coplanar $k = 0$ spin ordering has been revealed by elastic neutron scattering and $C(T)$ measurements. The proposed spin structure is an all-in-all-out spin state where three spins in each triangle are pointing in or out of the local tripod directions (along RE-O1) simultaneously (Fig. 4.3 (d)). Such a state also resembles the all-in-all-out spin structure for Ising spins on pyrochlore lattices, which has been observed in $Nd_2Sn_2O_7$ [93]. Regarding the double peak feature observed in χ'_{ac}, it is the position of the shoulder at zero field (0.55 K) that agrees with the LRO transition in C_{mag}. Accordingly, the appearance of the 0.47 K peak in χ'_{ac} seems to suggest a two-step transition. Additionally, a closer look at the order parameter scan of the (101) magnetic Bragg peaks from Ref. [86] seems to reveal a slope change around 0.45 K. Another possibility is that, since the lower temperature peak does not appear in C_{mag}/T, the two-step feature could be due to the grain effect, wherein grains with different crystal axes respond differently with respect to the applied magnetic field. For ZnNd, the two-step feature more closely converges in temperature at zero field which can only be distinguished in χ'_{ac} under a smaller dc field. For both compounds, further measurements under a small magnetic field will be helpful to clarify the nature of the two-step transition.

4.1.3 $Mg_2Gd_3Sb_3O_{14}$ and $Zn_2Gd_3Sb_3O_{14}$

For MgGd, a CW fit from 5 K to 15 K of $1/\chi_{dc}$ (Fig.4.1 (c)) yields θ_W = -6.70 K and μ_{eff} = 8.06 μ_B. For ZnGd, a similar fit of $1/\chi_{dc}$ (Fig. 4.1 (c)) yields θ_W = -6.85 K and μ_{eff} = 8.09 μ_B. The negative values of θ_W are close to that of $Gd_2Ti_2O_7$ (θ_W = -11.7 K) [95]. The effective moments are consistent with μ_{eff} = 7.94 μ_B expected for Gd^{3+} ($^8S_{7/2}$).

For MgGd, χ'_{ac} shows a sharp, frequency independent peak at T_N = 1.65 K (Fig.4.4 (a)), with measurement frequencies ranging from 80 to 700 Hz, indicating a LRO transition. For ZnGd, χ'_{ac} shows an inflection point at the same temperature region (∼1.69 K). For both compounds, the transitions are further confirmed by a sharp peak in $C_{mag}(T)$ (Fig.4.4 (b)).

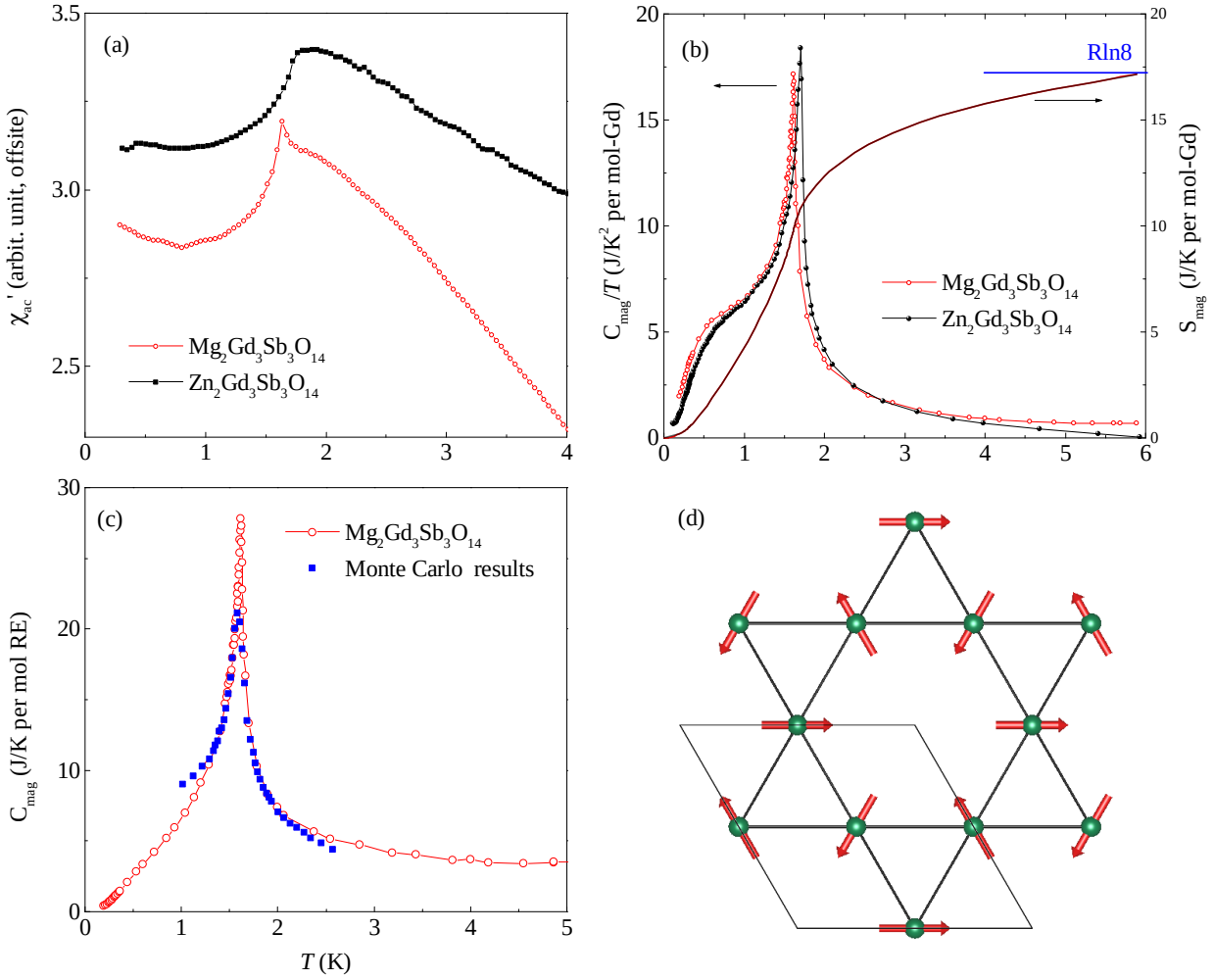

Figure 4.4: Temperature dependence of the (a) real part of χ_{ac} and (b) C_{mag}/T and S_{mag} for MgGd and ZnGd. (c) Matching between experimental data of MgGd and the scaled Monte Carlo simulation results in Ref. [8]. (d) The coplanar 120° LRO state for MgGd and ZnGd. Black solid lines represent a single unit cell.

Both of the integrated S_{mag} from 0.2 K to 6 K reach 17.2 J/K per mole-Gd, indicating a complete LRO among the Gd^{3+} spins.

The Gd^{3+} ion has Heisenberg spins ($J = 7/2$, $L = 0$) whose LRO in a 2D system violates the Mermin-Wagner theorem [96]. What is the driving force that defeats the Mermin-Wagner theorem? In order to uncover its physical origin, we have used a Luttinger-Tisza type theory [97, 98] and studied the eigenvalues and eigenfunctions of the interaction matrix in wave vector space. The calculation was done by one of my collaborators, Prof. Shastry Sriram at the University of California, Santa Cruz. The general idea is to construct a 2D kagome lattice and treat exchange and dipolar interactions as vectors in k-space (the so called Luttinger-Tisza method). Therefore, given an eigenvalue for a 2D Bravais lattice, the interactions reduce to a 9×9 matrix that can be easily diagonalized. For MgGd/ZnGd, the dipolar energy scale of the nearest neighbor spins $D_{nn} \sim 0.79$ K, while an estimate of the exchange constant is $J_{ex} \sim 5.62/5.73$ K, respectively. We found that the minimum eigenvalue of the interacting matrix is at the Brillouin zone center with $k = 0$, and the corresponding eigenvector represents a 120° state where the three spins in the unit cell lie in the plane pointing along three axes at angles $2\pi/3$ to each other (Fig. 4.4 (d)). Here, it is the large dipolar term that breaks the rotational invariance, lifts the frustration of a kagome lattice, and helps defeat the Mermin-Wagner theorem for a 2D Heisenberg lattice. It is known that higher values of spin than 1/2 release the frustration somewhat like soft spins would [99], and the case here has S = 7/2. This seems to enable a 2D-Ising like transition with a logarithmic heat capacity in the style of Onsager. Actually, a similar spin structure was predicted by Maksymenko et. al by considering classical dipoles on a kagome lattice[8]. Their calculated specific heat agrees well with our experiment in the critical region by proper scaling (Fig. 4.4 (c)). Thus, we conclude MgGd/ZnGd to be a rare example of a dipolar interaction mandated spin ordering on a kagome lattice.

4.1.4 $Mg_2Tb_3Sb_3O_{14}$ and $Zn_2Tb_3Sb_3O_{14}$

For MgTb, a CW fit from 150 K to 300 K (Fig. 4.1 (d)) of $1/\chi_{dc}$ yields a θ_W = -13.70 K and μ_{eff} = 9.98 μ_B. For ZnTb, a similar fit yields θ_W = -13.41 K and μ_{eff} = 9.86 μ_B. The

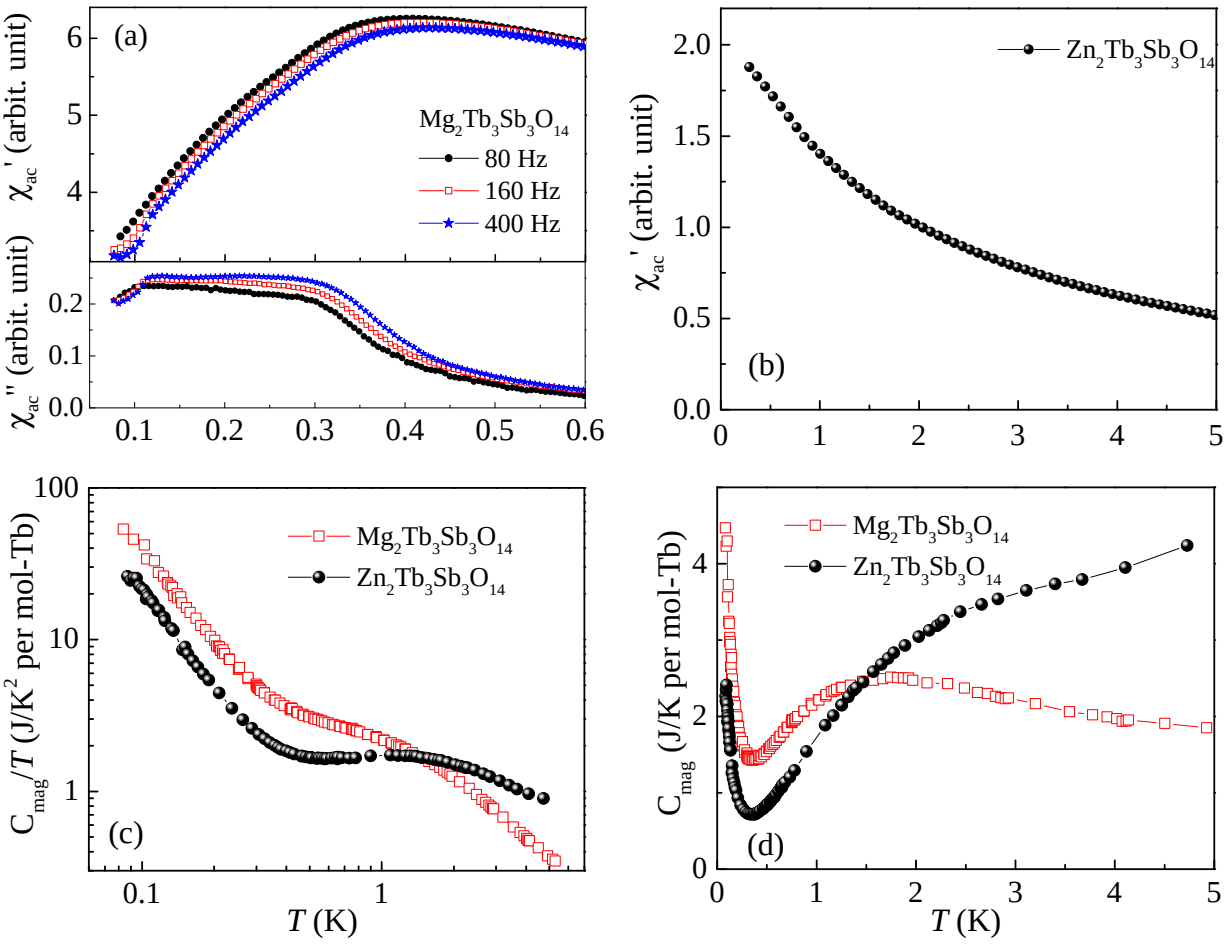

Figure 4.5: (a) Temperature dependence of the real and imaginary part of χ_{ac} with different ac field frequencies for MgTb. (b) The real part of χ_{ac} for ZnTb. (c) Low temperature C_{mag}/T plotted in a log-log scale for MgTb and ZnTb. (d) C_{mag} plotted in a linear scale.

effective moments are slightly larger than the free ion moment of μ_{eff} = 9.72 μ_B expected for Tb^{3+}.

For MgTb, both the real (χ'_{ac}) and imaginary (χ''_{ac}) part of the ac susceptibility show a broad feature around 0.35 K that is frequency dependent. Below this temperature, an anomaly is observed at 0.12 K that is more clearly seen in χ''_{ac}. Aside from these, no sharp LRO features are observed down to 50 mK (Fig. 4.4 (a)). For ZnTb, χ'_{ac} indicates a paramagnetic behavior down to the lowest measured temperature of 0.3 K, which is frequency independent (Fig. 4.4 (b)). For both compounds, the absence of LRO is further confirmed by the specific heat measurement where no singularity is observed down to 80 mK. Instead, the C_{mag} shows a broad feature (around 1.5 K for the MgTb and 2.5 K for ZnTb), followed by a power law rise below 0.3 K, as seen in the log-log plot of Fig. 9(c). We attribute this behavior to the hyperfine coupling between the nuclear and electronic spin degrees of freedom of the Tb^{3+} ion (for ^{159}Tb, nuclear spin is $I = 3/2$).

The absence of LRO in MgTb and ZnTb is reminiscent of similar behavior in the pyrochlore compound $Tb_2Ti_2O_7$. As mentioned in the introduction, $Tb_2Ti_2O_7$ remains a candidate for hosting the QSI/QSL state. In order to explain the absence of LRO, theory has invoked virtual transitions between the CEF levels of the ground state and the low lying excited state which preclude conventional order [41, 44]. Due to the similar local environment, we also expect the same Ising anisotropy as well as similar low lying CEFs in Tb-TKLs. Similar to the case of the Pr-TKLs, the difference is that every CEF doublet has split into two singlet levels, making it necessary to consider a four singlet levels to fully account for the low temperature magnetism. It is possible that a similar virtual transition is playing an important role to obstruct LRO in Tb-TKLs, making them promising QSL candidates.

4.1.5 $Mg_2Dy_3Sb_3O_{14}$ and $Zn_2Dy_3Sb_3O_{14}$

For MgDy, the CW fit below 10 K yields θ_W = -0.18 K and μ_{eff} = 10.20 μ_B (Fig. 4.1 (e)), consistent with the free ion moment of 10.63 μ_B for Dy^{3+} ($^6H_{15/2}$). For ZnDy, a similar fit (Fig. 4.1 (e)) of $1/\chi_{dc}$ yields θ_W = -0.72 K and μ_{eff} = 10.20 μ_B. In $Dy_2Ti_2O_7$ [95], the small θ_W (-0.20 K) is due to the competition between the dipolar interaction and

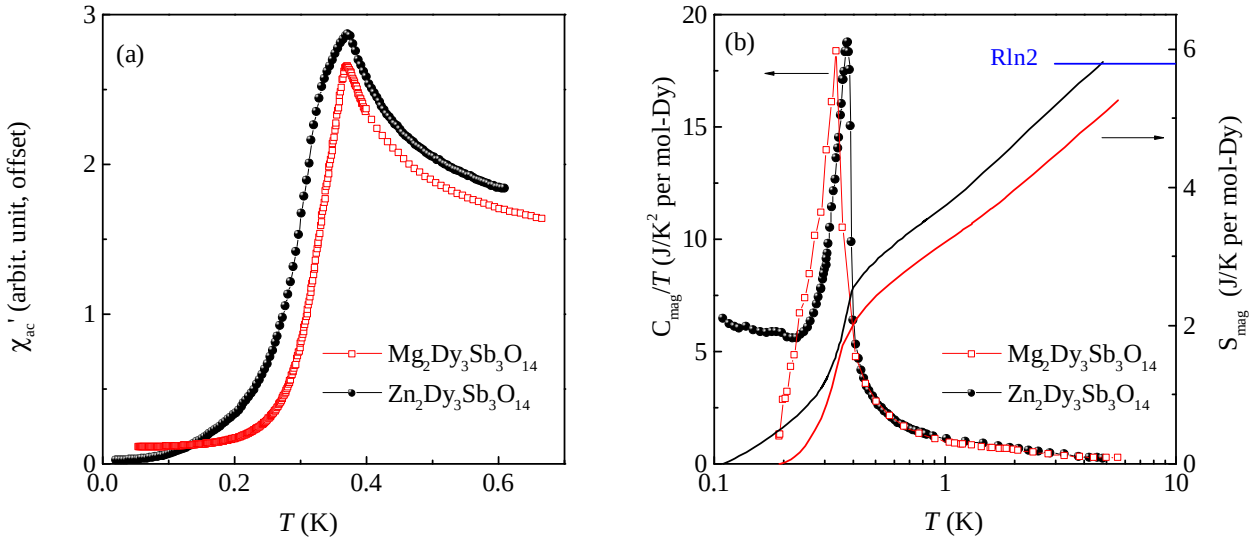

Figure 4.6: (a) Temperature dependence of the real part of χ_{ac} for MgDy and ZnDy. (b) Low temperature C_{mag}/T and S_{mag} for the two Dy-TKLs.

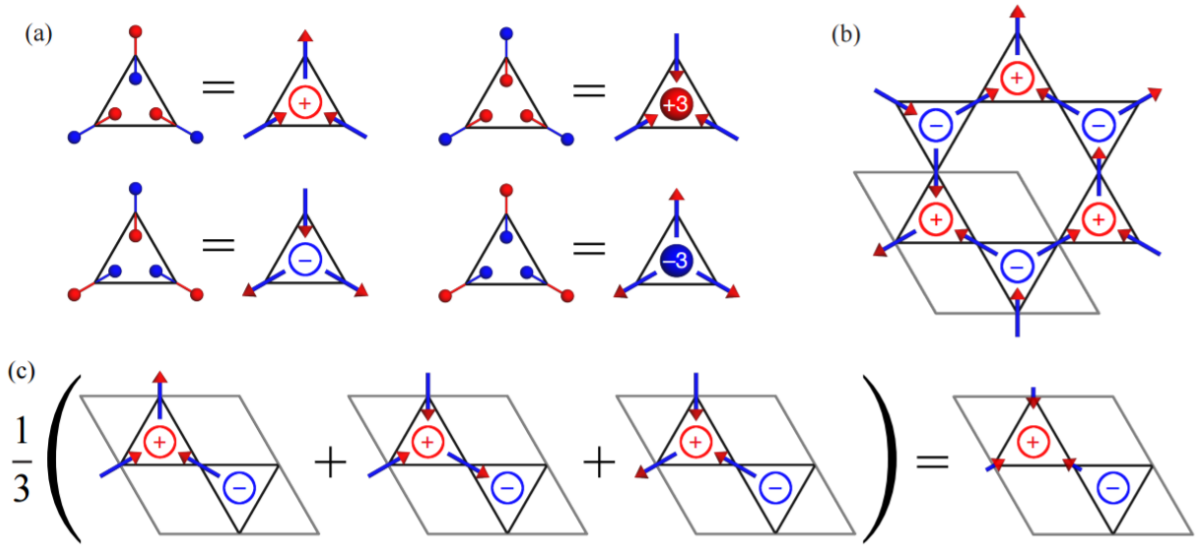

Figure 4.7: (a) Relationship between spin vectors (arrows), magnetic dipoles (connected red and blue spheres) and emergent charge of a triangle (labeled as ± 1 or ± 3). (b) Example of a microstate showing emergent charge order (ECO). (c) The vector average of the three microstates that are equally occupied in a ECO state yields an average all-in/all-out structure with an ordered moment equaling to 1/3 of the full moment. This plot is taken from Ref. [9].

super-exchange couplings of Dy ions. Here, the similarity in local structure translates into a similar-size coupling to the pyrochlore case since the total spin-spin coupling is dominated by the dipolar interaction. With the ferromagnetic dipolar interaction, the negative θ_W again shows the antiferromagnetic nature of the exchange interactions in MgDy.

For both compounds, transitions to LRO are observed both in the χ'_{ac} (Fig. 2(e)) and $C_{mag}(T)$ (Fig. 2(f)), at $T_N = 0.37$ K and 0.39 K, respectively. For MgDy, the integrated entropy from 0.2 K to 6 K reaches $S_{mag} = 5.38$ J/K per mole Dy, hosting a zero-point entropy of 0.38 J/K when compared with Rln2 = 5.76 J/K per Dy. An extra increase is observed in C_{mag}/T of ZnDy below 0.2 K that is absent in that of MgDy. Due to this increase, the integrated S_{mag} from 0.1 K to 6 K reaches 5.81 J/K per mole Dy. Aside from this, the position, intensity, and shape of the C_{mag} peak are almost identical for MgDy and ZnDy.

Initially, we interpreted the transition at 0.37 K in MgDy as a LRO of the Dy^{3+} spins because of the lack of frequency dependence of χ'_{ac} and the sharpness of the transition in both χ'_{ac}, and C_{mag} [100]. Following our findings, recent neutron scattering experiments [9] illustrate that this LRO transition is actually an ECO where emergent magnetic charge degrees of freedom exhibit LRO while spins remain partially disordered. As discussed in the introduction, the idea of magnetic charge comes from the monopole in spin ices. With Ising spins in a TKL, the potential for emergent behavior is defined by considering a spin (magnetic dipole) as two separate + and − magnetic charges so the emergent charge of a triangle is defined as the algebraic sum over the three charges it contains (Fig. 4.7 (a)) [7, 9]. In the ECO state, the + and − charges alternate, forming a LRO pattern, while the remaining threefold degeneracy of spin states is preserved for each charge; therefore the spin order is only partial (Fig. 4.7 (b)). As a result, the partially disordered spins give an averaged LRO moment on each Dy site (Fig. 4.7 (c)) which is the origin of the LRO features observed in χ'_{ac} and C_{mag}. As described in Ref. [9], there are two experimental signatures that differentiate the ECO state from conventional LRO: (i) a non-zero entropy $S_0 = 0.11R$ per mole Dy [101] and (ii) the presence of both Bragg and diffuse magnetic scattering in neutron-scattering measurements [62, 61]. The first signature is observed in our C_{mag} measurement (Fig. 4.6 (c)), and the second signature, namely the coexistence of

Bragg and diffuse magnetic scattering, has also been confirmed by Paddison et. al. in Ref. [9].

With almost identical behaviors observed here between MgDy and ZnDy, it is likely that ZnDy shares the same ECO ground state as well. In this sense, the increase of C_{mag} below 0.25 K in ZnDy is unexpected. This signal is likely not due to the Dy nuclear spin, given the same magnetic ion and the same hyperfine coupling. One possibility is that it is related to the additional spin dynamics below the ECO, which has been proposed theoretically by Monte Carlo simulations [7, 9]. With the partially ordered ECO state, a fully spin-ordered state with zero entropy density could be achieved at an even lower temperature given non-local (ring flip) spin dynamics that do not cost energy within the ECO manifold. The extra entropy recovered in ZnDy compared to that of MgDy ($\sim$ 0.4 J/K per mole-Dy) is consistent with such a picture where spin dynamics drive the system further towards LRO and fully recover the total entropy of Rln2. Yet it remains unknown why such dynamics are absent in MgDy.

4.1.6 $Mg_2Ho_3Sb_3O_{14}$ and $*Zn_2Ho_3Sb_3O_{14}$

For MgHo, a low temperature CW fit from 2 K to 10 K of $1/\chi_{dc}$ (Fig. 4.1 (f)) yields θ_W = -0.27 K and $\mu_{eff} = 10.54\ \mu_B$. For $*$ZnHo, a similar fit (Fig. 4.1 (f)) yields θ_W = -2.49 K and $\mu_{eff} = 10.22\ \mu_B$. These values for the effective moment are close to the free ion moments of $\mu_{eff} = 10.63\ \mu_B$ expected for Ho^{3+}. The origin for the small negative θ_W here is the same as those of the Dy-TKLs.

For MgHo, both the real part (χ'_{ac}) and the imaginary part (χ''_{ac}) of χ_{ac} show a broad peak around 0.4 K with strong frequency dependence (Fig. 4.8 (a)). With increasing frequency of the ac field, the peak becomes even broader and shifts higher in temperature. By fitting the ac field frequency (f) and χ''_{ac} peak maximum T_{max} to an Arrhenius formula $f = f_0 \exp(-E_b/T)$, we obtain an energy barrier of $E_b = 12.3$ K (Fig. 4.8 (a) inset). For $*$ZnHo, an even broader peak with similar frequency dependence is observed in both χ'_{ac} and χ''_{ac} around 0.45 K (Fig. 4.8 (b)). The corresponding energy barrier from the Arrhenius fit is $E_b = 7.2$ K.

Similar frequency dependence of χ_{ac} has been observed in their parent spin ice pyrochlores $Dy_2Ti_2O_7$ and $Ho_2Ti_2O_7$ above the spin freezing transition [27, 15]. In $Dy_2Ti_2O_7$, at a

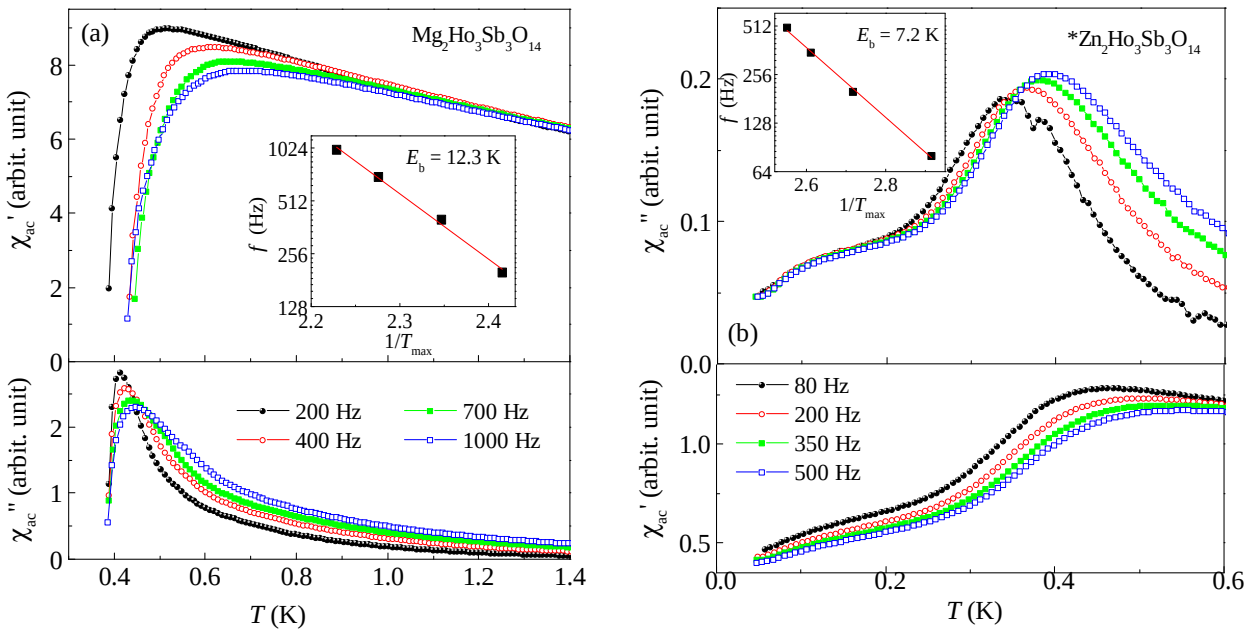

Figure 4.8: Temperature dependence of the real part (χ'_{ac}) and imaginary part (χ_{ac}") of χ_{ac} with different ac field frequencies for (a) MgHo and (b) $*$ZnHo. Insert: the ac field frequencies versus inverse peak maximum temperature of χ''_{ac}.

temperature region above the spin freezing where the monopole density is high but where the double-monopoles are few, the relaxation behavior in χ_{ac} can be well parametrized by an Arrhenius law. The related value of E_b is equal to twice the effective spin-spin coupling (J_{eff}), which is actually the energy cost of a single monopole defect [102]. In $Ho_2Ti_2O_7$, a larger value of $E_b = 13.08$ K ($\sim 6J_{eff}$) is observed, and the origin is not well understood [103].

Moving forward, what is the ground state, and what is the associated energy barrier in the Ho-TKL? First, with close similarities of the spin anisotropies and the spin-spin interactions between MgDy and MgHo, similar ECO states would be expected. Indeed, for MgHo, the temperature of the 0.4 K transition in χ_{ac} is close to the 0.37 K ECO transition in MgDy. However, the frequency dependence of χ_{ac} clearly differentiates it from that of MgDy, suggesting an ECO state with an extra spin relaxation process due to thermal or quantum fluctuations. Such behavior is likely related to the non-Kramers nature Ho^{3+} where the extra lowering of site symmetry in the TKL system splits the energy of CEF ground state doublets in Ho^{3+} at a finite energy, building an energy barrier for spin-spin interactions. The related relaxation process could also involve a hyperfine contribution that is not uncommon

in Ho magnets at these temperatures. Second, given the large dipolar couplings which act ferromagnetic exchange interactions at the nearest neighbor, MgHo is a potential candidate for hosting the KSI state. As discussed in Ref. [16], classical spins with TKL-like Ising anisotropy on a kagome lattice are highly frustrated which will result in a large ground state degeneracy and the zero-point entropy. Similar to that of the pyrochlore spin ice, if the KSI state is achieved, the broad peak observed in χ_{ac} of MgHo could represent a spin freezing process with $T_f \leq 0.4$ K while the system enters the SRO state characterized by the KSI ice rule. Then the value of $E_b = 12.3$ K is likely related to the energy difference from the ice rule state to the excited all-in-all-out state for a single Ho-triangle. The KSI state distinguishes itself from the ECO state in such a way that the magnetic charge degrees of freedom with respect to each triangle do not order, which will not give an averaged LRO of spins. Thus, from the point of view of elastic neutron scattering, only diffuse scattering is expected in the absence of sharp magnetic Bragg peaks. In order to clarify the exact ground state of MgHo, low temperature neutron diffraction measurement will be necessary.

Indeed, we have performed elastic and inelastic neutron scattering measurements to study this low temperature magnetism. The results, along with the $C(T)$ data, have established MgHo as a quantum kagome ice where the non-Kramers nature of Ho^{3+} induces quantum fluctuations, resulting in a moment-modulated ECO state. The results and analysis will be detailed in the next chapter.

For $*$ZnHo, the physics is complicated by the Zn-Ho site-disorder mentioned above. For a totally disordered TKL system, the site-disorder destroys the well-separated Ho kagome layers and forms a disordered 3D pyrochlore-like system where each site has an occupancy of 40% non-magnetic Zn ions and 60% magnetic Ho ions. Compared to the Ho-pyrochlore lattice, such system will be depleted in the A-sublattice and stuffed with extra Ho ion in the B-sublattice. In the stuffed spin ice compound $Ho_{2+\delta}Ti_{2-\delta}O_{7-\delta}$, a "cluster glass" ground state [104] is found. For $*$ZnHo, the frequency dependence in χ_{ac} is likely related to a similar glassy behavior.

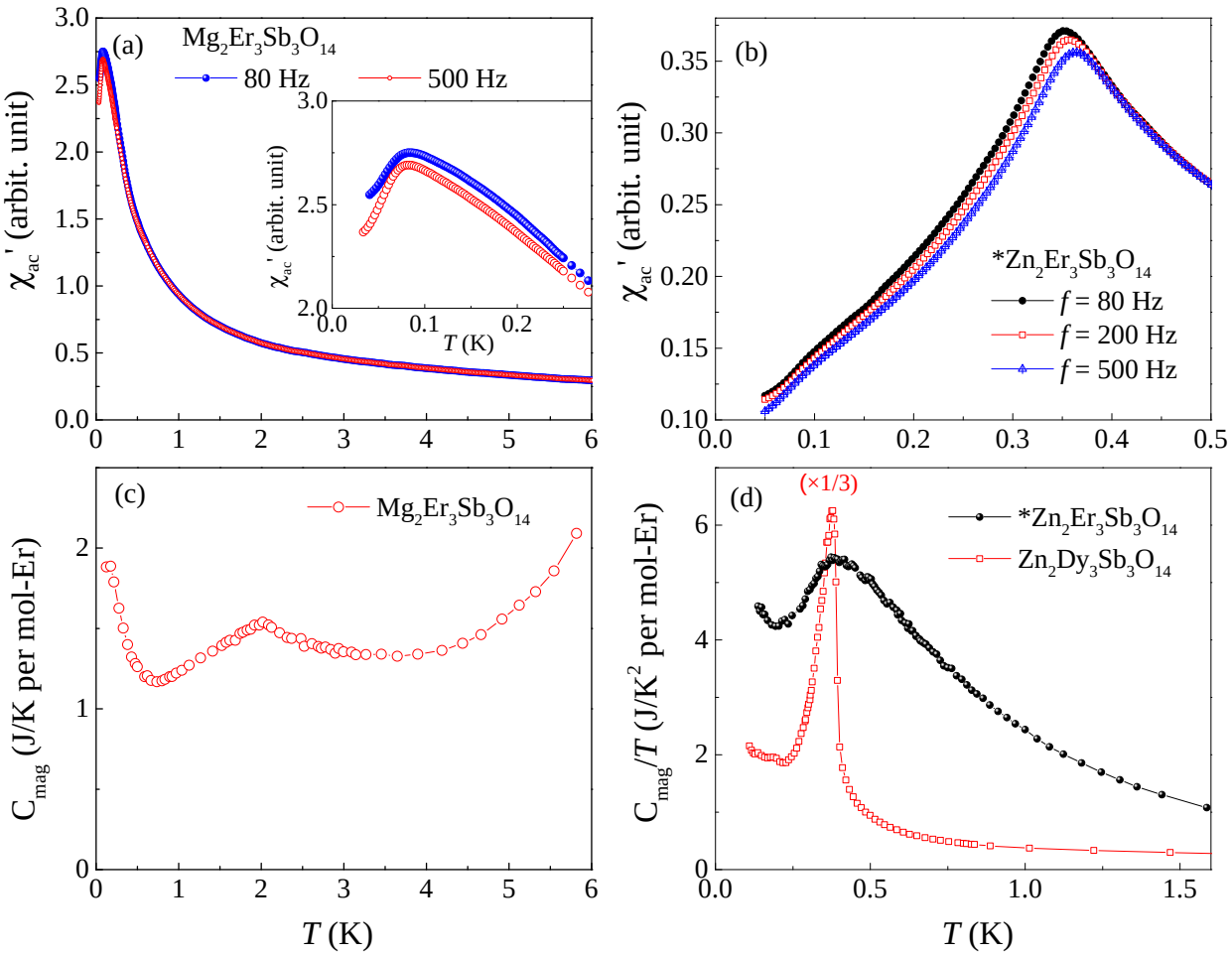

Figure 4.9: Temperature dependence of the real part of χ_{ac} with different ac field frequencies for (a) MgEr and (b) ZnEr. Inset: zoomed in χ'_{ac} at the low temperature region. (c) C_{mag} for MgEr. (d) C_{mag}/T for $*$ZnEr. The ZnDy data is plotted for reference.

4.1.7 $Mg_2Er_3Sb_3O_{14}$ and $*Zn_2Er_3Sb_3O_{14}$

For MgEr, a high temperature CW fit from 100 K to 300 K yields θ_W = -14.52 K and μ_{eff} = 9.45 μ_B (Fig. 4.1 (g)). For *ZnEr, a similar fit yields θ_W = -16.08 K and μ_{eff} = 9.67 μ_B. The effective moments are consistent with the free ion moment of $\mu = 9.58\ \mu_B$ for Er^{3+} ($^4I_{15/2}$), and the value for θ_W is close to that of the pyrochlore $Er_2Ti_2O_7$ (θ_W = -15.93 K) [95].

For MgEr, χ_{ac} was measured down to 30 mK with a broad peak observed around 80 mK (Fig. 4.9 (a)) which shows weak frequency dependence. This peak is not a LRO transition according to our recent neutron scattering experiment which shows intense diffuse scattering persisting down to $T \sim 60$ mK. The data will be published elsewhere and will not be further discussed here. The $C_{mag}(T)$ was measured down to 120 mK and exhibits a weak and broad peak around 2 K (Fig. 4.9 (b)). At this temperature, no anomaly is observed in χ_{ac}, while an extremely weak anomaly (2*10^{-8} emu/mole-Er) was seen in χ_{dc} at 2.1 K that is perhaps related to the weak $C_{mag}(T)$ peak. However, the nature of the 2.1 K transition remains a mystery. The small size of the 2.1 K feature suggests an origin in a phase that is not "topologically" connected to a classical ordered phase. Given that Er is XY-like in the pyrochlores, we speculate that, if also XY-like in the TKL, this phase is a Kosterlitz-Thouless vortex unbinding transition [105].

In *ZnEr, a SRO feature at 0.35 K is observed in both χ'_{ac} and $C_{mag}(T)$. As shown in Fig. 4.9 (b), the χ'_{ac} peak is broad with an obvious frequency dependence. The peak in C_{mag} is also broad compared with the sharp LRO transition in ZnDy. The frequency dependence of χ'_{ac} and the broadness of the transition from χ'_{ac} and C_{mag} are characteristic behaviors of a SG system [106]. Similar to *ZnHo, site disorder exists in *ZnEr. The present situation is akin to $(Eu_xSr_{1-x})S$ [107] and other insulating SG systems where the concentration of magnetic ions is close to the percolation threshold for nearest neighbor interactions. Therefore, *ZnEr most likely exhibits a SG transition with $T_{SG} = 0.35$ K.

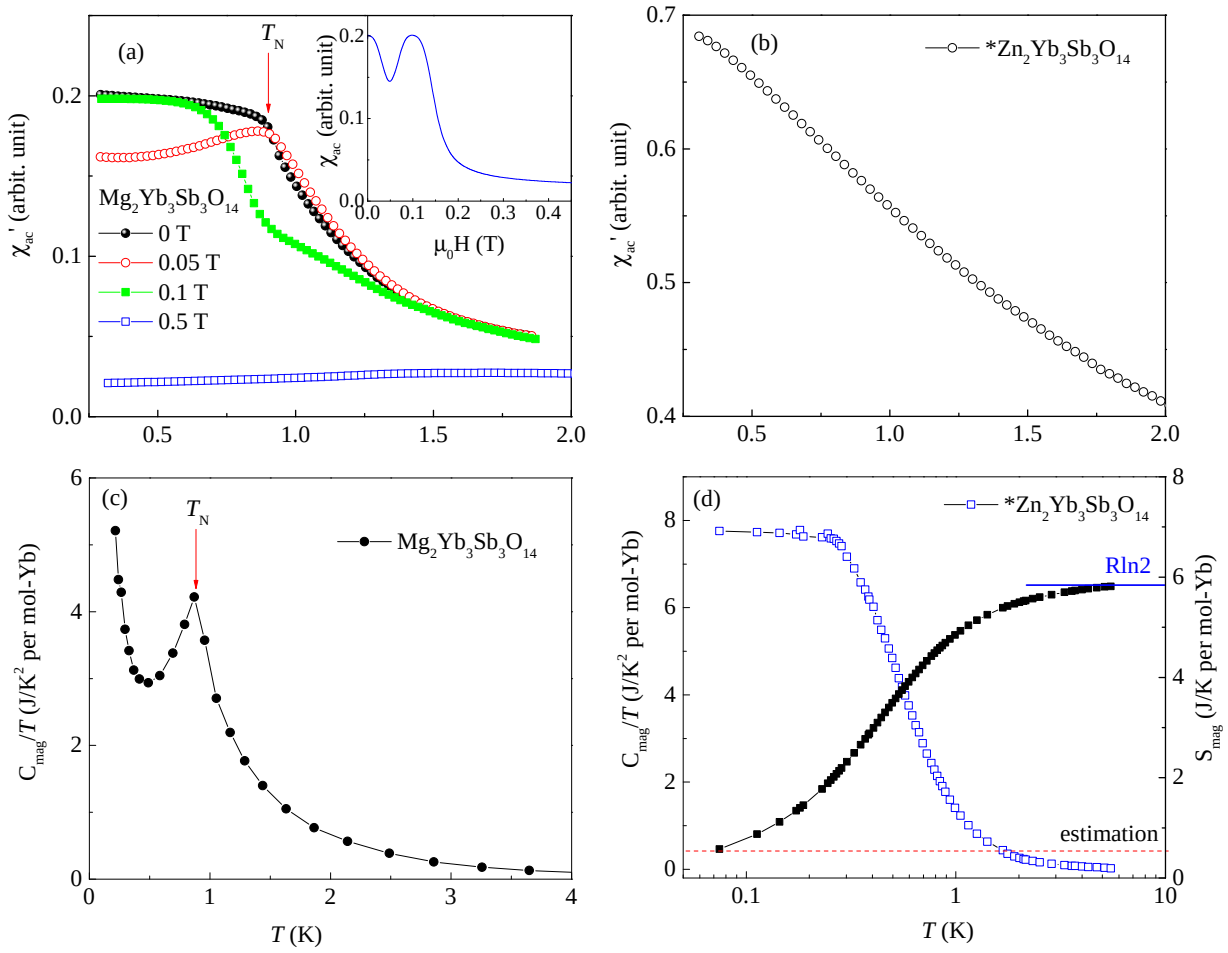

Figure 4.10: (a) Temperature dependence of the real part of χ_{ac} under different dc fields for MgYb. Inset: real part of χ_{ac} as a function of applied dc field. (b) The real part of the χ_{ac} for ∗ZnYb. (c) C_{mag}/T for MgYb. (d) C_{mag}/T and S_{mag} for ∗ZnYb. The dashed red line presents the estimated entropy below 76 mK assuming T-linear behavior of C_{mag} down to zero temperature.

4.1.8 $Mg_2Yb_3Sb_3O_{14}$ and $*Zn_2Yb_3Sb_3O_{14}$

For MgYb, a low temperature CW fit from 2 K to 10 K of $1/\chi_{dc}$ (Fig. 4.1 (h)) yields θ_W = -0.45 K and $\mu_{eff} = 3.24\ \mu_B$. For *ZnYb, a similar fit yields θ_W = -0.39 K and $\mu_{eff} = 3.18\ \mu_B$. These values for μ_{eff} are smaller than the free ion moments of $\mu_{eff} = 4.54\ \mu_B$ expected for Yb^{3+}, but similar to those found in the Yb pyrochlores, indicating a planar spin anisotropy at low temperature. Unlike the small positive θ_W found in Yb pyrochlores, the values for θ_W for both Yb TKLs are negative. This implies an enhanced antiferromagnetic exchange interaction while transforming from the 3D pyrochlore lattice to the 2D TKL.

For MgYb, χ'_{ac} shows an inflection point at 0.88 K at zero field (Fig. 4.10 (a)) which is frequency independent (not shown here). The transition temperature is consistent with a λ-shaped peak in C_{mag}/T (Fig. 4.10 (c)), suggesting an antiferromagnetic LRO transition with $T_N = 0.88$ K. The feature in χ'_{ac} becomes a well-defined peak under a small dc magnetic field of 0.05 T (red curves in Fig. 4.10 (a)). With even larger dc field, this peak moves to lower temperature and becomes weaker in intensity. The dc field scan of χ'_{ac} measured at 50 mK is shown in the inset of Fig. 4.10 (a). Two features are evident from the data: a drop between 0 and 0.05 T and a broad peak around 0.1 T, which drops quickly with even higher fields. Similar behaviors have been observed in a parent pyrochlore antiferromagnet $Yb_2Ge_2O_7$ [72, 108]. There, the Yb-sublattice possesses an antiferromagnetic LRO ground state with $T_N = 0.62$ K. With an applied magnetic field, a double peak feature is observed in the field scan of χ'_{ac}, where the first peak around 0.1 T is due to magnetic domain alignment and the second peak at 0.2 T corresponds to a spin-flop transition from the antiferromagnetic LRO state to the spin polarized state [108]. Similar physics is likely to occur in MgYb such that the two features in χ'_{ac} are due to magnetic domain movement and spin polarization, respectively.

For *ZnYb, paramagnetic behavior is observed in χ'_{ac} down to the lowest measured temperature of 0.3 K, and no LRO is observed in C_{mag} down to 75 mK. Instead, C_{mag}/T becomes a constant below 0.25 K (Fig. 4.10 (d)), indicating a T-linear behavior for C_{mag}. If such T-linear behavior is extended to zero temperature, the integrated entropy from 0 K to 6 K reaches 5.80 J/K per mole-Yb (Fig. 4.10 (d) inset) which is close to the value

of Rln2 = 5.76 J/K expected for an ordered two-level system. Due to strong site-disorder, some SRO glassy behavior is expected as that of ∗ZnEr. Since no SRO feature is observed in χ'_{ac} nor C_{mag}, it is possible that the spin freezing process lies below 0.3 K in the $C_{mag} \propto T$ region, which is not detected by χ'_{ac}. On the other hand, if such a possibility is ruled out by further measurements, the absence of spin freezing and the fully recovered entropy clearly differentiate ∗ZnYb from a conventional SG system, indicating a single (or very limited number of) micro-state in configuration space at zero temperature. Given the small effective spin-1/2 moments of Yb^{3+}, theoretical interpretation of such a state will be interesting even for a system even with severe disorder.

4.2 Discussion

4.2.1 Spin Anisotropies

As discussed in the previous chapter, if we assume a single ion anisotropy of each RE^{3+} ion similar to that of their parent pyrochlore lattices, three types of anisotropies are expected. For Pr^{3+}, Nd^{3+}, Tb^{3+}, Dy^{3+}, Ho^{3+}, Ising anisotropy is expected, while Er^{3+} and Yb^{3+} should exhibit XY behavior and Gd^{3+} should exhibit Heisenberg-like behavior. In TKL systems, when mediated by exchange/dipolar interactions, these three types of spins introduce different magnetic ground states. The magnetic properties of the 16 $A_2RE_3Sb_3O_{14}$ compounds (A = Mg, Zn; RE = Pr, Nd, Gd, Tb, Dy, Ho, Er, Yb) have been summarized in Table 4.1. Here, aside from the non-magnetic ground state found for Pr-TKLs, we will focus on the Mg branch and discuss their ground states in terms of each type of spin anisotropy.

Among the four $Mg_2RE_3Sb_3O_{14}$ (RE = Nd, Tb, Dy, Ho) compounds with possible Ising anisotropy, MgNd has smaller effective moments where the dipole-dipole interaction is small. The observed all-in-all-out spin structure agrees with the LRO scenario expected for an antiferromagnetic Ising model [86]. The other three Ising spin compounds, $Mg_2RE_3Sb_3O_{14}$ (RE = Tb, Dy, Ho), possess a large moment $\sim$ 10 μ_B. Within this group, the Dy and Ho compounds are most similar due to a small antiferromagnetic exchange interaction as estimated from the low temperature θ_W ($\sim$ -0.2 K). Since the dipole-dipole interaction has

an energy scale ~ 1.3 K, it is tempting to view both systems as pure dipolar ferromagnets. It is possible both compounds possess an ECO ground state, yet apparent differences in χ_{ac} are observed, suggesting different spin dynamics. This situation of two distinct ground states for the Dy and Ho compounds in TKLs is different from that of pyrochlores where typical spin ice behavior is observed in all $Ho_2X_2O_7$ and $Dy_2X_2O_7$ (X =Ti, Sn, Ge) [26, 15, 103, 109, 110, 111]. This interesting contrast suggests the importance of studying the underlying spin dynamics in order to understand precisely how lowering the dimensionality in the TKLs leads to LRO.

In the TKL family, MgGd is the only Heisenberg system due to the half filled f-shell of Gd^{3+}. The LRO transition at 1.65 K is due to strong dipole-dipole interactions, which provides an experimental example of the suppression of frustration in a kagome lattice by strong long-range interactions.

The Er^{3+} and Yb^{3+} are both effective spin-1/2 Kramers ions that likely possess XY anisotropy as in their pyrochlore counterparts. As Yb^{3+} possesses a much smaller moment than Er^{3+}, one would expect larger quantum fluctuations which usually perturb LRO. In the TKLs, however, LRO is found in MgYb instead of MgEr. If the XY anisotropy is preserved in both MgEr and MgYb, our observations imply that the anisotropic exchange that couples to the CEF g-tenser plays an important role. As shown in the introduction, for the XY pyrochlore compounds, the detailed balance between anisotropic nearest neighbor exchange interaction, $J_{ex} = (J_{zz}, J_{\pm}, J_{z\pm}, J_{\pm\pm})$, in addition to the strong quantum spin fluctuations of the effective spin-1/2 moment, stabilizes various exotic magnetic ground states [5]. In $Er_2Ti_2O_7$, for example, dominant interactions are coplanar type $J_{\pm}$ and $J_{\pm\pm}$ that couples the spin component within the XY plane [32]. Accordingly, the magnetic ground state is an antiferromagnetic state with XY-type LRO that is stabilized by quantum fluctuations [32, 112]. Meanwhile, $Yb_2Ti_2O_7$ has a major Ising type contribution (J_{zz}) that couples the Ising component of Yb^{3+} moments. Thus, moments in $Yb_2Ti_2O_7$ tend to behave as Ising spins, which results in a quantum spin ice ground state [31]. An analogous stabilization is likely to occur in the XY TKLs, which could lead to a complex ground state phase diagram and differences between MgEr and MgYb.

Table 4.1: A summary of magnetic properties of $A_2RE_3Sb_3O_{14}$ (A = Mg, Zn; RE = Pr, Nd, Gd, Tb, Dy, Ho, Er, Yb). For RE = Nd, Gd, Dy, Ho, Yb compounds, values of θ_W and μ_{eff} are from low temperature fits of $1/\chi_{dc}$. For RE = Pr, Tb, Er, values from high temperature fits are used instead because of the nonlinear $1/\chi_{dc}$ at low temperature due to CEF effects. Therefore, these values from high temperature fits do not necessarily reflect the spin-spin interactions at low temperatures.

		Pr	Nd	Gd	Tb	Dy	Ho	Er	Yb
	f state (RE^{3+})	$4f^2$	$4f^3$	$4f^7$	$4f^8$	$4f^9$	$4f^{10}$	$4f^{11}$	$4f^{13}$
	Kramers ion?	No	Yes	Yes	No	Yes	No	Yes	Yes
	Anisotropy	$\sim$	Ising	Heis.	Ising	Ising	Ising	XY	XY
A = Mg	θ_W (K)	-46.18	-0.05	-6.70	-13.70	-0.18	-0.27	-14.52	-0.45
	μ_{eff} (μ_B)	3.4	2.49	8.06	9.88	10.2	10.54	9.45	3.24
	Ground state	non-mag.	LRO	LRO	QSL(?)	ECO	QSI	QSL(?)	LRO
	$T_{N,f,SG}$ (K)	$\sim$	0.55	1.65	$\sim$	0.37	0.4	0.08, 2.1	0.88
A = Zn	θ_W (K)	-68.43	-0.11	-6.85	-13.41	-0.72	-2.49	-16.08	-0.39
	μ_{eff} (μ_B)	3.61	2.28	8.09	9.86	10.2	10.22	9.67	3.18
	Ground state	non-mag.	LRO	LRO	QSL(?)	ECO	SG(?)	SG	SG(?)
	$T_{N,f,SG}$ (K)	$\sim$	0.47	1.69	$\sim$	0.39	0.45	0.35	$\sim$(?)

4.2.2 Kramers Versus Non-Kramers

We can use another key attribute of these compounds to categorize the eight TKLs in the Mg branch. Five of them (RE = Nd, Gd, Dy, Er, Yb) have Kramers ions, whose single ion ground state doublet is restrictively protected by time-reversal symmetry and are thus degenerate in energy for a mean field of zero. The other three (RE = Pr, Tb, Ho) have non-Kramers ions, whose single ion ground state could also be a doublet but is not necessarily degenerate.

In the pyrochlore system, an "accidental" degeneracy of the non-Kramers doublets is usually found due to the protection of a high symmetry point group (D_{3d}) at the RE site. Recently, it has been theoretically proposed that in some spin ice like pyrochlore with non-Kramers ions, perturbations such as site-disorder, which act as local transverse fields, could lift such a degeneracy and possibly lead to different QSL ground states through quantum superpositions of spins [47]. An example is the QSL candidate $Pr_2Zr_2O_7$ [29] in which a recent inelastic neutron scattering study revealed the lifting of such degeneracy due to a continuous distribution of quenched transverse fields [46].

In the previous chapter, we have shown that in a TKL, the point group symmetry at the rare earth site is reduced from D_{3d} to C_{2h}. In such a case, the accidental degeneracy of the non-Kramers doublet is naturally removed which splits the doublet into two non-magnetic singlets state with a finite energy difference [89]. However, spin-spin interactions which act as local exchange fields can easily mix the two nearby singlets state and recover the magnetic moment. Starting from the CEF scheme of the parent pyrochlore lattice, if the energy splitting of the two lowest singlet states is comparable to the spin-spin interactions, the additional symmetry reduction can be viewed as a perturbation to the original CEF Hamiltonian where the system remains magnetic with a valid effective spin-1/2 description. One the other hand, if the two lowest singlet states get too separated in energy, exchange/dipolar interactions will be insufficient to induce magnetism magnetism, and a non-magnetic ground state is expected [113].

Among the three non-Kramers ion compounds, it is clear that MgPr belongs to the second category where a non-magnetic singlet ground state is found. The other two, MgTb and MgHo, likely belong to the first category, where the ground state doublets have a finite splitting in energy but remain magnetic. A proper description of the two systems will be Ising spins under transverse fields on a kagome lattice antiferromagnet. These two compounds can thus be thought of as 2D analogues of $Pr_2Zr_2O_7$. Our classification of the ground states based on Kramers versus non-Kramers ions seems successful: the four TKLs with Kramers ions (except for MgEr) exhibit LRO while no LRO is observed for the two TLKs with non-Kramers ions. This result implies that a comprehensive approach considering non-Kramers ions might be needed to explain the absence of LRO in MgTb and MgHo. In the next chapter, we will focus on MgHo and use neutron scattering to probe it ground state and excitations, and it indeed shows that the transverse field acts as a quantum tunneling term and turns the system into a quantum kagome ice.

4.2.3 Chemical Pressure Effects

By substituting the smaller Mg^{2+} ions with the larger Zn^{2+} ions on the non-magnetic A-site in the TKLs, we introduce chemical pressure that enlarges both lattice parameters a and c. Principally, this effect has more dramatic influences on the exchange couplings than

the dipolar interactions. In the pyrochlores, this chemical pressure effect has been proven effective for determining the magnetic ground states. For example, by replacing the Ti site with a smaller Ge ion or a larger Sn ion, the chemical pressure effect selects different magnetic ground states in the pyrochlore systems $Yb_2X_2O_7$ and $Er_2X_2O_7$ (X = Ge, Ti, Sn) [72, 108].

In the TKL system, an obvious result of chemical pressure is the structural change. As discussed above, while the A/RE site disorder is low in the Mg-branch and Zn-branch with RE ions of larger size, a severe Zn/RE site disorder is present for TKLs with smaller RE ions (RE = Ho, Er, Yb). This type of site disorder destroys the kagome lattice and introduces a random distribution of RE ions with 3D correlation, which will result in a different magnetic ground state.

For TKLs where the site disorder is small (RE = Pr, Nd, Gd, Tb, Dy), the chemical pressure seems to have little effect on the low temperature magnetism in both branches. Both MgPr and ZnPr have singlet ground states. We found LRO in the Nd, Gd and Dy compounds in both Mg and Zn branches with similar ordering temperatures (Tab. 4.1), consistent with the small lattice constant differences. No LRO is observed in both MgTb and ZnTb. It is noteworthy that some subtle differences have been observed. For example, while MgTb shows a broad SRO-like feature in χ'_{ac} at 400 mK, no such feature is seen in ZnTb. In Fig. 4.5 (c), C_{mag}/T also shows some differences above 400 mK between the two. Another example is that for MgNd, the zero field χ'_{ac} seems indicate a two-step transition, while for ZnNd, a small magnetic dc field is required to separate them. Also, for ZnDy, an extra increase of C_{mag} is observed below the ECO transition which is absent in that of MgDy. More work is needed to understand the differences between these systems.

Chapter 5

$Mg_2Ho_3Sb_3O_{14}$: A Quantum Kagome Ice from A Transverse Ising Model

Some theoretical calculations in this chapter are done in collaboration with Martin Mourigal's group at the Georgia Institute of Technology. Specifically, Joseph M. Paddison fitted the inelastic spectrum with a relaxation model, and XiaoJian Bai evaluated the mean-field Hamiltonian and found the ground state of the system. The main results of this chapter are to be published in a scientific journal.

In this chapter, I will show that MgHo, an Ising TKL antiferromagnet, is a model for a quantum kagome ice where the splitting of the Ho^{3+} crystal electric field doublet serves as a uniform transverse field, allowing quantum tunnelings between degenerate ice-like microstates. Using neutron scattering, our measurements reveal a symmetry breaking transition at 0.32 K to a partially ordered state closely related to the ECO state expected for a dipolar Ising magnet [114]. We observe persisting spin dynamics both above and below the transition, in contrast to static correlations observed in a sister compound based on Dy^{3+} [9]. Using extracted parameters from neutron data, we explain our observations within a mean-field model incorporating the effects of quantum dynamics and frustration.

5.1 Introduction

Frustrated magnetism, which arises from competing interactions in a topologically constrained lattice, can lead to a large ground state degeneracy and the formation of low-temperature, fluid-like states, so-called spin liquids [13]. Pyrochlore and kagome spin ices [15, 16] are two paradigmatic examples of spin liquids in a classical limit in a sense as the fluctuations e.g. monopole excitations) in the system are purely driven by thermal activation and that the energy barrier between degenerate microstates precludes spin dynamics when the temperature is sufficiently low. In the presence of quantum fluctuation, one can in principle obtain an exotic QSI descended from the classical spin ice state that is long-range entangled and persisting fluctuation in the zero-temperature limit [115]. One way to introduce quantum effects is to deviate from the pure Ising model and consider a local XXZ model with a transverse coupling ($J_{\perp}$), where theory predict a Coulombic U(1) quantum spin liquid phase with gapless photon-like excitations [38]. Much attention has been paid to a pyrochlore compound $Yb_2Ti_2O_7$ which is thought to be a promising realization of such a model [31]. Yet the precondition of strong Ising coupling is challenged by a recent neutron scattering measurement [50].

Another way to enhance quantum fluctuations for an Ising magnet is to apply a transverse field. The resulting transverse Ising model (TIM) is the *simplest* quantum many-body system such that the cooperative exchange interaction is separable from a tunable quantum tunneling term (transverse field). Leaving alone the frustration, the TIM is known to be a canonical example to show zero-temperature quantum phase transitions [116] and has a wide relevance to condensed matter phenomena, such as superconductivity, order by disorder, and quantum information [117]. It can be achieved experimentally in either ferromagnet with uniaxial symmetry under external magnetic fields, i.e. $CoNb_2O_6$ [118], or in rare earth compounds with a two-singlet CEF ground state [113], i.e. $LiTbF_4$ [119]. The key question is then how to introduce TIM in a real frustrated magnet since a spin ice is nonuniaxial and has a doublet CEF ground state. One theory has been proposed recently that for certain types of spin ice compounds with non-Kramers ions, such as $Ho_2Ti_2O_7$ and $Pr_2Zr_2O_7$ [46], disorder will act as quenched random transverse fields, inducing quantum entanglements that

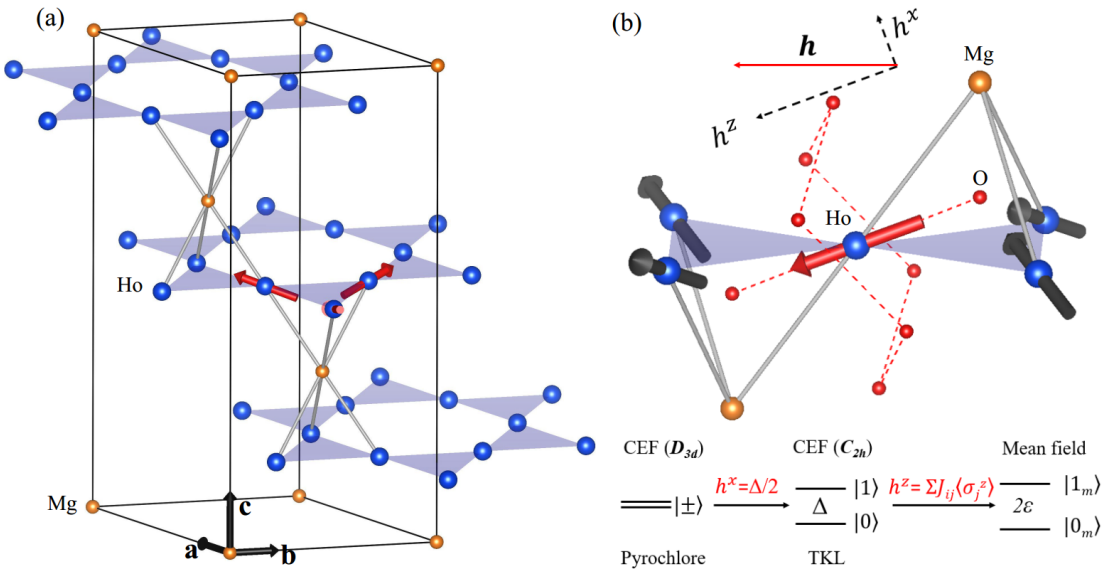

Figure 5.1: Partial crystal structure, showing the alternating Ho-kagome layers (large blue spheres) and Mg-triangular layers (small orange spheres) in a unit cell. (b) Local environment, showing eight surrounding oxygens (small red spheres) and four nearest neighbor Ho sites (whose spins are labeled by black arrows) around a central Ho ion. The mean-field at each site contains a transverse (h^x) and a longitudinal (h^z) component. The h^x effectively splits the non-Kramers doublet in the pyrochlore ($|\pm\rangle$) into two singlets in the Ho-TKL ($|0\rangle$ and $|1\rangle$) while the h^z describes the spin-spin interactions.

turn classical spin ices into quantum spin liquids [47]. Instead of considering disorder and random transverse fields that are often complicated and difficult to quantify, it is desirable to search for a structurally perfect frustrated Ising magnet with a two-singlet ground state. Such a magnet will automatically match up to a TIM under a uniform transverse field, enabling the realization of a QSI.

5.2 Transverse Ising Model

Our recently discovered TKL Ising antiferromagnet, MgHo, offers us an opportunity to realize such a QSI in a kagome lattice from the TIM. Similar to the TKL compounds described earlier, MgHo features well-isolated Ho^{3+}-kagome planes that alternate with non-magnetic Mg^{2+} triangular layers 5.1 (a). Rietveld refinements from X-ray and neutron powder diffraction measurements confirm this structure with negligible Mg/Ho site disorder, in contrast to some TKL compound studied earlier [9]. The local oxygen environment around

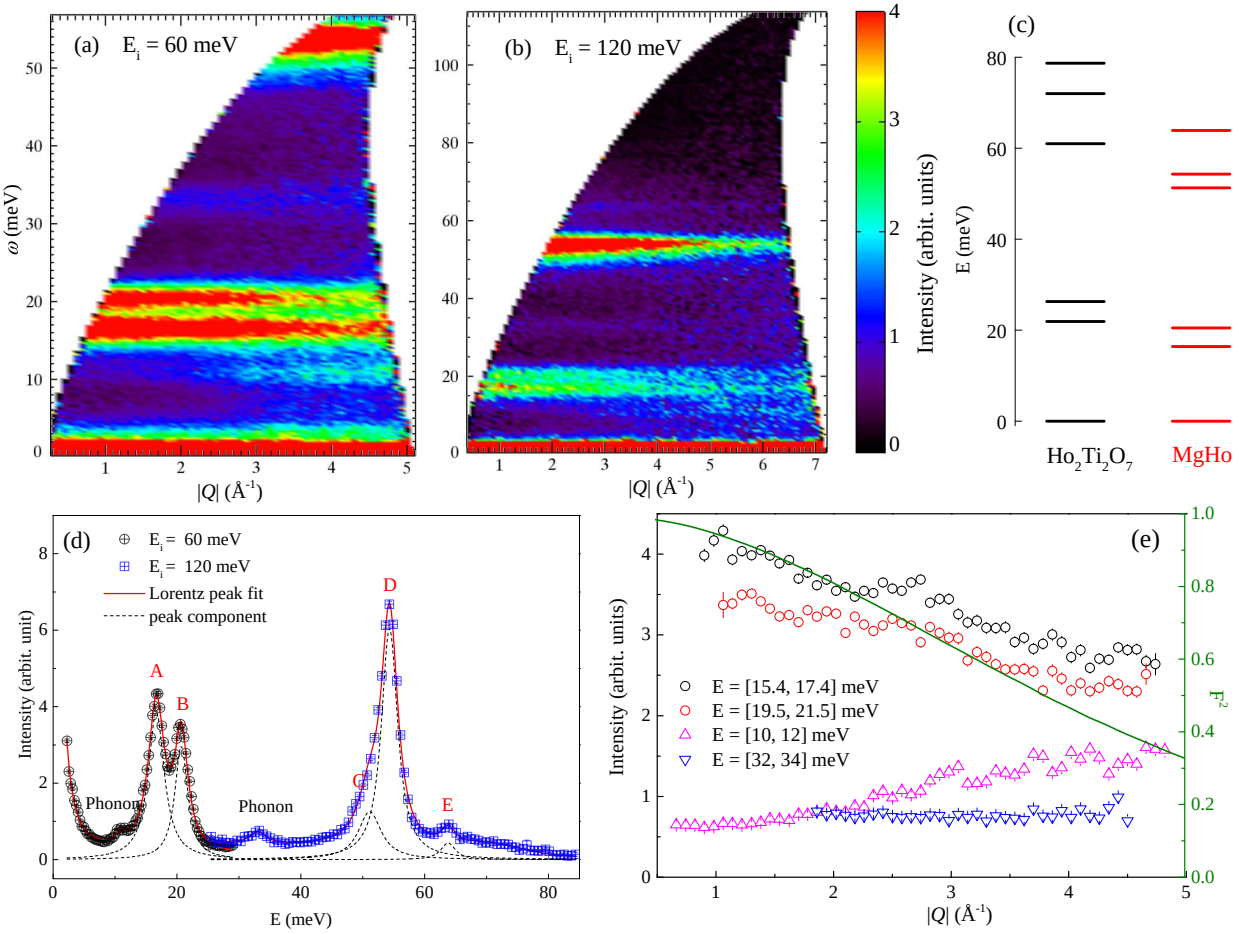

Figure 5.2: Crystal field measurements on SEQUOIA at ORNL with incident energy of (a) 60 meV and (b) 120 meV. (c) Comparison between the observed CEF levels of MgHo and that in $Ho_2Ti_2O_7$ from Ref. [10]. (d) Q cut of the inelastic spectrum. Open dots/squares are measured intensities. The peak components of five CEF levels obtained from Lorentzian peak fits are shown as black dashed lines. (e) Q dependence of different energy cuts. The magnetic form factor for Ho^{3+} is plotted for references.

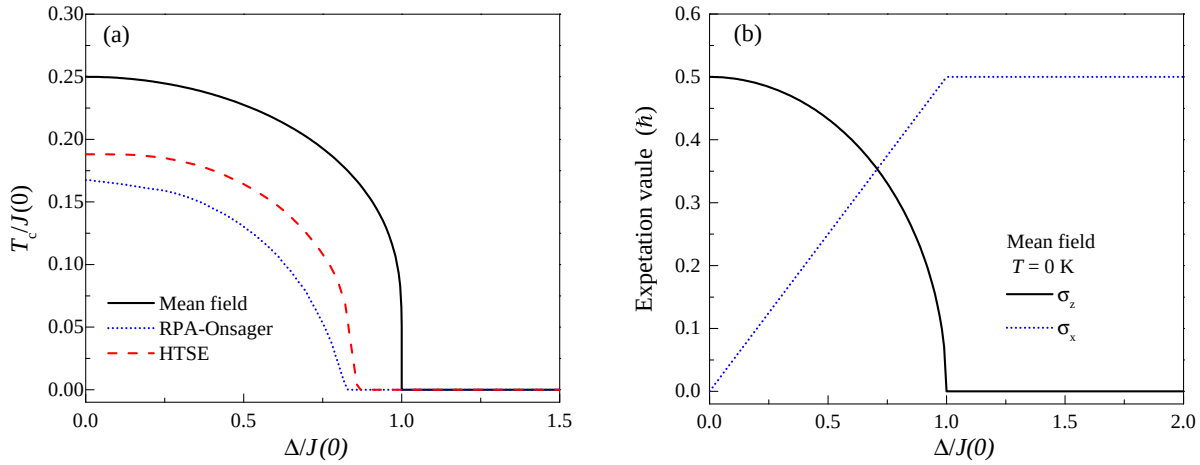

Figure 5.3: (a) The phase diagram of a non-frustrated TIM from three different models, mean-field, Random Phase Approximation (RPA) with Onsager correction [11] and high temperature series expansion (HTSE) [12]. (b) The expectation value of σ_x and σ_z as a function of $\Delta/J(0)$ from the mean-field model.

Ho^{3+} remains closely similar to that of the parent compound $Ho_2Ti_2O_7$, guaranteeing a similar CEF scheme with three distinct tripod-like Ising axes that are canted away from the kagome plane (Fig. 5.1b). At the same time, compared to $Ho_2Ti_2O_7$, the additional point group symmetry reduction at the Ho^{3+} site, in principle, splits every CEF doublet of non-Kramers Ho^{3+} ions into two non-magnetic singlets. Then what are the combination of effects on the single ion properties? In order to answer this question, we have performed a high energy inelastic neutron scattering experiment to probe the CEF excitations. A contour plot of scattering intensity as a function of energy (E) and momentum transfer (Q) is plotted in Fig. 5.2 (a), (b). By performing a Q cut of the spectrum, five CEF levels are observed at 16.4(2) 20.5(2), 51.3(8), 54.3(4), and 63.3(8) meV, respectively (5.2 (d)). Note that the excitations at $\sim$ 11 meV and $\sim$ 33 meV do not follow the magnetic form factor of Ho^{3+} (5.2(e)), therefore, are not magnetic in origin. As can be seen in Fig. 5.2 (c), the CEF scheme and intensity ratios of MgHo closely resemble those observed in $Ho_2Ti_2O_7$ [10], except for a renormalization in energy. It means that the symmetry reduction of the system only modifies the general CEF levels slightly, and the energy splitting of every Kramers doublet are within the energy resolution of our measurement. Indeed, by performing a point charge calculation from a refinement-determined structural model, the energy splitting of the ground

state doublet (Δ) is estimated to be 2.5 K, a number that is two order of magnitude smaller than the characteristic energy between different CEF levels observed here experimentally.

With well-separated higher CEF levels, the splitting Δ defines a two-singlet TIM and differentiates MgHo from other classical Ising magnets, e.g. a closely related TKL compound MgDy based on Kramer ions Dy^{3+} ions [9]. Since the two ground state singlets of Ho^{3+} (total angular momentum $J = 8$) is almost fully $j_z = \pm 8$ characteristic, we can write them as symmetric and antisymmetric forms such that $|0\rangle \approx \frac{1}{\sqrt{2}}(|8\rangle + |-8\rangle)$ and $|1\rangle \approx \frac{1}{\sqrt{2}}(|8\rangle - |-8\rangle)$. Hence, $|0\rangle$ and $|1\rangle$ define a two level CEF-basis such that the only non-zero matrix element is $\langle 0| J_z |1\rangle \equiv 8$. The Hamiltonian in the CEF-basis can be rewritten as an effective spin-1/2 model where Δ can be treated as a uniform transverse field, such that

$$H = \frac{\Delta}{2} \sum_i \sigma_i^x - \frac{1}{2} \sum_{i,j} J_{ij} \sigma_i^z \sigma_j^z. \tag{5.1}$$

Here, σ_i denotes unit Pauli matrices and $J_{i,j}$ is the effective interaction between Ising pseudo-spins that contains two parts, the nearest neighbor exchange coupling (J_{nn}) and a long-range dipolar interaction (D). Within a mean-field treatment (molecule field approximation), one can reduce the many-body Hamiltonian to a collection of effective single spins [120],

$$H = \sum_i \left(\frac{\Delta}{2} \sigma_i^x - \sum_j J_{ij} \langle \sigma_j^z \rangle \sigma_i^z \right). \tag{5.2}$$

where the mean-field contains both a transverse and a longitudinal component (**h** in Fig. 5.1 (b)). The eigenfunctions for effective spins ($|0_m\rangle$, $|1_m\rangle$) are superpositions of the CEF basis, whereas the ground state of the system is a product state where every spin is compatible with its molecule field. Due to J_{ij}, the mean-field at an individual site i is directly related to that of nearby sites, and the equilibrium condition leads to $\langle 1_i^m | \sigma^z | 0_i^m \rangle = 0$.

For a non-frustrated TIM (e.g. $J_{ij} > 0$), the interactions are site-independent so that a constant $\mathbf{h}_i$ is guaranteed. Within the mean-field treatment, this model has already demonstrated the most important properties of a TIM. That is: magnetic ordering at finite temperature can only be achieved when the transverse field is smaller than the many-body

interactions, for which the ordered magnetic moments are largely reduced due to non-vanishing transverse component (Fig. 5.3 (a) and (b)) [120]. Although the mean-field approximation overestimates the critical value of $\Delta/J(0)$ (here, $J(0) = \Sigma_i J_{ij}$ is defined as sum of spin-spin interactions at each site) as well as the magnetic ordering temperature [121], it provides a general picture of the TIM which will be instructive for the investigation of a frustrated TIM, such as MgHo in the present study.

5.3 Paramagnetic Dynamics

Before discussing the low-temperature behaviors, we now focus on the high-temperature paramagnetic region ($T > 4$ K $> J$) and use neutron-scattering experiments to reveal spin correlations. Normalized neutron scattering intensities as a function of momentum (Q) and energy transfer (ω) at various temperatures are plotted in Fig. 5.5 and 5.4, respectively. The $I_{\text{sub}}(Q)$ are obtained by subtracting high-temperature datasets, thereby presenting a good estimate of the purely magnetic scattering. Diffuse scattering with a broad peak centered at ≈ 0.65 $\mathring{A}$ is observed as the temperature is lowered, which is characteristic of ice-rule correlations in the parent pyrochlore spin ice compounds [109]. The $I(\omega)$ is background subtracted and is obtained by integrating Q from 0.4 $\mathring{A}$ to 1.6 $\mathring{A}$. From Fig. 5.5, three main features are observed: (i) a dominating central peak at quasi-elastic channel which is magnetic in origin, (ii) a broad tail extending to high energies, and (iii) a weak peak around 8 K which is clearly visible in all of the SEQUOIA data sets as well as on the negative-energy-transfer side of some DCS datasets (e.g., 4.2 K). By contrast, in systems where a transverse field is prohibited by a doublet ground state, spin fluctuations are much slower; e.g., the inelastic energy width is less than 0.1 K in $Ho_2Ti_2O_7$ at a temperature of 2 K [122]. When going away from the paramagnetic region, a shoulder develops at low energy ($\sim$2 K, very near the elastic line) when the temperature is lowered (0.4 K dataset).

It is useful to compare these results with the predictions of the Random Phase Approximation (RPA) theory [123]. At high temperature, RPA predicts that the entire spectral weight is contained in a single sharp peak at $\omega = \Delta$, corresponding to the crystal-field splitting. On cooling, the CEF excitation should split into three modes which acquire

dispersion because of the effect of the interactions; consequently, the single peak in $I(\omega)$ would broaden due to powder averaging the dispersive modes. No central peak is predicted at any temperature. These predictions disagree in almost all respects with the experimental results which show a strong central peak, broad inelastic scattering, and a sharp peak which is weak and nearly temperature independent.

We are not the first to observe this sort of behavior in a two-singlet system: the canonical two-singlet ferromagnet $LiTbF_4$ [119, 124, 125] shows features which are qualitatively very similar to MgHo, and the central peak is also a common feature of "soft mode" structural transitions [11]. Actually, all these features can be well modeled by a "relaxation-coupled oscillator "(RCO) model that was used to describe a canonical TIM system [124]. The imaginary part of the dynamic susceptibility of each mode in the RCO framework is given by

$$\chi_{uu}\left(\mathbf{Q},\omega\right)=\frac{\chi_0\left(0\right)\Delta^2}{\omega_u^2\left(\mathbf{Q}\right)-\omega^2-i\omega\gamma(\omega)},$$
$$\gamma(\omega)=\Gamma_0+\frac{\delta^2}{(\phi-i\omega)}, \tag{5.3}$$

where $\omega_u(\mathbf{Q})$ is the dispersion relation for collective oscillating modes of a TIM system and $\gamma(\omega)$ describes a damping function that contains couplings between the oscillating modes and the relaxing components. Here, Γ_0 is the damping constant, δ is the coupling coefficient between relaxing and oscillating modes, and ϕ is the energy width of the distribution of relaxing modes. In the limit of small ϕ (ϕ is much smaller than the instrument resolution in the current study), we can eliminates ϕ and reduce the imaginary part of $\chi_{uu}\left(\mathbf{Q},\omega\right)$ to the sum of a Lorentzian central peak and a damped harmonic oscillator whose frequency is renormalized as $\Omega_u^2(\mathbf{Q})=\omega_u^2(\mathbf{Q})+\delta^2$ [125]. The observation of the coexisting the high energy tail along with the 8 K peak suggests two damping modes, one that is strongly over-damped such that $\Gamma_0 \gg \Omega_u(\mathbf{Q})$ while the other is under-damped such that $\Gamma_1 < \Omega_u(\mathbf{Q})$. Within the RPA [123] and the Onsager reaction field correction [126], we reach a "RPA-Onsager-RCO" model to describe the scattering function, which finally allows us to fit $I_{\text{sub}}(Q)$ and $I_(\omega)$

simultaneously. The expression for the scattering function is:

$$S_{\Gamma_0,\Gamma_1}(\mathbf{Q},\omega) = \frac{\chi_0(0)\,\Delta^2}{N}\sum_{\mu}|F_\mu(\mathbf{Q})|^2\,\{\frac{T\delta^2 R(\omega)}{\omega_\mu^2(\mathbf{Q})\,\Omega_\mu^2(\mathbf{Q})} + \frac{\omega}{\pi\left[1-\exp\left(-\omega/T\right)\right]}\left[\frac{(1-f)\Gamma_0}{\left[\Omega_\mu^2(\mathbf{Q})-\omega^2\right]^2+(\omega\Gamma_0)^2}+\frac{f\Gamma_1}{\left[\Omega_\mu^2(\mathbf{Q})-\omega^2\right]^2+(\omega\Gamma_1)^2}\right]\}. \quad (5.4)$$

The model then contains five free parameters (Δ, δ, Γ_0, Γ_1, and f, the fraction of over-damped modes) where excellent fits over the whole paramagnetic region from 4.2 K to 40 K are obtained as shown in Fig. 5.6. The fitted values of the parameters are $J_{\rm nn} = 1.10$ (3) K, $\Delta = 3.09(2)$ K and $\delta = 7.77(3)$ K. We obtain a majority ($f = 96.2(3)\%$) of over-damped mode whose damping (Γ_0) increases with decreasing temperature. On the other hand, the remaining fraction (3.8(3)%) of the under-damped mode is temperature independent with $\Gamma_1 = 4.8(2)$ K, giving rise to the weak peak in $I(\omega)$ at an energy close to $\sqrt{\Delta^2+\delta^2} = 8.3$ K. It is noteworthy that simple models, such as the damped harmonic oscillator, do not give good fits of the spectrum. The successful consistency between our experimental observations and the RPA-Onsager-RCO model suggests that MgHo indeed behaves like a canonical two-singlet system at high temperatures, and the paramagnetic dynamics of the TIM might be universal.

5.4 Partially Ordered Ground State

We now turn to the low-temperature region ($T < \Delta$, J_{ij}) where the combination of frustration and quantum dynamics induced by the transverse field is expected to lead to non-trivial quantum states. We use specific heat and neutron-scattering measurements to reveal possible phase transitions and low-temperature spin dynamics. In the specific heat, a sharp peak is observed at $T^* = 0.32$ K (Fig.5.7), indicating a symmetry breaking transition. A Schottky-type broad peak is present in the same temperature range, which is due to the Hyperfine coupling between Ho^{3+} electronic and nuclear spins. The calculated nuclear specific heat assuming static moments of $10\,\mu_B/Ho^{3+}$ (red dashed line) obviously overestimates the height, while an alternative estimation, a fraction (75%) of static spins with reduced moment of $8\,\mu_B$

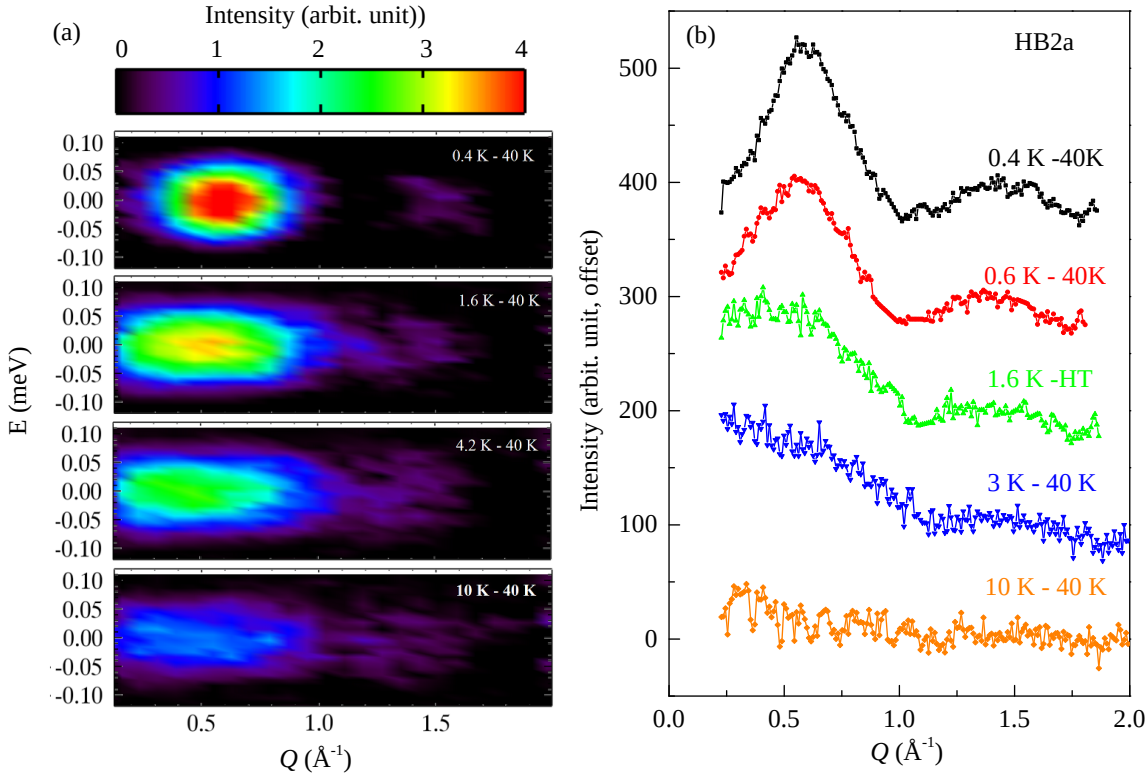

Figure 5.4: Overview of the experimental data of $I_{sub}(Q)$ measured at (a) DCS and (b) Hb-2a. $I_{sub}(Q)$ are obtained by subtracting high-temperature datasets from the temperatures of interest.

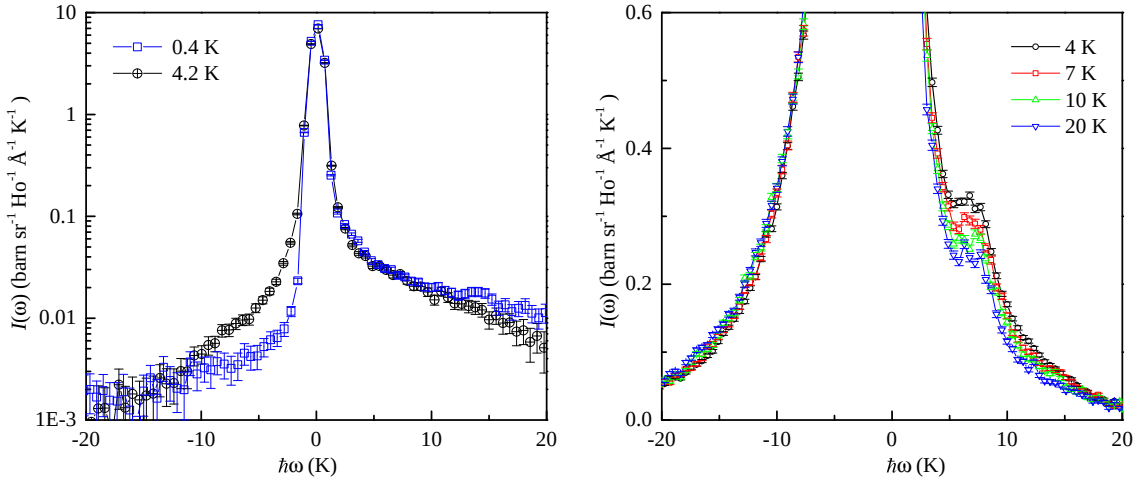

Figure 5.5: Overview of the experimental data of $I(\omega)$ measured at (a) SEQUOIA and (b) DCS. All data are normalized.

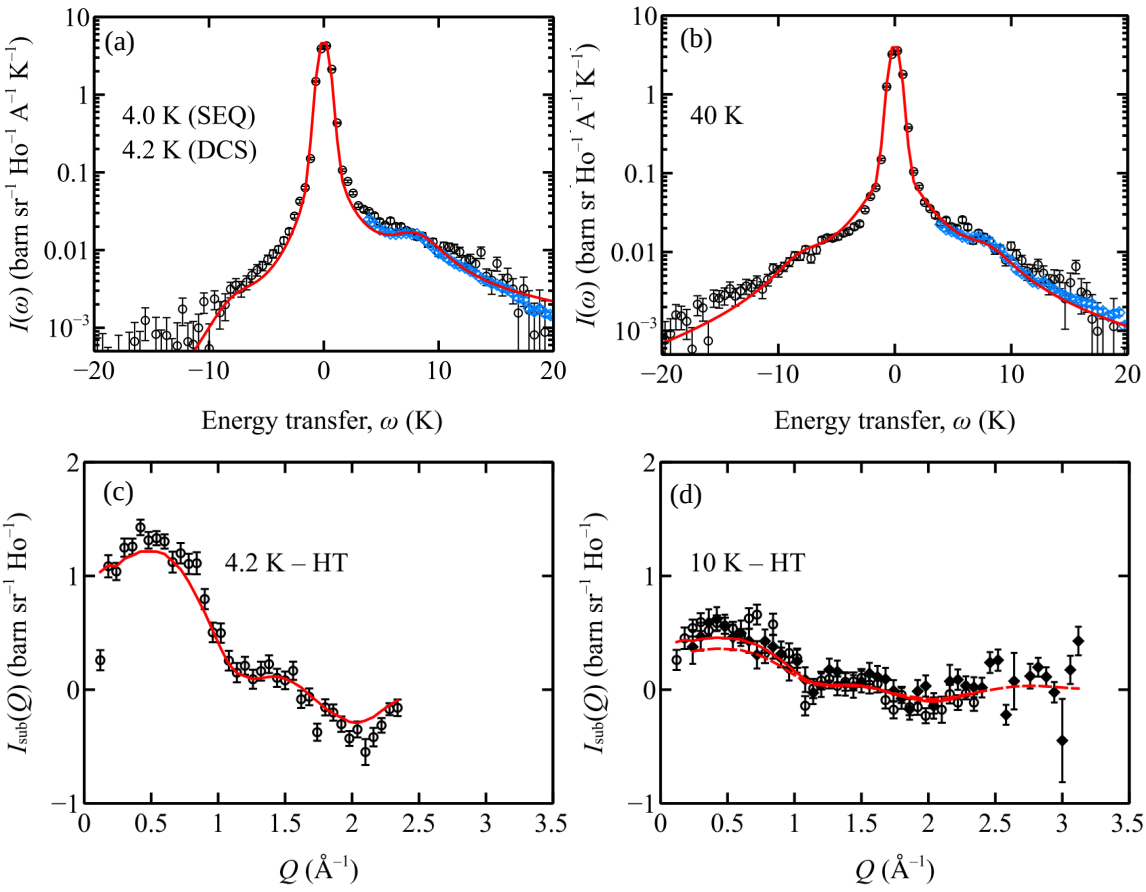

Figure 5.6: Experimental data (black circles) and fits (red lines) of the RPA-Onsager-RCO model described in the text to $I_{\rm sub}(\omega)$ and $I(Q)$. Fits were performed over the temperature range 4.0 K $\leq T \leq$ 40 K to DCS, SEQUOIA, and HB2A data simultaneously. All data are normalized. Error bars correspond to 1 standard error.

(black solid line), renders a reasonable subtraction for the low-temperature tail ($T < 0.2$ K) and gives a sensible estimation of the magnetic entropy associated with the subtracted data (Fig. Fig.5.7 inset). The fraction number and the reduced moment hints for entangled quantum correlations, which has also been observed in the quantum spin liquid candidate $Pr_2Zr_2O_7$ [29]. In fact, the nuclear specific heat can be treated as an efficient probe to examine the level of quantum fluctuations of the electronic spins and "measure" the fraction of moments that are still fluctuating.

Below T^*, two striking features are observed in our neutron-scattering data. The first feature is the emergence of structured excitations with the most prominent mode at around 3 K which is absent in the paramagnetic region (Fig. 5.8 (b)). This is in sharp contrast to the Kramers-ion variant MgDy in the TKL family [9], where the low-temperature dynamics are missing entirely in the observation window. Secondly, we found weak magnetic Bragg peaks appearing on top of broad diffuse scattering signals in $I_{\rm sub}(Q)$ (Fig. 5.8 (a)), consistent with a $q = 0$ all-in-all-out spin structure. The coexistence of the magnetic diffuse scattering and the Bragg peaks is reminiscent of the ECO state previously observed in MgDy [9]. However, here, the Rietveld refinement gives an ordered moment of $1.66(1)\,\mu_B$ per spin, which has been strongly reduced from the expected value of $3.33\,\mu_B$ for a classical ECO state. In addition, the diffuse scattering is not as sharp as that obtained from the ideal ECO state or that observed in MgDy. Since our structural refinements indicate no Ho/Mg site disorder, both effects are not likely due to defeat effects. Therefore, the observations in specific heat and neutron scattering indicate a new partially ordered state, which is beyond the description of the ECO state.

As the first attempt to understand this state, we solve the mean-field TIM Hamiltonian (Eq.5.2) for the TKL structure in the zero temperature limit. The expectation value of the effective moment on an arbitrary site is given by $\langle\sigma_i^z\rangle = 2h_i^z/(\sqrt{4(h_i^z)^2 + \Delta^2})$. Since h_i^z depends on the $\langle\sigma_j^z\rangle$ at nearby sites, an equilibrium can be be achieved only when the condition is satisfied for every site. It is easy to see that for a kagome antiferromagnet, a uniform h_i (in other words, a constant moment state) can never be achieved with non-zero Δ. This is in contrast to the similar problem on a pyrochlore lattice antiferromagnet where any state in the two-in-two-out spin-ice manifold naturally leads to a uniform h_i. The problem

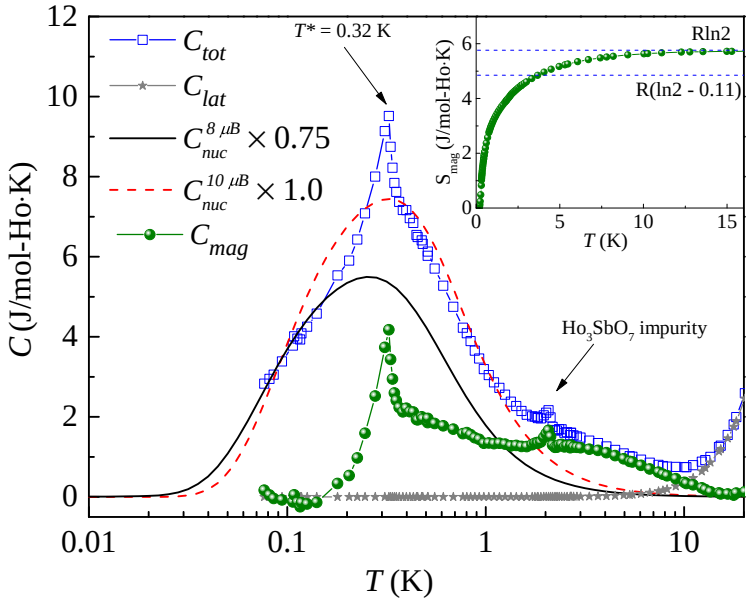

Figure 5.7: Specific heat of MgHo, showing following the contributions: total measured ($C_{\rm tot}$, blue squares), measured lattice ($C_{\rm lat}$, gray triangles), calculated nuclear contribution (the red dashed line for $C_{\rm nuc}^{10\mu_{\rm B}}$, and the black solid line for $C_{\rm nuc}^{8.1\mu_{\rm B}}$), subtracted magnetic ($C_{\rm mag} = C_{\rm tot} - 0.75C_{\rm nuc}^{8.1\mu_{\rm B}} - C_{\rm lat}$, green dots). Inset: magnetic entropy change $\Delta S_{\rm mag}$.

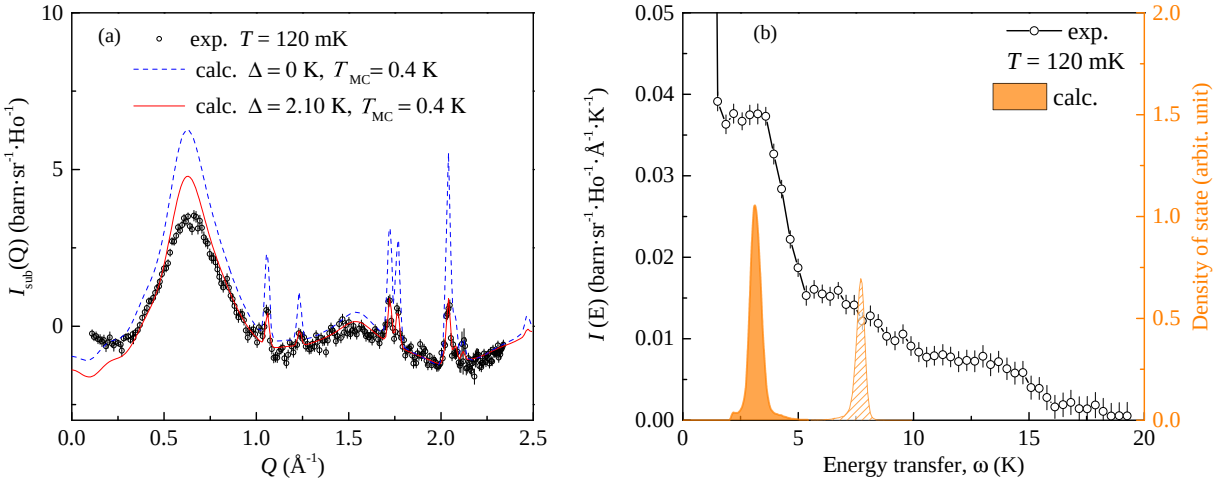

Figure 5.8: (a) Magnetic neutron-scattering data (black circles) at $T = 0.12$ K obtained by subtracting a high-temperature (average of 20 K and 40 K) measurement as background, calculations from classical ECO states at $T = 0.4$ K given by Monte Carlo (MC) annealing (blue dashed curve), and calculations from converged mean-field mmECO states with $\Delta = 2.1$ K (red curve) using the 0.4 K MC states as initial configurations. **b.** Energy dependence of the scattering intensity by integrating 0.4 to 1.6 Å^{-1} (black open circles), and the calculated density of state for the single-ion type spin excitations from mmECO states (orange area).

becomes even more interesting when the long-range dipolar interaction comes into play. To resolve the mean-field ground state, we evaluate the Hamiltonian numerically in real space. The principle is to compute h_i^z and update $\langle \sigma_i^z \rangle$ repeatedly until the convergence is reached. Using either random spin configurations or the more physically meaningful ECO configurations as initial states, a new type of ground state is found for which we call the moment modulated emergent charge order state (mmECO). Within this state, the characteristic of ECO is preserved, such that a two-in-one-out/one-in-two-out configuration is always found for every up/down triangle (or vice versa), forming a long range order of altering positive and negative emergent charges. However, a key difference is that the magnitudes of moment vary from site to site. For every triangle, there is one minority spin (empty arrows in Fig. 5.9 (a)) whose moment size is relatively larger than the other two majority spins (filled arrows in 5.9 (a)). Here, the non-uniform moment texture resembles a spin density wave that is usually found in metallic compounds but is hardly realized in a system with localized electrons. The statistical distribution of the moments forms a broad peak for the majority spins (filled peak in 5.9 (b)) and a narrow δ-function-like distribution for the minority spins (empty peak in 5.9 (b)). As a result, the statistics of the magnetic charges form a relatively narrow distribution around $\pm$ 0.5 (5.9 (b)). This corresponds to adding a spatial variation to the divergence full channel in the spin fragmentation theory [62, 127], while leaving the divergence free part intact. Alternatively, if we keep the divergence full part constant throughout the lattice, this gives rise to a soft breaking of the divergence free condition in the other channel. Either case calls for a generalization of the fragmentation theory.

In order to compare results with the experiments, we ran the mean-field calculation with various initial configurations and transverse fields with the nearest neighbor exchange $J_{\rm nn}$ = 1.0 K and the dipolar coupling D = 1.29 K fixed. In the case of classical ECO states as initial configurations, we notice that almost all spins in the final mmECO states remain parallel to spins in the initial configurations, resulting in large correlations with the initial ECO states. We further note that the classical ECO states from Monte Carlo (MC) simulations with the full ordered moment could exhibit different short range correlations depending on the temperature. The states deep in the ECO phase, for example 0.2 K, have

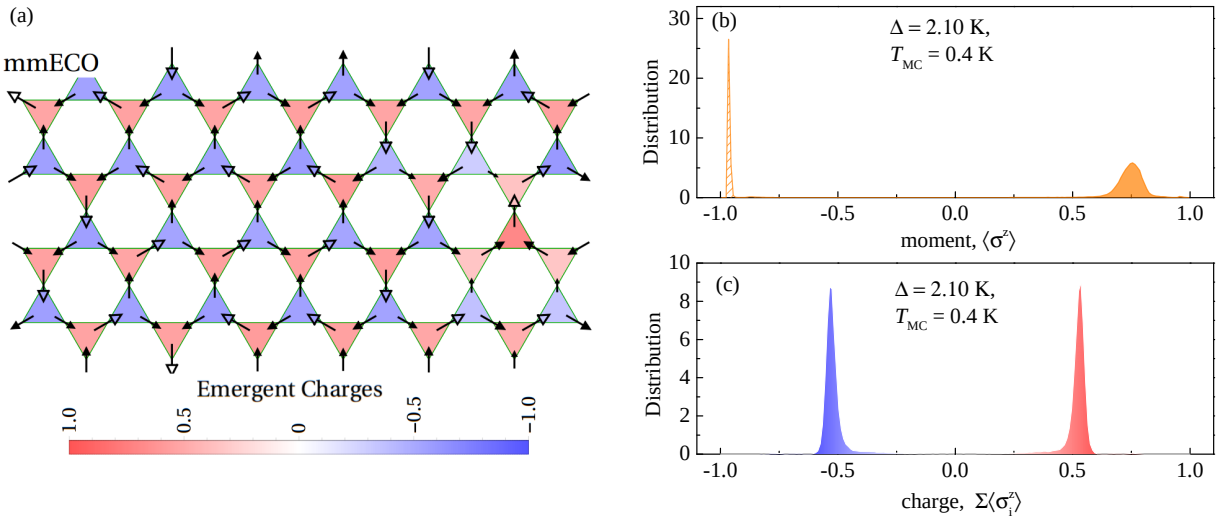

Figure 5.9: (a) A sample spin configuration of the mmECO state. The size of the arrows is scaled with the magnitude of the on-site expectation value $\langle \sigma_i^z \rangle$. Empty arrows are the minority spins with $\langle \sigma_i^z \rangle > 0.9$. Filled arrows are majority spins with $\langle \sigma_i^z \rangle < 0.9$. (b) The distribution of the on-site expectation values. The sign indicates if spins are parallel (positive) or anti-parallel (negative) to the local z-axes. (c) The distribution of emergent magnetic charges, defined as the sum of $\langle \sigma_i^z \rangle$ for each triangle.

a much sharper diffuse scattering pattern than that of states right after the phase transition (such as 0.4 K). We found that a good fit to both the diffuse scattering and the Bragg peak intensity can be achieved using the 0.4 K ECO states as initial configurations with $\Delta = 2.1$ K (Fig.5.8 (a)), where the broadness of the diffuse scattering is, to a large extent, inherited from the initial ECO states. Due to this very same observation, the 0.2 K ECO states lead to final configurations with diffuse scattering patterns that are too sharp compared to the data. In this sense, the quantum fluctuations in the system are described by thermal activation energy here such that the difference between 0.4 K and 0.2 K sets an energy scale for the quantum effects.

Our mean-field approach is able to provide useful information about the excitations as well. The energy gap between the ground state and the excited state on a single site is $\sqrt{4(h_i^z)^2 + \Delta^2}$. A counting for the mmECO states that give best fit to $I_{\text{sub}}(Q)$ reveals two peaks centered around 3.1 K and 7.7 K (Fig. 5.8 (b), which come from the sites of minority and of majority spins, respectively. This qualitatively explains the sharp mode around 3 K in the inelastic neutron spectrum, defining a characteristic energy of the system through

a single-spin-flip type of excitation ($|0_i^m\rangle \rightarrow |1_i^m\rangle$ in Fig. 5.1 (b)). Our mean-field model cannot, however, explain the continuous nature of the excitation spectrum and its high-energy tail, which suggests that non-trivial quantum correlations may play an important role.

5.5 Summary

The persisting quantum dynamics in both the paramagnetic and low temperature regions, the modulation of magnetic moments, and the fictionalization of emergent charge in the mmECO state clearly differentiate it from the ECO state expected for a classical system, demonstrating enhanced quantum effects due to the transverse fields. Meanwhile, since both Monte Carlo simulations [128, 129] and U(1) Gauge theory [130] predict a spin liquid state for a kagome antiferromagnet under weak transverse fields and in the absence of dipolar interaction, the mmECO state found here opens a new window for possible exotic states when quantum fluctuations are combined with long range interactions. In summary, MgHo introduces quantum dynamics in the exotic phase of ECO and realizes for the first time a frustrated TIM, making it the simplest experimental system for studying quantum many-body problems on a frustrated lattice and an excellent candidate to realize quantum kagome ice physics.

Chapter 6

Conclusion and Outlook

This dissertation focused on the structural and magnetic properties of our newly discovered rare earth TKL compounds $A_2RE_3Sb_3O_{14}$ (A = Mg, Zn; RE = Pr, Nd, Gd, Tb, Dy, Ho, Er, Yb), which were achieved by partially substituting the ions in the cubic pyrochlore lattice. Their unique structure and rich spin types provide us a platform to realize exotic kagome-based physics.

This dissertation provides a comprehensive study of their low temperature magnetism by means of susceptibility and specific heat measurements, which have revealed various magnetic ground states. These include the non-magnetic singlet state for MgPr, ZnPr, LROs for MgGd, ZnGd, MgNd, ZnNd, and MgYb, a long range ECO state for MgDy, ZnDy, possible SG states for ZnEr, ZnHo, and the absence of spin ordering down to 80 mK for MgEr, MgTb, ZnTb, and ZnYb compounds. The ground states observed here bear both similarities as well as striking differences from the states found in the parent pyrochlore systems. In particular, while the TKLs display a greater tendency towards LRO, the lack of LRO in MgHo, MgTb and ZnTb can be viewed from the standpoint of a balance among spin-spin interactions, anisotropies, and the non-Kramers nature of the single ion state. While substituting Zn for Mg changes the chemical pressure and subtly modifies the interaction energies for compounds with larger RE ions, this substitution introduces structural disorder and modifies the ground states for compounds with smaller RE ions (Ho, Er, Yb).

We have shown that the TKLs with non-Kramers ion are essentially the first experimental realization of TIM on a frustrated lattice. In addition, we performed elastic and inelastic

neutron scattering measurements on MgHo, illustrating a unique mmECO ground state, along with persisting quantum dynamics all the way from the paramagnetic region to the partially ordered state. Using extracted parameters from neutron data, we explain our observations within a mean-field model incorporating the effects of quantum dynamics and frustration. These results establish MgHo as a quantum kagome ice from the TIM.

The results shown in this dissertation, along with other pioneering studies (e.g. the studies for MgDy [9] and MgNd [86]) have illustrated the general properties and some exciting physics of the system. However, there are a lot of questions waiting to be answered.

On the experimental side, future CEF excitation measurements will be important for determining the CEF levels, g-tensors, as well as confirming the spin anisotropies for TKL members. Since no LRO is observed down to 50 mK in MgTb, ZnTb, MgEr, and ZnYb, these four TKL systems are promising candidates for hosting QSL states. Other experiments, including neutron scattering, μSR, and NMR will be helpful to identify the nature of their ground states as well as the spin correlations. Since QSL states are characterized by the presence or absence of a gap in the anyon excitation spectrum, it is important to determine if any of the QSL candidate TKLs possess such a gap. For Nd-KLs, the nature of the two-step order needs to be addressed. Measurements under weak magnetic fields are needed to provide insight into this question. Interpreting such measurements will be difficult, given the present polycrystalline samples, but coarse-grained behavior can be studied. For Gd-TKLs, our theoretical investigation based on the Luttinger-Tisza method predicts a 120 $^\circ$ spin structure. Confirmations are needed by other direct measurements. For MgDy, neutron scattering experiments based on a powder sample with 4-6% site disorder have identified an ECO with average spin LRO ground state. We expect a similar ground state in ZnDy. A question then would be whether or not perfect samples (lacking any site disorder) give rise to true LRO of the Dy^{3+} spins, as predicted by the theory [114]. For MgHo, the exact nature of the mmECO state as well as its collective excitation needs to be understood better. For MgEr, the nature of the 80 mK peak in χ'_{ac} remains unclear, and it is unknown whether the 2.1 K transition in C_{mag} is indeed a KT transition. It is also not clear what the LRO state for MgYb is exactly. Future studies are needed to answer all these questions.

On the theoretical side, due to the uniqueness of the tripod-like local Ising/XY anisotropy on a kagome lattice, there are limited theoretical works at the moment that suitably describe the TKL system. Our theoretical investigation using a Luttinger-Tisza type theory provides a first universal mean-field level description of the TKL. Aside from this, there are few existing theoretical studies that can be directly adopted. For Heisenberg spins, Moessner et al. considered classical dipoles on a 2D kagome lattice and calculated a phase diagram by scaling dipolar and exchange interactions [8]. This model might be a good starting point for the Gd-TKLs. For Ising spins, models with TKL-like canted Ising spins have predicted an ECO followed by a spin LRO transition on a kagome lattice [114], which seems to successfully explain the experimental observation for MgDy. The other two Ising compounds, Tb and Ho-TKLs, have non-Kramers ions, and therefore belong to the TIM family. Although our mean field method successfully explains many of the observations in MgHo, more advanced theoretical tools, such as quantum Monte Carlo [131] and multi-scale entanglement renormalization ansatz [132], will be necessary to take into account entanglement and to construct a real quantum model. For both compounds, the long range dipolar interaction is needed to be included which is absent in the previous study of TIMs [129, 130, 133]. For XY spins, there are even fewer (if any) theoretical studies since the situation of three distinct local XY planes has most likely not been previously considered before the realization of the TKL. Therefore, the TKLs offer an unexplored realm of theory.

The future exploration of the whole TKL family is expected to open a new field in condensed matter physics and materials science studies, just as the pyrochlore did during the last two decades. We hope our results will stimulate both experimental and theoretical studies on these exciting compounds.

Bibliography

[1] C. A. Morrison and R. P. Leavitt. Handbook on the Physics and Chemistry of Rare Earths. *North Holland Publishing Company*, 1982. x, 5

[2] C. Castelnovo, R. Moessner, and S. L. Sondhi. Magnetic monopoles in spin ice. *Nature*, 451(7174):42–45, 2008. x, 6, 34

[3] H. Kadowaki, Y. Ishii, K. Matsuhira, and Y. Hinatsu. Neutron scattering study of dipolar spin ice $Ho_2Sn_2O_7$: frustrated pyrochlore magnet. *Phys. Rev. B*, 65(14):144421, 2002. x, 6

[4] M. J. P. Gingras and P. A. McClarty. Quantum spin ice: a search for gapless quantum spin liquids in pyrochlore magnets. *Reports on Progress in Physics*, 77(5):056501, 2014. x, 7, 8

[5] L. Savary and L. Balents. Coulombic quantum liquids in spin-1/2 pyrochlores. *Phys. Rev. Lett.*, 108(3):037202, 2012. x, 7, 8, 56

[6] T.-H. Han, J. S. Helton, S. Chu, D. G. Nocera, J. A. Rodriguez-Rivera, C. Broholm, and Y. S. Lee. Fractionalized excitations in the spin-liquid state of a kagome-lattice antiferromagnet. *Nature*, 492(7429):406–410, 2012. x, 10, 11

[7] G.-W. Chern, P. Mellado, and O. Tchernyshyov. Two-stage ordering of spins in dipolar spin ice on the kagome lattice. *Phys. Rev. Lett.*, 106(20):207202, 2011. xi, 12, 47, 48

[8] M. Maksymenko, V. R. Chandra, and R. Moessner. Classical dipoles on the kagome lattice. *Phys. Rev. B*, 91(18):184407, 2015. xii, 13, 42, 43, 78

[9] J. A. M. Paddison, H. S. Ong, J. O. Hamp, P. Mukherjee, X. J. Bai, M. G. Tucker, N. P. Butch, C. Castelnovo, M. Mourigal, and S. E. Dutton. Emergent order in the kagome Ising magnet $Dy_3Mg_2Sb_3O_{14}$. *Nature Communications*, 7, 2016. xii, 27, 32, 46, 47, 48, 60, 62, 65, 71, 77

[10] S. Rosenkranz, A. P. Ramirez, A. Hayashi, R. J. Cava, R. Siddharthan, and B. S. Shastry. Crystal-field interaction in the pyrochlore magnet $Ho_2Ti_2O_7$. *Journal of Applied Physics*, 87(9):5914–5916, 2000. xiii, 63, 64

[11] G. Shirane and J. D. Axe. Acoustic-phonon instability and critical scattering in Nb_3Sb. *Phys. Rev. Lett.*, 27(26):1803, 1971. xiii, 64, 67

[12] J. Oitmaa, M. Plischke, and T. A. Winchester. High-temperature dynamics of the Ising model in a transverse field. *Phys. Rev. B*, 29(3):1321, 1984. xiii, 64

[13] L. Balents. Spin liquids in frustrated magnets. *Nature*, 464(7286):199, 2010. 1, 2, 3, 7, 61

[14] G. H. Wannier. Antiferromagnetism. the triangular Ising net. *Phys. Rev.*, 79(2):357, 1950. 2

[15] S. T. Bramwell and M. J. P. Gingras. Spin ice state in frustrated magnetic pyrochlore materials. *Science*, 294(5546):1495–1501, 2001. 2, 34, 48, 56, 61

[16] A. S. Wills, R. Ballou, and C. Lacroix. Model of localized highly frustrated ferromagnetism: The kagomé spin ice. *Phys. Rev. B*, 66(14):144407, 2002. 2, 12, 50, 61

[17] P. W. Anderson. The Resonating Valence Bond State in La_2CuO_4 and Superconductivity. *Science (New York, NY)*, 235(4793):1196, 1987. 3

[18] S. Liang, B. Doucot, and P. W. Anderson. Some new variational resonating-valence-bond-type wave functions for the spin-1/2 antiferromagnetic Heisenberg model on a square lattice. *Phys. Rev. Lett.*, 61(3):365, 1988. 3

[19] X.-G. Wen. Quantum orders and symmetric spin liquids. *Phys. Rev. B*, 65(16):165113, 2002. 3

[20] X.-G. Wen. Topological order: From long-range entangled quantum matter to a unified origin of light and electrons. *ISRN Condensed Matter Physics*, 2013, 2013. 3

[21] G. Misguich, C. Lhuillier, and H. T. Diep. Frustrated spin systems, 2005. 3

[22] F. D. M. Haldane. Spinon gasdescription of the S=1/2 Heisenberg chain with inverse-square exchange: Exact spectrum and thermodynamics. *Phys. Rev. Lett.*, 66(11):1529, 1991. 3

[23] A. P. Ramirez. Strongly geometrically frustrated magnets. *Annual Review of Materials Science*, 24(1):453–480, 1994. 4

[24] J. D. M. Champion, A. S. Wills, T. Fennell, S. T. Bramwell, J. S. Gardner, and M. A. Green. Order in the Heisenberg pyrochlore: The magnetic structure of $Gd_2Ti_2O_7$. *Phys. Rev. B*, 64(14):140407, 2001. 4

[25] A. P. Ramirez, B. S. Shastry, A. Hayashi, J. J. Krajewski, D. A. Huse, and R. J. Cava. Multiple Field-Induced Phase Transitions in the Geometrically Frustrated Dipolar Magnet: $Gd_2Ti_2O_7$. *Phys. Rev. Lett.*, 89(6):067202, 2002. 4

[26] M. J. Harris, S. T. Bramwell, D. F. McMorrow, T. H. Zeiske, and K. W. Godfrey. Geometrical frustration in the ferromagnetic pyrochlore $Ho_2Ti_2O_7$. *Phys. Rev. Lett.*, 79(13):2554, 1997. 4, 5, 56

[27] A. P. Ramirez, A. Hayashi, R. J. Cava, R. Siddharthan, and B. S. Shastry. Zero-point entropy in spin ice. *Nature*, 399(6734):333–335, 1999. 4, 5, 48

[28] H. D. Zhou, C. R. Wiebe, J. A. Janik, L. Balicas, Y. J. Yo, Y. Qiu, J. R. D. Copley, and J. S. Gardner. Dynamic spin ice: $Pr_2Sn_2O_7$. *Phys. Rev. Lett.*, 101(22):227204, 2008. 4, 9, 37

[29] K. Kimura, S. Nakatsuji, J. J. Wen, C. Broholm, M. B. Stone, E. Nishibori, and H. Sawa. Quantum fluctuations in spin-ice-like $Pr_2Zr_2O_7$. *Nature communications*, 4, 2013. 4, 9, 37, 57, 71

[30] J. S. Gardner, S. R. Dunsiger, B. D. Gaulin, M. J. P. Gingras, J. E. Greedan, R. F. Kiefl, M. D. Lumsden, W. A. MacFarlane, N. P. Raju, J. E. Sonier, et al. Cooperative paramagnetism in the geometrically frustrated pyrochlore antiferromagnet $Tb_2Ti_2O_7$. *Phys. Rev. Lett.*, 82(5):1012, 1999. 4

[31] K. A. Ross, L. Savary, B. D. Gaulin, and L. Balents. Quantum excitations in quantum spin ice. *Phys. Rev. X*, 1(2):021002, 2011. 4, 9, 56, 61

[32] L. Savary, K. A. Ross, B. D. Gaulin, J. P. C. Ruff, and L. Balents. Order by quantum disorder in $Er_2Ti_2O_7$. *Phys. Rev. Lett.*, 109(16):167201, 2012. 4, 56

[33] L. Pauling. The structure and entropy of ice and of other crystals with some randomness of atomic arrangement. *Journal of the American Chemical Society*, 57 (12):2680–2684, 1935. 5

[34] L. D. C. Jaubert and P. C. W. Holdsworth. Signature of magnetic monopole and Dirac string dynamics in spin ice. *Nature Physics*, 5(4):258–261, 2009. 6

[35] D. J. P. Morris, D. A. Tennant, S. A. Grigera, B. Klemke, C. Castelnovo, R. Moessner, C. Czternasty, M. Meissner, K. C. Rule, J.-U. Hoffmann, et al. Dirac strings and magnetic monopoles in the spin ice $Dy_2Ti_2O_7$. *Science*, 326(5951):411–414, 2009. 6

[36] S. R. Giblin, S. T. Bramwell, P. C. W. Holdsworth, D. Prabhakaran, and I. Terry. Creation and measurement of long-lived magnetic monopole currents in spin ice. *Nature Physics*, 7(3):252–258, 2011. 6

[37] C. Castelnovo, R. Moessner, and S. L. Sondhi. Spin ice, fractionalization, and topological order. *Annu. Rev. Condens. Matter Phys.*, 3(1):35–55, 2012. 7

[38] M. Hermele, M. P. A. Fisher, and L. Balents. Pyrochlore photons: The U (1) spin liquid in a S=1/2 three-dimensional frustrated magnet. *Phys. Rev. B*, 69(6):064404, 2004. 7, 61

[39] N. Shannon, O. Sikora, F. Pollmann, K. Penc, and P. Fulde. Quantum ice: a quantum Monte Carlo study. *Phys. Rev. Lett.*, 108(6):067204, 2012. 7

[40] S. H. Curnoe. Structural distortion and the spin liquid state in $Tb_2Ti_2O_7$. *Phys. Rev. B*, 78(9):094418, 2008. 7

[41] H. R. Molavian, M. J. P. Gingras, and B. Canals. Dynamically induced frustration as a route to a quantum spin ice state in $tb_2ti_2o_7$ via virtual crystal field excitations and quantum many-body effects. *Phys. Rev. Lett.*, 98(15):157204, 2007. 8, 45

[42] J. S. Gardner, B. D. Gaulin, A. J. Berlinsky, P. Waldron, S. R. Dunsiger, N. P. Raju, and J. E. Greedan. Neutron scattering studies of the cooperative paramagnet pyrochlore $Tb_2Ti_2O_7$. *Phys. Rev. B*, 64(22):224416, 2001. 8

[43] Y.-J. Kao, M. Enjalran, A. Del Maestro, H. R. Molavian, and M. J. P. Gingras. Understanding paramagnetic spin correlations in the spin-liquid pyrochlore $Tb_2Ti_2O_7$. *Phys. Rev. B*, 68(17):172407, 2003. 8

[44] P. Bonville, I. Mirebeau, A. Gukasov, S. Petit, and J. Robert. Tetragonal distortion yielding a two-singlet spin liquid in pyrochlore $tb_2ti_2o_7$. *Phys. Rev. B*, 84(18):184409, 2011. 8, 45

[45] J. P. Clancy, J. P. C. Ruff, S. R. Dunsiger, Y. Zhao, H. A. Dabkowska, J. S. Gardner, Y. Qiu, J. R. D. Copley, T. Jenkins, and B. D. Gaulin. Revisiting static and dynamic spin-ice correlations in $Ho_2Ti_2O_7$ with neutron scattering. *Phys. Rev. B*, 79(1):014408, 2009. 9

[46] J.-J. Wen, S. M. Koohpayeh, K. A. Ross, B. A. Trump, T. M. McQueen, K. Kimura, S. Nakatsuji, Y. Qiu, D. M. Pajerowski, J. R. D. Copley, et al. Disordered Route to the Coulomb Quantum Spin Liquid: Random Transverse Fields on Spin Ice in $Pr_2Zr_2O_7$. *Phys. Rev. Lett.*, 118(10):107206, 2017. 9, 57, 61

[47] L. Savary and L. Balents. Disorder-Induced Quantum Spin Liquid in Spin Ice Pyrochlores. *Phys. Rev. Lett.*, 118(8):087203, 2017. 9, 57, 62

[48] J. A. Hodges, P. Bonville, A. Forget, A. Yaouanc, P. Dalmas. De Réotier, G. André, M. Rams, K. Królas, C. Ritter, P. C. M. Gubbens, et al. First-order transition in the spin dynamics of geometrically frustrated $Yb_2Ti_2O_7$. *Phys. Rev. Lett.*, 88(7):077204, 2002. 9

[49] L.-J. Chang, S. Onoda, Y. Su, Y.-J. Kao, K.-D. Tsuei, Y. Yasui, K. Kakurai, and M. R. Lees. Higgs transition from a magnetic Coulomb liquid to a ferromagnet in $Yb_2Ti_2O_7$. *Nature communications*, 3:992, 2012. 9

[50] J. D. Thompson, P. A. McClarty, D. Prabhakaran, I. Cabrera, T. Guidi, and R. Coldea. Quasiparticle Breakdown and Spin Hamiltonian of the Frustrated Quantum Pyrochlore $Yb_2Ti_2O_7$ in Magnetic Field. *arXiv preprint arXiv:1703.04506*, 2017. 9, 61

[51] A. P. Ramirez, G. P. Espinosa, and A. S. Cooper. Strong frustration and dilution-enhanced order in a quasi-2d spin glass. *Phys. Rev. Lett.*, 64(17):2070, 1990. 10

[52] P. Tomczak and J. Richter. Ground state of the spin-1/2 Heisenberg antiferromagnet on a two-dimensional square-hexagonal-dodecagonal lattice. *Phys. Rev. B*, 59(1):107, 1999. 10

[53] M. R. Norman. Colloquium: Herbertsmithite and the search for the quantum spin liquid. *Rev. Mod. Phys.*, 88(4):041002, 2016. 11

[54] P. Mendels, F. Bert, M. A. De Vries, A. Olariu, A. Harrison, F. Duc, J. C. Trombe, J. S. Lord, A. Amato, and C. Baines. Quantum magnetism in the paratacamite family: towards an ideal kagomé lattice. *Phys. Rev. Lett.*, 98(7):077204, 2007. 11

[55] J. S. Helton, K. Matan, M. P. Shores, E. A. Nytko, B. M. Bartlett, Y. Yoshida, Y. Takano, A. Suslov, Y. Qiu, J.-H. Chung, et al. Spin dynamics of the spin-1/2 kagome lattice antiferromagnet $ZnCu_3(OH)_6Cl_2$. *Phys. Rev. Lett.*, 98(10):107204, 2007. 11

[56] S.-H. Lee, H. Kikuchi, Y. Qiu, B. Lake, Q. Huang, K. Habicht, and K. Kiefer. Quantum-spin-liquid states in the two-dimensional kagome antiferromagnets $ZnCu_{4-x}(OD)_6Cl_2$. *Nature Materials*, 6(11):853–857, 2007. 11

[57] D. E. Freedman, T.-H. Han, A. Prodi, P. Muller, Q.-Z. Huang, Y.-S. Chen, S. M. Webb, Y. S. Lee, T. M. McQueen, and D. G. Nocera. Site specific X-ray anomalous dispersion of the geometrically frustrated Kagome magnet, herbertsmithite, $ZnCu_3(OH)_6Cl_2$. *Journal of the American Chemical Society*, 132(45):16185–16190, 2010. 11

[58] T.-H. Han, M. R. Norman, J. J. Wen, J. A. Rodriguez-Rivera, J. S. Helton, C. Broholm, and Y. S. Lee. Correlated impurities and intrinsic spin-liquid physics in the kagome material herbertsmithite. *Phys. Rev. B*, 94(6):060409, 2016. 11

[59] R. Liebmann. Statistical mechanics of periodic frustrated ising systems. In *Statistical Mechanics of Periodic Frustrated Ising Systems*, volume 251, 1986. 11

[60] Y. Tabata, H. Kadowaki, K. Matsuhira, Z. Hiroi, N. Aso, E. Ressouche, and B. Fåk. Kagome ice state in the dipolar spin ice $Dy_2Ti_2O_7$. *Phys. Rev. Lett.*, 97(25):257205, 2006. 13

[61] T. Fennell, S. T. Bramwell, D. F. McMorrow, P. Manuel, and A. R. Wildes. Pinch points and kasteleyn transitions in kagome ice. *Nature Physics*, 3(8):566–572, 2007. 13, 47

[62] B. Canals, I.-A. Chioar, V.-D. Nguyen, M. Hehn, D. Lacour, F. Montaigne, A. Locatelli, T. O. Menteş, B. S. Burgos, and N. Rougemaille. Fragmentation of magnetism in artificial kagome dipolar spin ice. *Nature communications*, 7, 2016. 13, 47, 73

[63] R. Schaffer, S. Bhattacharjee, and Y. B. Kim. Spin-orbital liquids in non-Kramers magnets on the kagome lattice. *Phys. Rev. B*, 88(17):174405, 2013. 13

[64] Y. Zhao, W. Li, B. Xi, Z. Zhang, X. Yan, S.-J. Ran, T. Liu, and G. Su. Kosterlitz-thouless phase transition and re-entrance in an anisotropic three-state potts model on the generalized kagome lattice. *Phys. Rev. E*, 87(3):032151, 2013. 13

[65] S. Sachdev. Kagomé-and triangular-lattice heisenberg antiferromagnets: Ordering from quantum fluctuations and quantum-disordered ground states with unconfined bosonic spinons. *Phys. Rev. B*, 45(21):12377, 1992. 13

[66] T. Picot and D. Poilblanc. Nematic and supernematic phases in kagome quantum antiferromagnets under the influence of a magnetic field. *Phys. Rev. B*, 91(6):064415, 2015. 13

[67] Y. Okamoto, H. Yoshida, and Z. Hiroi. Vesignieite $BaCu_3V_2O_8(OH)_2$ as a candidate spin-1/2 kagome antiferromagnet. *Journal of the Physical Society of Japan*, 78(3): 033701–033701, 2009. 13

[68] T.-H. Han, J. Singleton, and J. A. Schlueter. Barlowite: a spin-1/2 antiferromagnet with a geometrically perfect kagome motif. *Phys. Rev. Lett.*, 113(22):227203, 2014. 13

[69] J. Rodríguez-Carvajal. Recent advances in magnetic structure determination by neutron powder diffraction. *Physica B: Condensed Matter*, 192(1-2):55–69, 1993. 16

[70] R. J. Elliott and K. W. H. Stevens. The theory of magnetic resonance experiments on salts of the rare earths. In *Proceedings of the Royal Society of London A: Mathematical, Physical and Engineering Sciences*, volume 218, pages 553–566. The Royal Society, 1953. 16

[71] M. Krusius, A. C. Anderson, and B. Holmström. Calorimetric investigation of hyperfine interactions in metallic Ho and Tb. *Phys. Rev.*, 177(2):910, 1969. 17

[72] Z. L. Dun, M. Lee, E. S. Choi, A. M. Hallas, C. R. Wiebe, J. S. Gardner, E. Arrighi, R. S. Freitas, A. M. Arevalo-Lopez, J. P. Attfield, et al. Chemical pressure effects on magnetism in the quantum spin liquid candidates $Yb_2X_2O_7$ (X= Sn, Ti, Ge). *Phys. Rev. B*, 89(6):064401, 2014. 18, 54, 59

[73] T. Sato and Y. Miyako. Nonlinear Susceptibility and Specific Heat of $(Pd_{0.9966}Fe_{0.0034})_{0.95}Mn_{0.05}$. *Journal of the Physical Society of Japan*, 51(5):1394–1400, 1982. 19

[74] A. Furrer, T. StrÃ, et al. *Neutron scattering in condensed matter physics*. World Scientific Publishing Co Inc, 2009. 19, 22

[75] V. O. Garlea, B. C. Chakoumakos, S. A. Moore, G. B. Taylor, T. Chae, R. G. Maples, R. A. Riedel, G. W. Lynn, and D. L. Selby. The high-resolution powder diffractometer at the high flux isotope reactor. *Applied Physics A*, 99(3):531–535, 2010. 21

[76] G. E. Granroth, A. I. Kolesnikov, T. E. Sherline, J. P. Clancy, K. A. Ross, J. P. C. Ruff, B. D. Gaulin, and S. E. Nagler. SEQUOIA: A newly operating chopper spectrometer at the SNS. In *Journal of Physics: Conference Series*, volume 251, page 012058. IOP Publishing, 2010. 22

[77] J. R. D. Copley and J. C. Cook. The Disk Chopper Spectrometer at NIST: a new instrument for quasielastic neutron scattering studies. *Chemical Physics*, 292(2):477–485, 2003. 22

[78] R. T. Azuah, L. R. Kneller, Y. Qiu, P. L. W. Tregenna-Piggott, C. M. Brown, J. R. D. Copley, and R. M. Dimeo. DAVE: a comprehensive software suite for the reduction, visualization, and analysis of low energy neutron spectroscopic data. *Journal of Research of the National Institute of Standards and Technology*, 114(6):341, 2009. 23

[79] K. Li, Y. F. Hu, Y. X. Wang, T. Kamiyama, B. Wang, Z. Li, and J. Lin. Syntheses and properties of a family of new compounds $RE_3Sb_3Co_2O_{14}$ (RE= La, Pr, Nd, Sm–Ho) with an ordered pyrochlore structure. *Journal of Solid State Chemistry*, 217:80–86, 2014. 24

[80] W. T. Fu and D. J. W. IJdo. Crystal structure of $Mn_2Ln_3Sb_3O_{14}$ (Ln= La, Pr and Nd): A new ordered rhombohedral pyrochlore. *Journal of Solid State Chemistry*, 213: 165–168, 2014. 24

[81] M. B. Sanders, J. W. Krizan, and R. J. Cava. $RE_3Sb_3Zn_2O_{14}$ (RE= La, Pr, Nd, Sm, Eu, Gd): a new family of pyrochlore derivatives with rare earth ions on a 2D Kagome lattice. *Journal of Materials Chemistry C*, 4(3):541–550, 2016. 24, 25

[82] M. B Sanders, K. M. Baroudi, J. W. Krizan, O. A. Mukadam, and R. J. Cava. Synthesis, crystal structure, and magnetic properties of novel 2D kagome materials $RE_3Sb_3Mg_2O_{14}$ (RE= La, Pr, Sm, Eu, Tb, Ho): Comparison to $RE_3Sb_3Zn_2O_{14}$ family. *physica status solidi (b)*, 253(10):2056–2065, 2016. 25

[83] W. T. Fu and D. J. W. IJdo. New rhombohedral pyrochlores $Ca_2Ln_3Sb_3O_{14}$ (Ln= lanthanide and Y): Space group revised. *Journal of Solid State Chemistry*, 229:330–335, 2015. 27

[84] A Bertin, Y Chapuis, P Dalmas de Réotier, and A Yaouanc. Crystal electric field in the r2ti2o7 pyrochlore compounds. *Journal of Physics: Condensed Matter*, 24(25): 256003, 2012. 31

[85] T Sakakibara, T Tayama, Z Hiroi, Kazuyuki Matsuhira, and Seishi Takagi. Observation of a liquid-gas-type transition in the pyrochlore spin ice compound d y 2 t i 2 o 7 in a magnetic field. *Phys. Rev. Lett.*, 90(20):207205, 2003. 31

[86] A. Scheie, M. Sanders, J. Krizan, Y. Qiu, R. J. Cava, and C. Broholm. Effective spin-1 2 scalar chiral order on kagome lattices in $Nd_3Sb_3Mg_2O_{14}$. *Phys. Rev. B*, 93(18): 180407, 2016. 32, 39, 41, 55, 77

[87] K. W. H. Stevens. Matrix elements and operator equivalents connected with the magnetic properties of rare earth ions. *Proceedings of the Physical Society. Section A*, 65(3):209, 1952. 32

[88] I. D. Ryabov. On the generation of operator equivalents and the calculation of their matrix elements. *Journal of Magnetic Resonance*, 140(1):141–145, 1999. 33

[89] U. Walter. Treating crystal field parameters in lower than cubic symmetries. *Journal of Physics and Chemistry of Solids*, 45(4):401–408, 1984. 33, 58

[90] Charles Kittel. *Introduction to solid state physics*. Wiley, 2005. 34

[91] M. J. P. Gingras, B. C. Den Hertog, M. Faucher, J. S. Gardner, S. R. Dunsiger, L. J. Chang, B. D. Gaulin, N. P. Raju, and J. E. Greedan. Thermodynamic and single-ion properties of Tb^{3+} within the collective paramagnetic-spin liquid state of the frustrated pyrochlore antiferromagnet $Tb_2Ti_2O_7$. *Phys. Rev. B*, 62(10):6496, 2000. 35

[92] A. J. Princep, D. Prabhakaran, A. T. Boothroyd, and D. T. Adroja. Crystal-field states of pr^{3+} in the candidate quantum spin ice $Pr_2Sn_2O_7$. *Phys. Rev. B*, 88(10): 104421, 2013. 37

[93] A. Bertin, P. Dalmas. de Réotier, B. Fåk, C. Marin, A. Yaouanc, A. Forget, D. Sheptyakov, B. Frick, C. Ritter, A. Amato, et al. $Nd_2Sn_2O_7$: An all-in–all-out pyrochlore magnet with no divergence-free field and anomalously slow paramagnetic spin dynamics. *Phys. Rev. B*, 92(14):144423, 2015. 39, 41

[94] A. M. Hallas, A. M. Arevalo-Lopez, A. Z. Sharma, T. Munsie, J. P. Attfield, C. R. Wiebe, and G. M. Luke. Magnetic frustration in lead pyrochlores. *Phys. Rev. B*, 91 (10):104417, 2015. 39

[95] S. T. Bramwell, M. N. Field, M. J. Harris, and I. P. Parkin. Bulk magnetization of the heavy rare earth titanate pyrochlores-a series of model frustrated magnets. *Journal of Physics: Condensed Matter*, 12(4):483, 2000. 41, 45, 52

[96] N. D. Mermin and H. Wagner. Absence of ferromagnetism or antiferromagnetism in one-or two-dimensional isotropic Heisenberg models. *Phys. Rev. Lett.*, 17(22):1133, 1966. 43

[97] J. M. Luttinger and L. Tisza. Theory of dipole interaction in crystals. *Phys. Rev.*, 70 (11-12):954, 1946. 43

[98] L. Onsager. Electrostatic Interaction of Molecules. *Journal of Physical Chemistry*, 43 (2):189–196, 1939. 43

[99] O. Nagai, S. Miyashita, and T. Horiguchi. Ground state of the antiferromagnetic Ising model of general spin S on a triangular lattice. *Phys. Rev. B*, 47(1):202, 1993. 43

[100] Z. L. Dun, J. Trinh, K. Li, M. Lee, K. W. Chen, R. Baumbach, Y. F. Hu, Y. X. Wang, B. S. Choi, E. S.and Shastry, , A. P. Ramirez, and H. D. Zhou. Magnetic ground states of the rare-earth tripod kagome lattice $Mg_2RE_3Sb_3O_{14}$ (RE= Gd, Dy, Er). *Phys. Rev. Lett.*, 116(15):157201, 2016. 47

[101] G. Möller and R. Moessner. Magnetic multipole analysis of kagome and artificial spin-ice dipolar arrays. *Phys. Rev. B*, 80(14):140409, 2009. 47

[102] J. Snyder, B. G. Ueland, J. S. Slusky, H. Karunadasa, R. J. Cava, and P. Schiffer. Low-temperature spin freezing in the $Dy_2Ti_2O_7$ spin ice. *Phys. Rev. B*, 69(6):064414, 2004. 49

[103] J. A. Quilliam, L. R. Yaraskavitch, H. A. Dabkowska, B. D. Gaulin, and J. B. Kycia. Dynamics of the magnetic susceptibility deep in the Coulomb phase of the dipolar spin ice material $Ho_2Ti_2O_7$. *Phys. Rev. B*, 83(9):094424, 2011. 49, 56

[104] R. J. Aldus, T. Fennell, P. P. Deen, E. Ressouche, G. C. Lau, R. J. Cava, and S. T. Bramwell. Ice rule correlations in stuffed spin ice. *New Journal of Physics*, 15(1): 013022, 2013. 50

[105] J. M. Kosterlitz and D. J. Thouless. Ordering, metastability and phase transitions in two-dimensional systems. *Journal of Physics C: Solid State Physics*, 6(7):1181, 1973. 52

[106] K. Binder and A. P. Young. Spin glasses: Experimental facts, theoretical concepts, and open questions. *Rev. Mod. Phys.*, 58(4):801, 1986. 52

[107] H. Maletta and W. Felsch. Insulating spin-glass system $Eu_xSr_{1-x}S$. *Phys. Rev. B*, 20 (3):1245, 1979. 52

[108] Z. L. Dun, X. Li, R. S. Freitas, E. Arrighi, C. R. Dela Cruz, M. Lee, E. S. Choi, H. B. Cao, H. J. Silverstein, C. R. Wiebe, et al. Antiferromagnetic order in the pyrochlores $R_2Ge_2O_7$ (R= Er, Yb). *Phys. Rev. B*, 92(14):140407, 2015. 54, 59

[109] A. M. Hallas, J. A. M. Paddison, H. J. Silverstein, A. L. Goodwin, J. R. Stewart, A. R. Wildes, J. G. Cheng, J. S. Zhou, J. B. Goodenough, E. S. Choi, et al. Statics and dynamics of the highly correlated spin ice $Ho_2Ge_2O_7$. *Phys. Rev. B*, 86(13):134431, 2012. 56, 66

[110] K. Matsuhira, Y. Hinatsu, K. Tenya, H. Amitsuka, and T. Sakakibara. Low-temperature magnetic properties of pyrochlore stannates. *Journal of the Physical Society of Japan*, 71(6):1576–1582, 2002. 56

[111] X. Ke, M. L. Dahlberg, E. Morosan, J. A. Fleitman, R. J. Cava, and P. Schiffer. Magnetothermodynamics of the ising antiferromagnet $Dy_2Ge_2O_7$. *Phys. Rev. B*, 78 (10):104411, 2008. 56

[112] J. D. M. Champion, M. J. Harris, P. C. W. Holdsworth, A. S. Wills, G. Balakrishnan, S. T. Bramwell, E. Čižmár, T. Fennell, J. S. Gardner, J. Lago, et al. $Er_2Ti_2O_7$: Evidence of quantum order by disorder in a frustrated antiferromagnet. *Phys. Rev. B*, 68(2):020401, 2003. 56

[113] Y.-L. Wang and B. R. Cooper. Collective excitations and magnetic ordering in materials with singlet crystal-field ground state. *Phys. Rev.*, 172(2):539, 1968. 58, 61

[114] G.-W. Chern, P. Mellado, and O. Tchernyshyov. Two-stage ordering of spins in dipolar spin ice on the kagome lattice. *Phys. Rev. Lett.*, 106(20):207202, 2011. 60, 77, 78

[115] M. J. P. Gingras and P. A McClarty. Quantum spin ice: a search for gapless quantum spin liquids in pyrochlore magnets. *Reports on Progress in Physics*, 77(5):056501, 2014. 61

[116] S. Sachdev. *Quantum phase transitions*. Wiley Online Library, 2007. 61

[117] S. Suzuki, J.-I. Inoue, and B. K. Chakrabarti. *Quantum Ising phases and transitions in transverse Ising models*, volume 862. Springer, 2012. 61

[118] R. Coldea, D. A. Tennant, E. M. Wheeler, E. Wawrzynska, D. Prabhakaran, M. Telling, K. Habicht, P. Smeibidl, and K. Kiefer. Quantum criticality in an Ising chain: experimental evidence for emergent E8 symmetry. *Science*, 327(5962):177–180, 2010. 61

[119] R. W. Youngblood, G. Aeppli, J. D. Axe, and J. A. Griffin. Spin dynamics of a model singlet ground-state system. *Phys. Rev. Lett.*, 49(23):1724, 1982. 61, 67

[120] R. B. Stinchcombe. Ising model in a transverse field. I. Basic theory. *Journal of Physics C: Solid State Physics*, 6(15):2459, 1973. 65, 66

[121] R. J. Elliott, P. Pfeuty, and C. Wood. Ising model with a transverse field. *Phys. Rev. Lett.*, 25(7):443, 1970. 66

[122] G. Ehlers, A. L. Cornelius, M. Orendac, M. Kajnakova, T. Fennell, S. T. Bramwell, and J. S. Gardner. Dynamical crossover in hotspin ice. *Journal of Physics: Condensed Matter*, 15(2):L9, 2002. 66

[123] P. Fulde and M. Loewenhaupt. Magnetic excitations in crystal-field split 4f systems. *Advances in Physics*, 34(5):589–661, 1985. 66, 67

[124] J. Kotzler, H. Neuhaus-Steinmetz, A. Froese, and D. Gorlitz. Relaxation-coupled order-parameter oscillation in a transverse Ising system. *Phys. Rev. Lett.*, 60(7):647, 1988. 67

[125] R. G. Lloyd and P. W. Mitchell. Spin dynamics in the singlet-singlet ground state magnet $LiTb_xY_{1-x}F_4$; a neutron scattering study. *Journal of Physics: Condensed Matter*, 2(10):2383, 1990. 67

[126] V. H. Santos and C. Scherer. A new approximation for the dynamics of the transverse Ising model. *Zeitschrift für Physik B Condensed Matter*, 40(1):95–97, 1980. 67

[127] M. E. Brooks-Bartlett, S. T. Banks, L. D. C. Jaubert, A. Harman-Clarke, and P. C. W. Holdsworth. Magnetic-moment fragmentation and monopole crystallization. *Phys. Rev. X*, 4(1):011007, 2014. 73

[128] R. Moessner, S. L. Sondhi, and P. Chandra. Two-dimensional periodic frustrated Ising models in a transverse field. *Phys. Rev. Lett.*, 84(19):4457, 2000. 75

[129] R. Moessner and S. L. Sondhi. Ising models of quantum frustration. *Phys. Rev. B*, 63 (22):224401, 2001. 75, 78

[130] P. Nikolić and T. Senthil. Theory of the kagome lattice Ising antiferromagnet in weak transverse fields. *Phys. Rev. B*, 71(2):024401, 2005. 75, 78

[131] S. V. Isakov, S. Wessel, R. G. Melko, K. Sengupta, and Y. B. Kim. Hard-core bosons on the kagome lattice: Valence-bond solids and their quantum melting. *Phys. Rev. Lett.*, 97(14):147202, 2006. 78

[132] G. Vidal. Class of quantum many-body states that can be efficiently simulated. *Phys. Rev. Lett.*, 101(11):110501, 2008. 78

[133] R. Moessner, S. L. Sondhi, and P. Chandra. Two-dimensional periodic frustrated Ising models in a transverse field. *Phys. Rev. Lett.*, 84(19):4457, 2000. 78

Appendices

List of Publications

First-Author Publications

[1] **Z. L. Dun**., J. Trinh, M. Lee, E. S. Choi, K. Li, Y. F. Hu, Y. X. Wang, N. Blanc, A. P. Ramirez, and H. D. Zhou. Structural and magnetic properties of two branches of the tripod-kagome-lattice family $A_2R_3Sb_3O_{14}$ (A= Mg, Zn; R= Pr, Nd, Gd, Tb, Dy, Ho, Er, Yb). *Phys. Rev.B*, 95(10):104439, 2017.

[2] **Z. L. Dun**, J. Trinh, K. Li, M. Lee, K. W. Chen, R. Baumbach, Y. F. Hu, Y. X. Wang, B. S. Choi, E. S.and Shastry, , A. P. Ramirez, and H. D. Zhou. Magnetic ground states of the rare-earth tripod kagome lattice $Mg_2RE_3Sb_3O_{14}$ (RE= Gd, Dy, Er). *Phys. Rev. Lett.*, 116(15):157201, 2016.

[3] **Z. L. Dun**, X. Li, R. S. Freitas, E. Arrighi, C. R. Dela Cruz, M. Lee, E. S. Choi, H. B. Cao, H. J. Silverstein, C. R. Wiebe, et al. Antiferromagnetic order in the pyrochlores $R_2Ge_2O_7$ (R= Er, Yb). *Phys. Rev.B*, 92(14):140407, 2015.

[4] **Z. L. Dun**, J. Ma, H. B. Cao, Y. Qiu, J. R. D. Copley, T. Hong, M. Matsuda, J. G. Cheng, M. Lee, E. S. Choi, S. Johnston, and H. D. Zhou. Competition between the inter- and intra-sublattice interactions in $Yb_2V_2O_7$. *Phys. Rev.B*, 91:064425, 2015.

[5] **Z. L. Dun**, V. O. Garlea, C. Yu, Y. Ren, E. S. Choi, H. M. Zhang, S. Dong, and H. D. Zhou. $LaSrVO_4$: A candidate for the spin-orbital liquid state. *Phys. Rev.B*, 89(23):235131, 2014.

[6] **Z. L. Dun**, M. Lee, E. S. Choi, A. M. Hallas, C. R. Wiebe, J. S. Gardner, E. Arrighi, R. S. Freitas, A. M. Arevalo-Lopez, J. P. Attfield, et al. Chemical pressure effects on magnetism in the quantum spin liquid candidates $Yb_2X_2O_7$ (X= Sn, Ti, Ge). *Phys. Rev.B*, 89(6):064401, 2014.

[7] **Z. L. Dun**, E. S. Choi, H. D. Zhou, A. M. Hallas, H. J. Silverstein, Y. Qiu, J. R. D. Copley, J. S. Gardner, and C. R. Wiebe. $Yb_2Sn_2O_7$: A magnetic coulomb liquid at a quantum critical point. *Phys. Rev.B*, 87(13):134408, 2013.

Collaborative Publications

[1] Y. Jiang, **Z. L. Dun**, H. D. Zhou, Z. Lu, K.-W. Chen, S. Moon, T. Besara, T. M. Siegrist, R. E. Baumbach, D. Smirnov, and Z. Jiang. Landau-level spectroscopy of massive dirac fermions in single-crystalline $ZrTe_5$ thin flakes. *Phys. Rev. B*, 96:041101, Jul 2017.

[2] X. Li, Y. Q. Cai, Q. Cui, C. J. Lin, **Z. L. Dun**, K. Matsubayashi, Y. Uwatoko, Y. Sato, T. Kawae, S. J. Lv, C. Q. Jin, J.-S. Zhou, J. B. Goodenough, H. D. Zhou, and J.-G. Cheng. Long-range magnetic order in the heisenberg pyrochlore antiferromagnets $Gd_2Ge_2O_7$ and $Gd_2Pt_2O_7$ synthesized under high pressure. *Phys. Rev. B*, 94:214429, Dec 2016.

[3] R. Sinclair, H. B. Cao, V. O. Garlea, M. Lee, E. S. Choi, **Z. L. Dun**, S. Dong, E. Dagotto, and H. D. Zhou. Canted magnetic ground state of quarter-doped manganites $R_{0.75}Ca_{0.25}MnO_3$ (R= Y, Tb, Dy, Ho, and Er). *Journal of Physics: Condensed Matter*, 29(6):065802, 2016.

[4] J. A. M. Paddison, M. Daum, **Z. L. Dun**, G. Ehlers, Y. Liu, M. B. Stone, H. D. Zhou, and M. Mourigal. Continuous excitations of the triangular-lattice quantum spin liquid $YbMgGaO_4$. *Nature Physics*, 2016.

[5] J. Ma, Y. Kamiya, T. Hong, H. B. Cao, G. Ehlers, W. Tian, C. D. Batista, **Z. L. Dun**, H. D. Zhou, and M. Matsuda. Static and dynamical properties of the spin-1/2 equilateral triangular-lattice antiferromagnet $Ba_3CoSb_2O_9$. *Phys. Rev.Lett.*, 116(8):087201, 2016.

[6] X. Li, Y. Q. Cai, Q. Cui, C. J. Lin, **Z. L. Dun**, K. Matsubayashi, Y. Uwatoko, Y. Sato, T. Kawae, S. J. Lv, et al. Long-range magnetic order in the heisenberg pyrochlore

antiferromagnets $Gd_2Ge_2O_7$ and $Gd_2Pt_2O_7$ synthesized under high pressure. *Phys. Rev.B*, 94(21):214429, 2016.

[7] W. Yu, Y. Jiang, J. Yang, **Z. L. Dun**, H. D. Zhou, Z. Jiang, P. Lu, and W. Pan. Quantum oscillations at integer and fractional landau level indices in single-crystalline $ZrTe_5$. *Scientific reports*, 6, 2016.

[8] Y. Q. Cai, Q. Cui, X Li, **Z. L. Dun**, J. Ma, C. dela Cruz, Y. Y. Jiao, J. Liao, P. J. Sun, Y. Q. Li, et al. High-pressure synthesis and characterization of the effective pseudospin S = 1/2 xy pyrochlores $R_2Pt_2O_7$ (R= Er, Yb). *Phys. Rev.B*, 93(1):014443, 2016.

[9] M Zhu, D Do, C. R. Dela Cruz, **Z. L. Dun**, J-G Cheng, H. Goto, T. Uwatoko, Y.and Zou, H. D. Zhou, S. D. Mahanti, et al. Ferromagnetic superexchange in insulating Cr_2MoO_6 by controlling orbital hybridization. *Phys. Rev.B*, 92(9):094419, 2015.

[10] L. Li, J. R. Morris, M. R. Koehler, **Z. L. Dun**, H. D. Zhou, J. Q. Yan, D. Mandrus, and V. Keppens. Structural and magnetic phase transitions in $EuTi_{1-x}Nb_xO_3$. *Phys. Rev.B*, 92(2):024109, 2015.

[11] G. Quirion, M. Lapointe-Major, M. Poirier, J. A. Quilliam, **Z. L. Dun**, and H. D. Zhou. Magnetic phase diagram of $Ba_3CoSb_2O_9$ as determined by ultrasound velocity measurements. *Phys. Rev.B*, 92(1):014414, 2015.

[12] J. Ma, J. H. Lee, S. E. Hahn, T. Hong, H. B. Cao, A. A. Aczel, **Z. L. Dun**, M. B. Stone, W. Tian, Y. Qiu, et al. Strong competition between orbital ordering and itinerancy in a frustrated spinel vanadate. *Phys. Rev.B*, 91(2):020407, 2015.

[13] R. Sinclair, J. Ma, H. B. Cao, T. Hong, M. Matsuda, **Z. L. Dun**, and H. D. Zhou. Evolution of the magnetic and structural properties of $Fe_{1-x}Co_xV_2O_4$. *Phys. Rev.B*, 92(13):134410, 2015.

[14] M. Lee, E. S. Choi, X. Huang, J. Ma, C. R. Dela Cruz, M. Matsuda, W. Tian, **Z. L. Dun**, S. Dong, and H. D. Zhou. Magnetic phase diagram and multiferroicity of $Ba_3MnNb_2O_9$: A spin-5/2 triangular lattice antiferromagnet with weak easy-axis anisotropy. *Phys. Rev.B*, 90(22):224402, 2014.

[15] T. Zou, **Z. L. Dun**, H. B. Cao, M. Zhu, H.D. Zhou, and X. Ke. Tuning the ferroelectric state in multiferroic $TbMnO_3$ single crystal by a trapped-charge-induced internal electric field. *Journal of Applied Physics*, 116(10):104101, 2014.

[16] H. J. Silverstein, A. E. Smith, C. Mauws, D. L. Abernathy, H. D. Zhou, **Z. L. Dun**, . van Lierop, and C. R. Wiebe. Direct measurement of the spin gap in a quasi-one-dimensional clinopyroxene: $NaTiSi_2O_6$. *Phys. Rev.B*, 90(14):140402, 2014.

[17] Y. Kohama, K. Mochidzuki, T. Terashima, A. Miyata, A. DeMuer, T. Klein, C. Marcenat, **Z. L. Dun**, H. D. Zhou, G. Li, et al. Entropy of the quantum soliton lattice and multiple magnetization steps in $BiCu_2PO_6$. *Phys. Rev.B*, 90(6):060408, 2014.

[18] M. Zhu, D. Do, C. R. Dela Cruz, **Z. L. Dun**, H. D. Zhou, S. D. Mahanti, and X. Ke. Tuning the magnetic exchange via a control of orbital hybridization in $Cr_2(Te_{1-x}W_x)O_6$. *Phys. Rev.Lett.*, 113(7):076406, 2014.

[19] T. Zou, **Z. L. Dun**, H. B. Cao, M. Zhu, D. L. Coulter, H. D. Zhou, and X. Ke. Excess-hole induced high temperature polarized state and its correlation with the multiferroicity in single crystalline $DyMnO_3$. *Appl. Phys. Lett.*, 105(5):052906, 2014.

[20] M. Lee, J. Hwang, E. S. Choi, J. Ma, C. R. Dela Cruz, M. Zhu, X. Ke, **Z. L. Dun**, and H. D. Zhou. Series of phase transitions and multiferroicity in the quasi-two-dimensional spin-1/2 triangular-lattice antiferromagnet $Ba_3CoNb_2O_9$. *Phys. Rev.B*, 89(10):104420, 2014.

[21] J. Ma, C. D. Dela Cruz, T. Hong, W. Tian, A. A. Aczel, S. X. Chi, J-Q Yan, **Z. L. Dun**, H. D. Zhou, and M. Matsuda. Magnetic phase transition in the low-dimensional compound $BaMn_2Si_2O_7$. *Phys. Rev.B*, 88(14):144405, 2013.

Vita

Zhiling Dun was born on March 1st, 1989, in Wuhan, China. After high-school, he joined the physics department at the University of Science and Technology of China in 2007 and received a B.S. in physics in 2011. At the same year, he came to U.S. to pursue a Ph.D in condensed matter physics at the University of Tennessee. He joined the group of Dr. Haidong Zhou and worked five years as a research assistant before receiving his Ph.D in 2017.